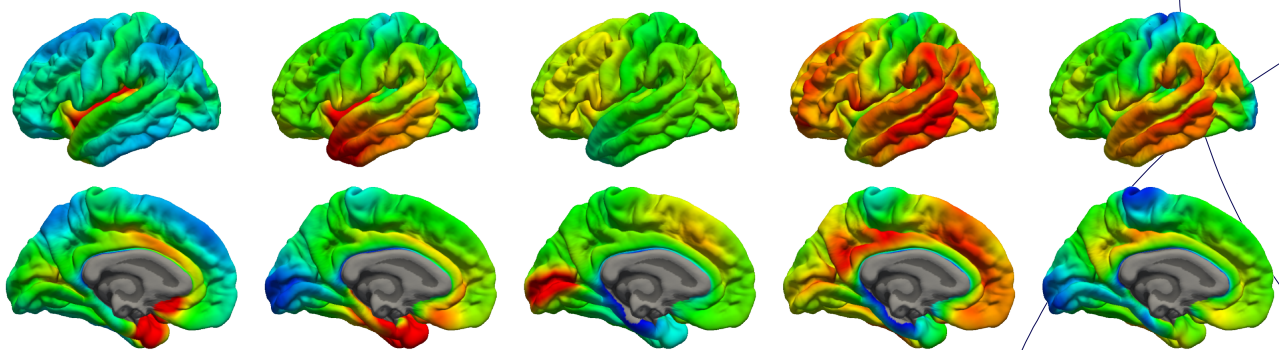**PhD thesis**

Vincent Beliveau

Functional and Molecular Imaging of the Serotonin System in the Human Brain

Main Supervisor: Gitte Moos Knudsen

Co-Supervisors: Claus Svarer, Melanie Ganz and Patrick M. Fisher

This thesis has been submitted to the Graduate School of Health and Medical Sciences, University of Copenhagen on November 30th, 2017

Ph.D. thesis by Vincent Beliveau, M.Sc.

Neurobiology Research Unit, Rigshospitalet, Copenhagen, Denmark

Academic Advisors

Professor Gitte Moos Knudsen, MD, DMSc

Neurobiology Research Unit, Rigshospitalet, Copenhagen, Denmark

Senior Researcher Claus Svarer, Ph.D.

Neurobiology Research Unit, Rigshospitalet, Copenhagen, Denmark

Assistant Professor Melanie Ganz, Ph.D.

Neurobiology Research Unit, Rigshospitalet, Copenhagen, Denmark

Senior Researcher Patrick M. Fisher, Ph.D.

Neurobiology Research Unit, Rigshospitalet, Copenhagen, Denmark

Evaluation committee

Chair: Professor Albert Gjedde

Department of Neuroscience, University of Copenhagen, Denmark

Associate Professor Koen Van Leemput

DTU Compute, Technical University of Denmark, Denmark

Associate Professor Rupert Lanzenberger

Department of Psychiatry and Psychotherapy, Medical University of Vienna, Austria

Submitted: November 30th, 2017

Front: Cortical density maps for 5-HTT, $5\text{-HT}_{1A}R$, $5\text{-HT}_{1B}R$, $5\text{-HT}_{2A}R$ and 5-HT_4R (study II)

Contents

Concluding remarks and future perspectives   **43**

References   **45**

Appendix   **55**

Preface

The work presented in this thesis was accomplished during my appointment as a Ph.D. student at the Neurobiology Research Unit of Righospitalet, Copenhagen, Denmark, from December 2014 to November 2017. My academic advisors were Gitte Moos Knudsen, Claus Svarer, Melanie Ganz and Patrick M. Fisher.

Peer-Reviewed Publications

Study I

V. Beliveau, C. Svarer, V. G. Frokjaer, G. M. Knudsen, D. N. Greve, P. M. Fisher, Functional connectivity of the dorsal and median raphe nuclei at rest, Neuroimage 116 (2015) 187–195.

Study II

V. Beliveau, M. Ganz, L. Feng, B. Ozenne, L. Højgaard, P. M. Fisher, C. Svarer, D. N. Greve, G. M. Knudsen, A high-resolution in vivo atlas of the human brain's serotonin system, Journal of Neuroscience 37 (1) (2017) 120–128.

Study III

V. Beliveau, G. Papoutsakis, J. L. Hinrich, M. Mørup, Sparse probabilistic parallel factor analysis for the modeling of pet and task-fmri data, in: Medical Computer Vision and Bayesian and Graphical Models for Biomedical Imaging, Springer, Cham, 2016, pp. 186–198.

Other Relevant Publications

[1] M. Ganz, L. Feng, H. D. Hansen, V. Beliveau, C. Svarer, G. M. Knudsen, D. N. Greve, Cerebellar heterogeneity and its impact on pet data quantification of 5-ht receptor radioligands, Journal of Cerebral Blood Flow & Metabolism 37 (9) (2017) 3243–3252.

[2] M. Nørgaard, M. Ganz, C. Svarer, B. Mc Mahon, P. M. Fisher, N. Churchill, V. Beliveau, C. Grady, S. C. Strother, G. M. Knudsen, Brain networks implicated in seasonal affective disorder: A neuroimaging pet study of the serotonin transporter, Frontiers in Neuroscience 11 (2017) 614.

[3] S. da Cunha-Bang, L. V. Hjordt, E. Perfalk, V. Beliveau, C. Bock, S. Lehel, C. Thomsen, D. Sestoft, C. Svarer, G. M. Knudsen, Serotonin 1b receptor binding is associated with trait anger and level of psychopathy in violent offenders, Biological psychiatry 82 (4) (2017) 267–274.

[4] S. da Cunha-Bang, P. M. Fisher, L. V. Hjordt, E. Perfalk, V. Beliveau, K. Holst, G. M. Knudsen, Men with high serotonin 1b receptor binding respond to provocations with heightened amygdala reactivity, NeuroImage 166 (2017) 79–85.

[5] A. P. Skibsted, S. d. Cunha-Bang, J. M. Carré, A. E. Hansen, V. Beliveau, G. M. Knudsen, P. M. Fisher, Aggression-related brain function assessed with the point subtraction aggression paradigm in fmri, Aggressive Behavior 43 (6) (2017) 601–610.

[6] A. Ettrup, C. Svarer, B. McMahon, S. da Cunha-Bang, S. Lehel, K. Møller, A. Dyssegaard, M. Ganz, V. Beliveau, L. M. Jørgensen, et al., Serotonin 2a receptor agonist binding in the human brain with [11 c] cimbi-36: Test–retest reproducibility and head-to-head comparison with the antagonist [18 f] altanserin, Neuroimage 130 (2016) 167–174.

[7] P. M. Fisher, C. B. Larsen, V. Beliveau, S. Henningsson, A. Pinborg, K. K. Holst, P. S. Jensen, C. Svarer, H. R. Siebner, G. M. Knudsen, et al., Pharmacologically induced sex hormone fluctuation effects on resting-state functional connectivity in a risk model for depression: a randomized trial, Neuropsychopharmacology 44 (2) (2016) 446–453.

[8] M. Nørgaard, M. Ganz, C. Svarer, V. Beliveau, P. M. Fisher, B. Mc Mahon, D. N. Greve, S. C. Strother, G. M. Knudsen, Estimation of regional seasonal variations in sert-levels using the freesurfer pet pipeline: a reproducibility study, in: Proceedings of the MICCAI workshop on computational methods for molecular imaging, 2015.

Summary (English)

The serotonin (5-HT) system plays a central role in the regulation of brain function and its disruption and/or imbalance has been linked to many brain disorders. Although the 5-HT system has been extensively studied in animal models and post-mortem tissue, many facets of the 5-HT system in the *in vivo* human brain remain to be fully characterized. In the work presented in this thesis we sought to investigate the functional connectivity and the spatial structure of the 5-HT system by taking advantage of the unique high resolution PET, MRI and fMRI data available in the Cimbi database.

The raphe nuclei form the seat of the serotonergic projections throughout the mammalian brain. Hence, they are an ideal proxy for identifying brain function linked to the 5-HT system. We investigated the functional connectivity of the 5-HT system by finding which brain regions were synchronized with the activity of the raphe nuclei in the human brain at rest, as measured with resting-state functional MRI. In order to asses if the strength of the synchronization is related to a feature of the 5-HT system, we subsequently investigated the extent to which it was associated with corresponding serotonin transporter density.

A detailed *in vivo* mapping of the 5-HT system in the human brain offers the opportunity to investigate the spatial characterization of the 5-HT system. Taking advantage of the high resolution PET images of the Cimbi database and the availability of corresponding structural MRI, we created an *in vivo* 5-HT atlas of the human brain receptors $5\text{-HT}_{1A}R$, $5\text{-HT}_{1B}R$, $5\text{-HT}_{2A}R$ and $5\text{-HT}_{4}R$ and the transporter, 5-HTT. We validated this 5-HT atlas by comparing it to measurements from autoradiography studies, which in turn also allowed us to convert the PET measures into densities. The spatial association between density and levels of genetic information was subsequently investigated using data from the Allen Human Brain Atlas.

Brain parcellations derived from features such as cytoarchitectonic boundaries or functional activation may not represent a correct representation of the underlying distribution of the 5-HT receptors and transporter. Hence, creating a new parcellation specific to the 5-HT receptors and the transporter can provide a model more relevant to the 5-HT system than existing ones. Changes in the dynamic profile of PET data reflect changes in receptor density and may contain important characteristics to segregate brain regions based on variation of the receptor distribution profile. We derived and implemented two probabilistic parallel factor analysis models to identify, from the dynamic PET data, brain regions with distinct dynamic properties. These models take advantage of common modes in the data (e.g. space and time) to identify latent components summarizing the data across another mode (e.g. subjects).

The models were validated through simulation, applied to the dynamic PET data and additionally to an fMRI dataset to test its applicability to other modalities.

Summary (Danish)

Serotonin (5-HT) systemet spiller en central rolle i modulering af hjernens funktion, og der ses forstyrrelser i 5-HT systemet ved en række forskellige neuropsykiatriske sygdomme. 5-HT-systemet er grundigt beskrevet i dyr og også delvis i menneskehjerner udtaget efter døden, men der er stadig betydelige mangler i forståelsen af 5-HT-systemets funktion hos det levende menneske. Denne afhandling beskriver resultaterne af studier af den 5-HT drevne funktionelle forbindelse mellem hjerneregioner samt en kortlægning af nogle af 5-HT-systemets receptorer og transporter. Arbejdet bygger på unikke PET, MRI- og fMRI-data, der er tilgængelige i Cimbi-databasen.

I pattedyrshjernen er det raphe-kernerne, hvor 5-HT dannes og dermed danner sæde for de serotonerge projektioner og dermed udgør de et udgangspunkt for undersøgelserne af hjerneprojektioner af relevans for 5-HT systemet. Ved at undersøge den funktionelle aktivitet fra raphe-kernerne kunne identificere, hvilke hjerneområder der er synkroniseret med kernerne, målt ved funktionel MR i vågentilstand mens hjernen ikke foretager sig noget bestemt. For at vurdere, om styrken af synkroniseringen er relateret til et træk af 5-HT-systemet, undersøgte vi senere, i hvilket omfang det var forbundet med tilsvarende tæthed af 5-HT transporteren.

En detaljeret in vivo kortlægning af 5-HT-systemet i den menneskelige hjerne giver mulighed for at undersøge den strukturelle karakterisering af 5-HT-systemet. Ved at udnytte PET-billederne med høj opløsning fra Cimbi-databasen og de tilhørende strukturelle MRI skanninger har vi genereret en 5-HT-atlas af de humane hjerne-receptorer 5-HT$_{1A}$R, 5-HT$_{1B}$R, 5-HT$_{2A}$R og 5-HT$_4$R og 5-HT transporteren. Vi validerede denne 5-HT-atlas ved at sammenligne den med målinger fra autoradiografi studier, som tillod en kalibrering af PET-målene til koncentrationer. Den strukturelle tilknytning mellem tæthed og niveauer af genetisk information blev efterfølgende undersøgt ved anvendelse af data fra Allen Human Brain Atlas. Opdeling af hjernen i funktionelle enheder (parcellering) foretages som regel vhja. f.eks. cytoarkitektoniske grænser eller funktionel aktivering. Men her anvendte vi det ovenfor beskrevne 5-HT atlas til at at skabe en ny parcellation, specifik for 5-HT-systemet. Ændringer i den dynamiske profil af PET-data afspejler ændringer i receptortætheden og kan indeholde vigtige egenskaber til at adskille hjerneområder baseret på variation af receptorfordelingsprofilen. På baggrund af de dynamiske PET-data afledte og implementerede vi to probabilistiske parallel faktoranalysemodeller til at identificere, hjerneområder med distinkt dynamiske egenskaber. Disse modeller udnytter komponenter i data (fx struktur og tid) for at identificere latente komponenter, der opsummerer data i en anden tilstand (fx individer). Modellerne blev valideret gennem simulering og blev efterfølgende anvendt på dynamiske

PET data og fMRI datasæt for at teste dets anvendelighed til andre modaliteter.

Acknowledgements

Abbreviations

5-HT 5-hydroxytryptamine, serotonin

AHBA Allen Human Brain Atlas

ARD Automatic relevance determination

BBR Boundary-based registration

BOLD Blood-oxygen-level-dependent signal

BP   Binding potential

BP$_{ND}$ Non-displaceable binding potential

cAMP Cyclic adenosine monophosphate

CVS Combined volume and surface

DAG Diacylglycerol

FC   Functional connectivity

fMRI Functional magnetic resonance imaging

FS   FreeSurfer

FWHM Full width at half maximum

GLM General Linear Model

IP$_3$ Inositol triphosphate

MRI Magnetic resonance imaging

mRNA Messenger ribonucleic acid

PARAFAC Parallel factor analysis

PCA Principal component analysis

PET Positron emission tomography

PICA Probabilistic independent component analysis

RF   Radio frequency

RSN Resting-state network

SP-PARAFAC Sparse parallel factor analysis

SP-PCA Sparse principal component analysis

SSRI Selective serotonin reuptake inhibitor

VB   Variational Bayes

VB-PARAFAC Variational Bayes parallel factor analysis

VB-PCA Variational Bayes principal component analysis

WM White matter

Introduction

The serotonin (5-hydroxytryptamine, 5-HT) system is one of the most complex neurotransmitter systems in the mammalian brain. It is involved in a wide range of brain functions and is a key component to the understanding of brain regulation and associated disorders. To date, molecular imaging techniques (e.g. positron emission tomography (PET)) are the only available tool for the study of neuroreceptors in the living human brain. To understand the 5-HT system it is essential to obtain a precise description of its functions and structure, however the 5-HT system is yet to be fully characterized. The work presented here sought to highlight the functional and structural properties of the 5-HT system.

Although 5-HT is widely involved in brain function, only the raphe nuclei can be characterized as having a primary serotonergic role. The raphe nuclei are the seat of serotonergic innervation throughout the cortex and are the source of synthesis for cerebral 5-HT. As such, they form an unique proxy for the study of brain activation related to the 5-HT system. The innervation of the raphe nuclei has been thoroughly studied in rodents [1, 2]. However, it was previously unclear how neuronal modulation of these nuclei are related to the function of afferent and efferent brain regions. Hence, understanding the functional connectivity (FC) of the raphe nuclei is a first step in mapping serotonergic brain function. Unfortunately, the raphe nuclei are a relatively small structure, made of an heterogeneous amalgam of cells, including white matter cells, and is impossible to delineate precisely and difficult to study using standard techniques such as magnetic resonance imaging (MRI). For this reason, all previous attempts to quantify the functional properties of the raphe nuclei with functional MRI (fMRI) have been using manually drawn regions of interest (ROI) [3, 4, 5] which may have been inaccurate.

The structure of the 5-HT system is characterized by the distribution of its receptors and transporter. Previously, the distribution of the 5-HT receptors had been quantified through autoradiography [6, 7] or with PET images of relatively low resolution [8]. These studies formed the foundation of our knowledge about the distribution of 5-HT receptors throughout the human brain. However, their applicability to further comparative studies in neuroimaging is limited and difficult. Autoradiography is usually reported as a table without precise spatial correspondence other than region names and the previous 5-HT atlas was of relatively low resolution and lacked corresponding MRI, hence limiting its spatial precision [8]. The Cimbi database [9] contains high resolution PET targeting the $5\text{-HT}_{1A}\text{R}$, $5\text{HT}_{1B}\text{R}$, $5\text{-HT}_{2A}\text{R}$ and $5\text{-HT}_{4}\text{R}$ receptors and the transporter, 5-HTT, together with corresponding structural MRI images. Hence, this data offered a unique opportunity to created a high resolution *in*

vivo atlas for some of the 5-HT receptors and the transporter in the human brain.

Neuroscientists have repeatedly tried to divide the human brain into regions of homogeneous properties in an effort to establish a simpler, discrete description of the brain's function and structure. An early parcellation, the well-know Broadmann areas, divided the brain according to its cytoarchitectonic features [10]. In more recent work, based on neuroimaging studies, the human brain has been parcellated using features such as gyrification [11], intrinsic brain activation [12] and even multi modal approaches [13]. However, these parcellations of the brain may not reflect the specific organization (i.e. receptor distribution) of the 5-HT system. Summary measures proportional to receptor density (e.g. binding potential) can potentially be used to identify distinct brains regions. Summarizing the dynamic PET data may however mask pertinent information that would allow to segregate regions of the brain which would otherwise be considered together as a uniform region. For example, regions with the same binding potential may in truth have different dynamics and should be considered as distinct. Unfortunately, there is considerable noise in dynamic PET data and models accounting for the noise while keeping optimal spatial resolution are necessary to obtain detailed parcellation of the brain. The Parallel Factor Analysis (PARAFAC) is a model similar to principal component analysis (PCA), but which leverages common modes (e.g. time and space) across multiple datasets (e.g. subjects) to identify vectors maximally explaining variance in the data. In a probabilistic framework, priors can be used in these model to impose sparsity in their solution and potentially identify solution which may be more biologically relevant.

Thus, in the context of the issues exposed here, the primary aims of this thesis were to:

1. Investigate the functional connectivity of the dorsal and median raphe nuclei (**Study I**).

2. Create a high resolution atlas of the 5-HT system using PET and MRI data from the Cimbi database (**Study II**)

3. Derive, implement and validate probabilistic PARAFAC algorithms and investigate their applicability to extract features from dynamic PET of 5-HT targets and model fMRI data. (**Study III**)

Background

Serotonin System

The 5-HT molecule (Figure 1) is a monoamine neurotransmitter derived from tryptophan. Synthesis of cerebral 5-HT occurs within a group of nuclei located on the midline of the brainstem, the raphe nuclei. Of those, the dorsal (DR) and median (MR) raphe nuclei are the source of the serotonergic innervation of the mammalian cortex [14]. The structure and physiological properties of the raphe nuclei have been extensively described in rodents [15, 16, 2]. In humans, about 70% and 43% of the neurons in the DR [17] and MR [18] are serotonergic, respectively. Indeed, a number of other neurotransmitters, such as dopamine and glutamate, have been identified in these nuclei [19].

The afferent and efferent projections of the DR and MR have been thoroughly studied in the rat and macaque monkeys. It has been shown that efferent projections of both the DR and MR are widely distributed throughout the forebrain to distinct, non-overlapping brain areas [20, 21]; these projections are exemplified in Figure 2. Conversely, the afferent inputs to the DR and MR have been shown to originate largely from the same source regions, such as medial prefrontal cortex and limbic areas [2]. However, denser inputs from hypothalamic structures to DR compared to MR have been observed. Dense monosynaptic bidirectional projections between DR and MR also exist [1]. The extent to which these observations in rodents translate into humans remains to be fully determined.
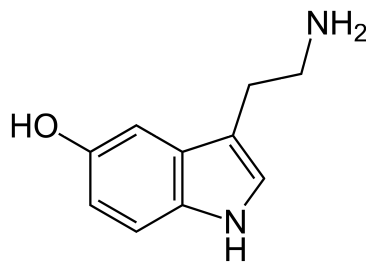

Figure 1: The serotonin molecule
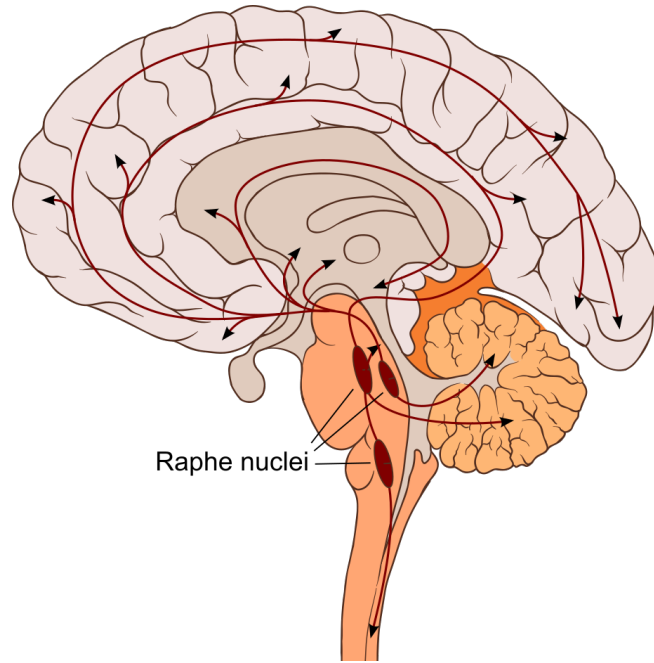
Figure 2: Projections of the raphe nuclei
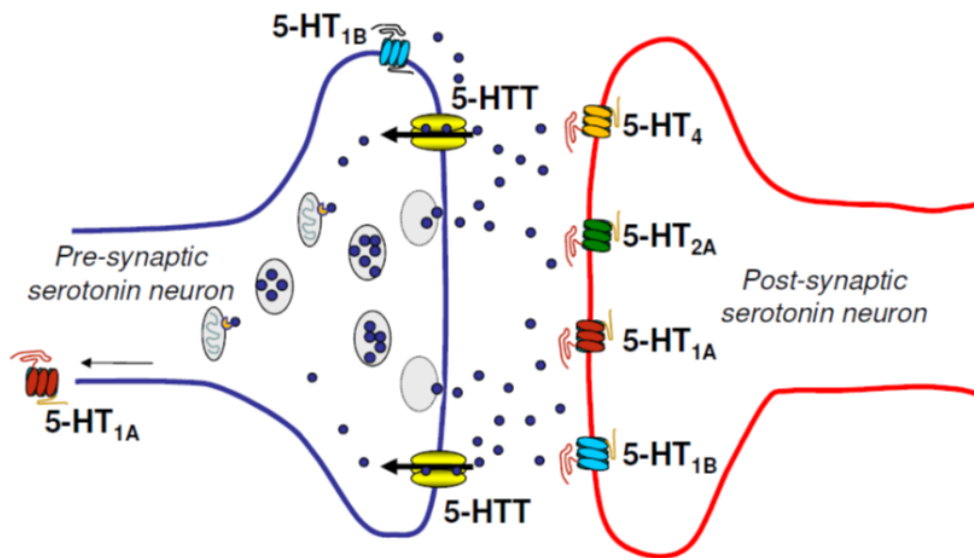
Figure 3. Synaptic localization of the 5-HT targets studied in this thesis. This figure was kindly provided by Patrick M. Fisher and was originally adapted from [22].

Characteristics of the 5-HT system which contribute to its versatility and complexity are the large range of associated receptors, the extent of serotonergic projections and the diversity of other neurotransmitters involved in this system. 5-HT receptors are G protein-coupled receptors influencing cell firing (both increase and decrease) by modulating the levels of the second messengers cyclic adenosine

monophosphate (cAMP), inositol triphosphate (IP_3) and diacylglycerol (DAG), with the exception of $5HT_3$ which is a ligand-gated ion channel. Based on their neurochemical properties, the 5-HT receptors have been classified into 7 families ($5\text{-}HT_1$ to $5\text{-}HT_7$) and 14 receptor subtypes. This thesis focuses on the four receptor subtypes $5\text{-}HT_{1A}R$, $5\text{-}HT_{1B}R$, $5\text{-}HT_{2A}R$ and $5\text{-}HT_4R$ and the transporter 5-HTT. These receptors and transporter are currently the only 5-HT targets that can be imaged *in vivo* and for which there exist corresponding radioligands with a high affinity exclusive to the subtype of interest [23]. The synaptic localization of these receptors and the transporter are illustrated in Figure 3. In terms of basic physiological mechanisms, the $5\text{-}HT_{1A}R$ and $5\text{-}HT_{1B}R$ both decrease cAMP levels of neurons (inhibition) where as the $5\text{-}HT_{2A}R$ increases levels of IP_3 and DAG (excitation) and $5\text{-}HT_4R$ increases cAMP levels (excitation). The 5-HTT recycles serotonin from the synaptic cleft back into the neuron.

All 5-HT receptors have unique spatial distributions throughout the brain and each is related to a large number of brain functions and disorders. Here a few key aspects are presented.

5-HT$_{1A}$R

The $5\text{-}HT_{1A}R$ has a high density in the raphe nuclei where it acts largely as an autoreceptor inhibiting the release of 5-HT. High densities of postsynaptic $5\text{-}HT_{1A}R$ can also be found in the hippocampus and amygdala. This receptor is involved in a large range of functions and diseases, from complex disorders such as anxiety [24] and addiction [25] to basic physiological functions such as thermoregulation [26] and vasoconstriction [27].

5-HT$_{1B}$R

The $5\text{-}HT_{1B}R$ can also be found as an autoreceptor in the raphe nuclei, although in relatively lower levels than the $5\text{-}HT_{1A}R$ and 5-HTT. More generally, the $5\text{-}HT_{1B}R$ is both an autoreceptor and heteroreceptor with high densities in occipital and frontal cortex and striatum. The $5\text{-}HT_{1B}R$ has been implicated in a range of functions and disorders, such as aggression [28], anxiety and depression [29].

5-HT$_{2A}$R

The $5\text{-}HT_{2A}R$ is an heteroreceptor which is widely expressed throughout neocortex, with higher densities in the prefrontal and temporal cortex. It is the primary target for hallucinogenic drugs such as psilocybin or LSD and a recent study suggests that these drugs could potentially be used for resolving

treatment-resistant depression [30]. 5HT$_{2A}$R has also been shown to influence brain functions such as sleep [31], sexual behavior [32] and threat processing [33, 34].

5-HT$_4$R

Contrary to the receptors described above, the 5-HT$_4$R has a low density in neocortex, but a high density in the caudate and putamen. A study suggests that the level of 5-HT$_4$R forms a good proxy for the serotonin levels in the brain [35]. This receptor has also been implicated in functions such as appetite [36] and treatment of psychiatric disorders such as depression [37].

5-HTT

Similarly to the 5-HT$_4$R, the 5-HTT has a low density in neocortex and a high density in the caudate and putamen and additionally in the raphe nuclei, midbrain and thalamus. The 5-HTT is the principal target for selective serotonin reuptake inhibitors (SSRIs) used in the treatment of depression. Interestingly, the 5-HT$_{1B}$R has been shown to be involved in the regulation of the the activity of 5-HTT [38]. The 5-HTTLPR, a polymorphism in the promoter region of the 5-HTT gene (*SLC6A4*), has been shown to influence aspects of brain function [39, 40].

Positron Emission Tomography

Positron emission tomography (PET) is an imaging technique which relies on the localization of radioactive decay of an administered radiolabeled compound. As such, PET and the related technique Single Photon Emission Computed Tomography (SPECT) are currently the only imaging techniques allowing the study of neurotransmitter systems *in vivo* in the human brain. A number of radioligands have been developed to image 5-HT receptors with PET [23].

When performing a PET experiment, a molecule with high specificity for a given target (e.g. a specific receptor subtype) is labeled with a radioactive isotope (e.g. ^{11}C or ^{18}F); this molecule is then called a radioligand. This radioligand is injected into the subject, where it distributes throughout the body, while the unstable isotope decays at a fixed rate (e.g., ^{11}C and ^{18}F have half-lives of approximately 20 and 110 min, respectively) and releases a positron. When this positron gets in contact with an electron (a process which occurs typically within 1mm of the site of decay), the positron and electron are both annihilated and two photons are emitted at 180° from one another at a specific energy level (511 keV). A PET scanner is formed by a ring of detectors around the subject which can detect

photons at that energy level. By detecting the coincidence of two photons and using their position on the detection ring and the relative delay between their detection it is then possible to determine the origin of the annihilation site. When this process is performed over a period of time, the decaying positions can be located, counted and stored within a structure called a sinogram. The sinogram data can be modeled to form quantitative spatial approximation of the origin of the decay in space and create the 3D PET images, a complex process termed reconstruction. As the labeled molecule will distribute spatially according to its interaction in tissue (e.g. binding to a receptor, usage by a cell), the PET image will be representative of the underlying process affecting the molecule. In the case of 5-HT PET imaging we are interested in the binding of the radioligand with the target receptor subtype.

The quantitative measurement of radioligand binding is expressed as binding potential (BP), a measure of the PET signal of interest relative to the non specific, or non displaceable signal. When the distribution of the radioligand can be assumed to be in stable, steady-state, a simple ratio of the signal within a target region and a reference region (e.g. blood or reference region devoid of receptor) can be used to quantify the PET images. However, in practice steady-state is often not achievable and dynamic PET images (i.e. multiple PET images over time) and more sophisticated quantification methods are required. A common strategy is to establish a model which considers the PET signal as being formed by separate compartments. These compartment models try to estimate the concentration of a given radioligand within each compartment as well as the rate constants (i.e. the speed at which the radioligand is exchanged from one compartment to another) governing the dynamics between the compartments. One of the most common models is the two-compartment model which compares a non displaceable compartment, containing uninteresting background signal, and a specific compartment, containing the signal of interest. The non displaceable signal is often obtained from the plasma concentration of blood samples and is seen as the gold standard reference. However, blood samples often need to be taken from arterial blood, something which is inconvenient to implement and cumbersome to the participant. In the cases where a brain region devoid of the target exists, it is also possible to use the signal from that region as a reference, rather than using the signal from plasma. The selection of an appropriate reference region is critical and in some cases might be ambiguous [41]. For all the kinetic modeling performed in this thesis, we have used a two compartments model with a reference region named MRTM2 [42]. This model first identifies the output rate constant of the reference region, k_2, using another form of the model called MRTM0; this model uses the signal from the reference region and signal from a region with high binding to obtain the best estimate of k_2. The rate constants in

other regions with lower binding (and usually containing more noise) are similarly estimated, but the constant k_2 estimated from the high-binding regions is reused, hence avoiding its estimation with a more noisy signal. The estimation of the rate constants is performed with a multilinear regression and was shown to be more robust to noise compared to similar models [42].

Magnetic Resonance Imaging

Principles and Acquisition

Magnetic resonance imaging (MRI) is an imaging technique that measures the collective signal generated by the magnetic moment of molecules to study structural and functional characteristics of tissues. A spin is a quantum property of subatomic particles which defines an angular momentum along an axis. For particles such as protons, this spin can have two states, up or down, which also correspond to high or low energy levels. In an atom with an even number of particles in the nucleus (e.g. ^{12}C), the spins are at equilibrium, but when the number of particles is uneven (e.g. ^{1}H) the atom has a non-null net spin and a corresponding magnetic moment.

In a natural environment, the high and low energy spins of protons freely moving within tissue are at equilibrium, hence there is no net magnetic moment. However, when placed in a strong magnetic field, a fraction of the low energy spins align with the magnetic field resulting in a net polarization vector parallel to the axis of the magnetic field. The application of a radio frequency (RF) pulse at the resonant (Larmor) frequency increases the angular momentum of the spin of protons and changes the angle of the net polarization vector. The protons will then be rotating at an angle with the axis of the strong magnetic field and the speed at which they rotate will be proportional to the strength of the magnetic field. Typically, a pulse tipping the net polarization vector by 90° or 180° is used. After receiving a pulse, the net polarization vector will relax back to its original configuration over a period of time. The time taken by the longitudinal (parallel to the main magnetic field) and transverse (perpendicular to the main magnetic field) parts of the net polarization vector to revert back to the original configuration (relaxation) follows an exponential process, and the time constant governing these processes are referred to as T1 and T2, respectively. These relaxation constants are influenced by the nature of the tissue in which the protons are located; typically, the less dense the tissue is, the faster the net polarization vector can revert back to its original state and the larger the relaxation constant will be.

After the application of a RF pulse, the transverse part of the net polarization vector generates

an alternating magnetic field which can induce a current in receiver coils. The quantification of the current induced in the receiver coils forms the signal acquired by an MRI scanner, hence all MRI sequences rely on strategies to transform parts of the net polarization vector onto the transverse axis. For example, in T1-weighted sequence first a 90° RF pulse is applied, and then after some waiting time (repetition time), another pulse is applied to transfer the longitudinal component onto the transverse axis where it can be quantified. As the precession speed of a proton is linearly related to the strength of the magnetic field in which it is placed, it is possible to target a specific spatial location with a RF pulse by applying a magnetic gradient varying linearly in space, a process called slice selection. Linear gradients along the remaining axis can be used to encode phase information within the slice, by turning a gradient on and off after the application of the RF pulse, and to encode frequency information by applying a gradient along the remaining axis during the acquisition of the MR signal. Frequency and phase information form the axes of k-space and, using methods such as inverse Fourier transformation, can be used to create images of the 2D slices from which a full 3D volume can be reconstructed.

MRI sequences quantifying T1 and T2 relaxation are nowadays used to acquire high resolution structural images where there is contrast between tissue types due to their different composition (hence different associated relaxation constant). It is also possible to capture neuronal activity with MRI, a technique known as fMRI, by imaging the blood-oxygen-level-dependent signal (BOLD) over time. Neuronal activity consumes energy and to meet that energy demand a process termed hæmodynamic response triggers a local dilation of blood vessel which results in a greater flow of oxygenated blood to the neurons. Red blood cells carrying oxygen, hemoglobin, are diamagnetic molecule. When they lose their oxygen, they become deoxyhemoglobin, a paramagnetic molecule which affects the local magnetic susceptibility in its surroundings and induces a loss in MR signal due to inhomogeneity in the magnetic field. Hence, an increase in oxygenated blood flow increases the ratio of hemoglobin to deoxyhemoglobin and results in an increase in MR signal. Thus, BOLD is used as an indirect measure to asses activation of a given brain area. As the T2 signal is highly influenced by magnetic field inhomogeneity, sequences sensitive to changes in T2*, the observed transverse relaxation signal of the T2 signal, are used to acquire BOLD fMRI images.

Resting-State Functional MRI

Functional MRI has been extensively used to study the brain response to active or passive tasks, hence probing the functional properties of the human brain. However, a specific application of fMRI which

has gained tremendous interest in the last decade is the study of the brain at rest, while not engaged in a task. Following the initial observation by [43] and the later formalization by [44, 45, 46] that some brain regions were synchronized when a subject was not engaged in a task and desynchronized when engaged led to the concept of a "default" network in the brain, termed the "default mode network". Subsequent studies of brain activity at rest with fMRI, a technique called resting-state fMRI (rs-fMRI), revealed a number of intrinsic, resting-state networks (RSN) believed to represent various aspects of the brain's functional organization [47].

An important aspect of rs-fMRI research concerns its methodology. A number of issues have been addressed since its inception; issues such as global signal regression [48], motion [49] and physiological artifacts [50] and significance testing [51] have been subjects of controversies in the field and required adjustments in the preprocessing and analysis procedures. Although there is now some consensus in the neuroimaging community on these issues, many different approaches are used to preprocess and analyze rs-fMRI data. Issues such as the number of existing RSNs or the low reproducibility at the subject-level still remain to be resolved.

Even though there are limitations to this technique, there are also viable analysis strategies that can be employed so that it can be a useful proxy for communication between brain areas. Practically, rs-fMRI research focuses on identifying changes in RSNs related to differences in brain state. By defining the connectivity between two regions as the amount of temporal correlation between their rs-fMRI signal, researchers have sought to identify changes in FC resulting from conditions such as neurological disorders or diseases.

FreeSurfer

FreeSurfer (FS, https://surfer.nmr.mgh.harvard.edu/)[52, 53, 54] is a state-of-the-art set of software tools for the analysis of neuroimaging data. It was initially developed to analyze morphometric properties of the human brain, such as cortical thickness and curvature, but was later extended to perform surface-based analysis of data such as fMRI, and more recently PET [55].

To obtain a model of the cortical surface of an individual, FS requires one or multiple T1-weighted MRI images. If multiple T1 images are provided, they are aligned and averaged to create an image with better signal-to-noise. FS then performs normalization of image intensities by correcting for the B1 field inhomogeneity and removes non brain tissue using a deformable model (skull stripping) [56]. Then, white matter (WM) voxels are identified and a surface of the pial/WM boundary is created for

each hemisphere; this is referred to as the WM surfaces. From these WM surfaces, pial surfaces are created by inflating the WM surfaces outward until the edge between gray matter and cerebrospinal fluid.

One of the main advantages of surface-based analysis over standard volume-based approaches is the ability to perform surface smoothing. Smoothing is a central preprocessing step in neuroimaging and it is especially critical in PET to limit the noise contribution in the kinetic modeling. However, the already large partial voluming effects intrinsic to PET images argue for limiting the amount of smoothing used in the images. By restricting smoothing to signal sampled from between the WM/pial surfaces, surface smoothing prevents the blurring of signal across tissue types and possibly gyri and hence prevents the introduction of additional partial voluming in the signal of interest.

To perform surface-based analysis, individual surfaces can be transformed to an average surface to perform group analysis. The transformation between the surfaces is a nonlinear mapping which matches curvature across surfaces while minimizing distortion of the original distance between vertices. In FS, the default normal surface is named *fsaverage* and consists of approximately 160,000 vertices for each hemisphere. Lower resolution versions of this normal surface, such as *fsaverage5* which has around 10,000 vertices, also exist. Moreover, when there is different contrast in GM and WM in a given modality, as is the case with all 5HT PET images, it is possible to use the WM surface model to perform accurate and robust registration between images from that modality and the structural image processed by FS by using boundary-based registration (BBR) [57]; BBR tries to align an image with the WM boundary such that the difference in intensity on each side of the surface is maximized over the whole WM surface.

FreeSurfer additionally performs labeling of subcortical structures in the volume [58, 59] and parcellation of the cortical surface into regions defined by the Desikan-Killiany atlas [11] presented in Figure 4. Recently, tools for the refinement of the brainstem segmentation [60] and hippocampus subfields [61] have been introduced in FS.
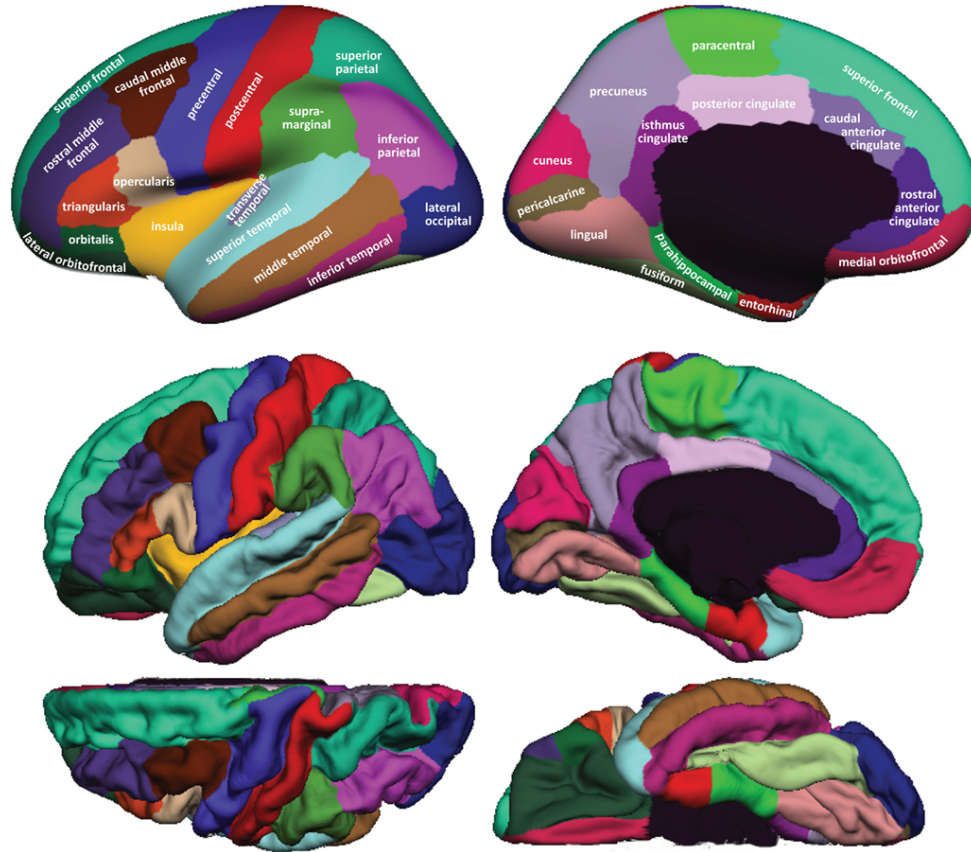
Figure 4. The Desikan-Killiany atlas (left hemisphere) on the inflated (top) and pial (middle and bottom) *fsaverage* surfaces. *Upper and middle*: left are lateral views and right are a medial views. *Lower*: left is a view from the top and right a view form the bottom. The figure was obtained from https://www.frontiersin.org/articles/10.3389/fnins.2012.00171/full, [62].

Messenger Ribonucleic Acid

Messenger ribonucleic acid (mRNA) is the copy of a specific gene from the DNA specifying a sequence of amino acids necessary for the construction of a protein. The mRNA genetic information is structured as a chain of codons, a sequence of three base pairs, where each codon encodes for a specific amino acid, except for the start and end codons which specify the initiation and termination of the protein synthesis. The translation of the mRNA, the process of synthesizing a protein, occurs within the ribosome in the cytoplasm or on the endoplasmic reticulum and requires additional transfer and ribosomal RNA. Although the translation of mRNA occurs mostly in the cell body, local translation in the dendrites and the axon of neurons are emerging as important regulatory mechanism of synaptic activity and neuronal functions [63, 64]. In this work, mRNA information on the 5-HT targets was

obtained from the Allen Human Brain Atlas, a high throughput effort which used in situ hybridization to quantify the mRNA levels of 62,000 genes across all brain structures. For the 5-HT system, the gene encoding the 5-HT$_{1A}$R, 5-HT$_{1B}$R, 5-HT$_{2A}$R, 5-HT$_4$R and 5-HTT are labeled *HTR1A*, *HTR1B*, *HTR2A*, *HTR4* and *SLC6A4*, respectively.

Linear Data Decomposition

Linear decomposition methods, also known as matrix factorization, are methods which attempt to identify latent features which can be linearly combined to explain the data. Methods such as singular value decomposition , independent component analysis, PARAFAC or dictionary learning are all matrix factorization algorithms which are optimizing different objective functions. In general terms, for a given data matrix $\boldsymbol{Y} \in \mathbb{R}^{n \times p}$, where n is the number of samples (e.g. voxels) and p the dimension of the data (e.g. subjects) linear decomposition methods seek to identify a matrix of k latent vectors $\boldsymbol{X} \in \mathbb{R}^{n \times k}$ which can be linearly composed such that

$$\boldsymbol{Y} = \boldsymbol{\beta}\boldsymbol{X} + \boldsymbol{E} \tag{1}$$

where $\boldsymbol{E}$ is an error term to be minimized. Factorization methods differ from each other by imposing different constraints for solving this problem. Given a data matrix $\boldsymbol{Y}$ where the column mean has been removed, PCA seeks to optimize the objective function

$$\underset{\boldsymbol{X}}{\operatorname{argmin}}(\|\boldsymbol{Y} - \boldsymbol{\beta}\boldsymbol{X}\|_F^2), \quad \text{with } \boldsymbol{X}^T\boldsymbol{X} = \boldsymbol{I} \tag{2}$$

In other words, PCA seeks to identify a set of orthogonal vectors such that the squared error (here equivalent to the variance) is minimized. The related ICA algorithms similarly aim to identify latent vectors minimizing the squared error while optimizing for maximum independence (often measured as mutual information or non-gaussianity) between the vectors.

When two or more dimensions (or modes) are common across multiple datasets (e.g. fMRI data normalized in space with a fixed task design), it is possible to exploit this structure in the factorization. Such a dataset is illustrated in Figure 5. The Parallel Factor Analysis (PARAFAC) model, also known as tensor rank decomposition, works similarly to PCA, but identifies common latent vectors across multiple datasets. Given a set of data $\boldsymbol{Y} = \{\boldsymbol{Y}_s\}$, the 3-way PARAFAC model (two common modes) seeks to identify $\boldsymbol{X}$ and $\boldsymbol{\beta}_s$ which optimizes

$$\underset{\boldsymbol{X}}{\operatorname{argmin}} \left(\sum_{Y_s \in Y} \|\boldsymbol{Y}_s - \boldsymbol{\beta}_s\boldsymbol{X}\|_F^2 \right) \tag{3}$$
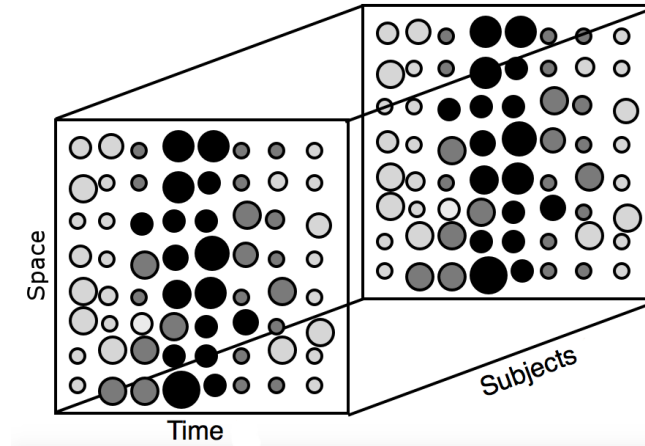
Figure 5: An example 3-way dataset where two modes (i.e. time and space) are repeated across the remaining dimension (i.e. subjects). Samples are represented by circles of varying magnitude and color.

Solving this problem can be done in many ways and in this thesis we considered the well-established variational inference framework. Variational inference performs a simplification of the fully Bayesian formulation of the problem which would otherwise be intractable. The Bayesian formulation allows for the use of priors to automatically infer the dimensionality (i.e. number of relevant components) of the problem. The traditional Variational Bayes (VB) formulation of PCA uses an automatic relevance determination (ARD) prior which tries to shrink to zero whole columns of the matrix X. Other types of priors, such as Jeffrey's prior, are sparse (SP) priors which try to shrink individual elements of X. In this work we have implemented the Variational Bayes formulation of PCA and PARAFAC with ARD priors, VB-PCA and VB-PARAFAC, and their sparse equivalent with Jeffrey's prior, SP-PCA and SP-PARAFAC.

Methods

All data used in this thesis was provided by the Cimbi database [9], with the exception of the fMRI data used in study III, which was part of a pilot study and kindly provided by Dr. Per Jensen. For all dynamic PET images, one or two corresponding T1-weighted MRI and, in most cases, a T2-weighted MRI were acquired.

FreeSurfer Processing

All T1-weighted MRI in study I & II were processed using FS's cortical reconstruction process, the so-called *recon-all*, producing subject-specific surfaces, cortical and subcortical labeling, including white matter, and transformation to the standard space in the volume (MNI305) and on the surface (fsaverage). First, all images were assessed to contain no large artifacts or anatomical abnormalities. If available, a T2-weighted structural MRI was used to improve the delineation of the pial surface by FS. In study I, no manual edits were performed and volume-based data was normalized to MNI305 space. In study II, manual edits to correct surface errors were carefully performed by two experts and volume data was normalized to MNI152 space using the combined surface and volume (CVS) registration [65]; this process is not ran by default by *recon-all*.

Dynamic PET Processing

All the dynamic PET images used in this thesis were acquired on a high resolution Siemens HRRT scanner, with an approximate in-plane resolution of 2mm [66] in the center of the field of view. Reconstruction of the PET data was performed using the 3D–OSEM–PSF algorithm with TXTV based attenuation correction [67, 68, 69]. Frames of the dynamic PET data were corrected for motion using AIR 5.2.5 [70]. In study I & II, the dynamic PET data, were then aligned with the structural MRI and subcortical regions were transformed to MNI305 or MNI152 and cortical regions were sampled onto individual subject's FS surface and transformed to the standard cortical surface *fsaverage*. Finally the dynamic data was smoothed correspondingly on the surface with a full width at half maximum (FWHM) Gaussian filter of 10 mm and in the volume with a FWHM Gaussian filter of 6 (Study I) or 5 (Study II) mm. Regional and vertex/voxel-wise kinetic modeling of the dynamic data was performed using the MRTM2 model to obtain non-displaceable binding potential (BP_{ND}) measures [42].

Study I

The central analysis performed in this study consisted of extracting DR and MR signal from the rs-fMRI and find which brain regions are associated with these signals. Data previously acquired by [71] was used. Initially, 63 subjects for which [^{11}C]DASB PET images, T1-weighted MRI and rs-fMRI images at baseline and rescan were available were considered in the analysis. FreeSurfer was used to preprocess the anatomical and functional data. The rs-fMRI data was preprocessed and vertex/voxel-wise FC was assessed using a general linear model (GLM). Subsequently, to investigate the association between the extent of FC between a region of the brain with the raphe nuclei and the corresponding density of 5-HTT, we performed a linear regression between FC measures and BP for each subject and evaluated whether the regression slopes were significantly different from 0. The 5-HTT BP$_{ND}$ were obtained as described above.

Preprocessing and analysis of functional MRI

The raphe nuclei are small structures embedded close to prominent sources of noise. Hence, in this study special care was given to the correct alignment of the fMRI data with the anatomy and the removal of physiological artifacts and other sources of noise. A standard preprocessing workflow was applied to prepare the subcortical data in the volume and the cortical data on the surface: the images were motion corrected, aligned with the structural image, projected to standard space and smoothed on the surface and in the volume with a FWHM Gaussian filter of 10 and 6 mm, respectively. However, some preprocessing steps not commonly considered in rs-fMRI were also applied. A correction for inhomogeneity in the B0 field [72] was applied to the structural image used with the fMRI to improve its alignment with the functional data. Furthermore, physiological and other sources of noise were removed in two steps. First, PESTICA v2 [73] was applied to identify and remove contributions from cardiological and respiratory signals. Secondly, principal sources of variation from signal in white matter and cerebrospinal fluid, and additionally signal from the 4th ventricle were included as nuisance regressor in the first-level analysis GLM. Within the model, frames flagged as containing too much motion were censored and subjects where 10% or more of the total number of frames were flagged were removed from the analysis. In total, 14 subjects were excluded.

The association between DR and MR signal was evaluated for every vertex/voxel at the subject-level using GLMs. Then, a group-level analysis was performed by evaluating at every vertex/voxel, using a two-tailed t-test, if the mean of the regression coefficients obtained from the subject-level

GLMs at that location was different from 0. Correction for multiple comparison (vertex/voxel threshold of $p = 0.001$ and cluster threshold of $p = 0.05$) was performed and the final clusters significantly related to DR and MR were identified.

Delineation of the Dorsal and Median Raphe Nuclei

Delineating the raphe nuclei can be challenging [74] as they are not visible on structural MRI due to their heterogeneous composition. Here we adopted a multimodal strategy to delineate these nuclei, leveraging the high density of 5-HTT within the nuclei. Mean time-weighted images of the [^{11}C]DASB PET images were created and T1-weighted MRI were used to define anatomical landmarks of the cerebral aqueduct, 4th ventricle and brainstem on these images. Then, the voxel with maximum intensity within the region formed by the landmarks was identified and defined as the center of the ROI defining DR; neighboring voxels with highest intensity and within the boundaries of the anatomical landmarks were then incrementally added one at a time, hence growing the ROI, until a predetermined target volume of 115 mm^3 was reached. Then, the same strategy was adopted to delineate the MR, while using the DR as an upper anatomical boundary and a target volume of 64 mm^3. Figure 6 outlines the delineation outcome.
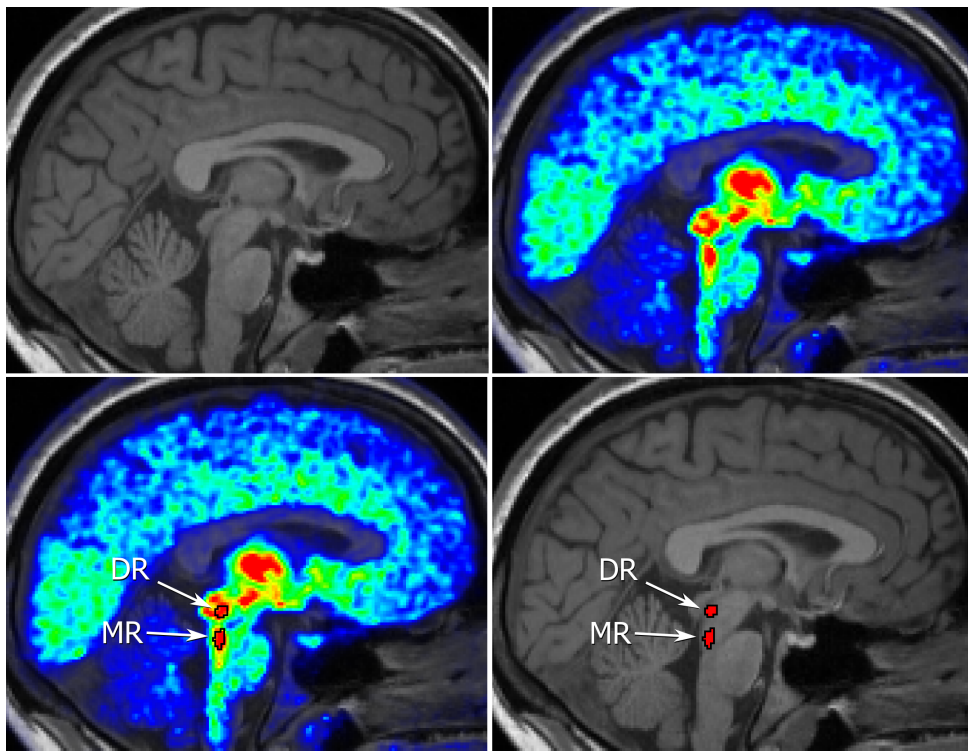

Figure 6: Delineation of the DR and MR on T1-weighted MRI using a [^{11}C]DASB image.

Study II

The main methodological challenge in this study was to validate the new processing pipeline for PET data within FS. This study included all PET data from healthy participants of the Cimbi database aged between 18 and 45 years, a total of 232 PET scans from 210 individuals. The target receptors were $5-HT_{1A}R$, $5-HT_{1B}R$, $5-HT_{2A}R$ and $5-HT_4R$ and the transporter 5-HTT which were images with the radioligand [^{11}C]Cumi-101, [^{11}C]AZ10419369, [^{11}C]Cimbi-36, [^{11}C]SB207145 and [^{11}C]DASB, respectively.

To perform the processing of the PET data within FS, the T1-weighted and PET images were processed as described above. A linear model was then used to evaluate the association between the regional BP_{ND} values and autoradiography measures from the literature [7, 6]. This association was used to transform the BP_{ND} values derived from the PET data into comparable density values. Subsequently, we investigated the linear association between regional density values and mRNA intensities obtained from the Allen Human Brain Atlas (AHBA, http://human.brain-map.org/, [75, 76]) Finally, we tested for effects of gender or age using a linear mixed effect model.

mRNA data from the Allen Human Brain Atlas

Previous work from [75] processed the mRNA data and assigned a summary values to each region defined in FS's Desikan-Killiany atlas. To create summary values, [75] first obtained the average mRNA levels for each of the genes of interest within each cortical probe. Then, they assigned each of the probe to a region of the Desikan-Killiany atlas and for each gene, each region and each subject they obtained median regional values across all probes. Finally, they calculated median values across all subjects for each gene and each region to obtain the final summary values. In this study we used this data directly as regional cortical values, and extended the procedure to subcortical regions. The only difference adopted in our approach was to directly use the labels assigned by the AHBA to each sample, rather than inferring a label based on the anatomical location of the probes.

Cerebellum segmentation

A particular methodological issue which arose in this project concerned the segmentation of the cerebellum. It has been shown that cerebellar vermis contains $5-HT_{1A}R$ and possibly other 5-HT receptors and may not be a suitable reference region. Hence, we adopted a procedure to label and remove vermis from the cerebellum segmentation of FS used for the kinetic modeling of PET data. The software

SUIT 2.7 [77] in combination with SPM12 (http://www.fil.ion.ucl.ac.uk/spm) was used to segment vermis and cerebellum. The final cerebellum segmentation was created by taking the intersection of the segmentation provided by SUIT, without vermis, and the cerebellar gray matter segmentation provided by FS. Although FS provides greater detail in the delineation of gray and white matter tissue compared to SUIT, it sometimes overlabels peripheral tissue. By limiting the final segmentation to the intersection of the labels provided by the two algorithms, we were able to overcome these limitations. This procedure formed the basis for an evaluation of the cerebellum and especially vermis as reference region for kinetic modeling in a related paper [1].

Study III

The methodological aspect of this study firstly consisted of deriving the algorithms for VB-PARAFAC and SP-PARAFAC (VB-PCA and SP-PCA were previously derived in [78]) and implementing VB-PCA, SP-PCA, VB-PARAFAC and SP-PARAFAC. Then, we evaluated the algorithms against each other through simulation and by using PET and fMRI data. Stability and reproducibility of the solutions were assessed using the RV coefficient [79] and the average correlation coefficient between the components, where optimal pairing was determined using the Hungarian algorithm [80] to optimize correlation.

The simulation was performed by creating a 3-way dataset where three sparse ground truth vectors were arbitrarily generated and linearly mixed to create five groups with random means, scalings and additive Gaussian noise for each group. The different decomposition algorithms where then applied to the simulated data and compared to the ground truth components.

We then performed an exploratory decomposition of dynamic PET data using the four models implemented in this study, and additionally a non probabilistic version of the PARAFAC model implemented in the N-WAY toolbox 3.21 [81]. We reused the data from 4 subjects scanned with [^{11}C]Cumi-101 in study II. This choice was motivated by the good temporal alignment of the PET data for these subjects. The preprocessing was done as described in Study II, however, the data was processed in the volume only and was normalized to MNI152 space and smoothed using a 5mm FWHM Gaussian filter. The stability and reproducibility of the solutions was assessed and qualitatively compared.

Finally, we applied the models to fMRI data. The dataset was composed of 8 scans of a block-design where subjects were instructed by visual cue to close and open their fist for 10 seconds at approximately 1 Hz, followed by a rest period of 10 seconds and repeated 10 times. The preprocessing

of fMRI data was performed using the standard work flow within FSL 5.0.9 [82]. The fMRI data was motion corrected using MCFLIRT [83] and aligned with the structural image using FLIRT [83], normalized to standard MNI152 space using FNIRT [84] and smoothed with a 8mm FWHM Gaussian filter. Here again we applied the four models implemented in this study to the data and the non probabilistic PARAFAC algorithm from the N-WAY toolbox. Additionally, we applied the tensor extension of the probabilistic independent component analysis (PICA) algorithm, as implemented by Melodic [85]. PICA is one of the most well-know dimensionality reduction tools for fMRI and formed a gold-standard to benchmark our algorithms.

Results

Study I

The main outcome of study I showed which brain regions are functionally connected with DR and MR in the human brain at rest. Figure 7 and the accompanying Tables 1 and 2 present the significant clusters that were observed. Interestingly, striking similarities can be seen between the FC maps for DR and MR. As a post hoc analysis, we investigated the association between FC levels and BP_{ND} measures and found a significant positive association for both DR and MR.
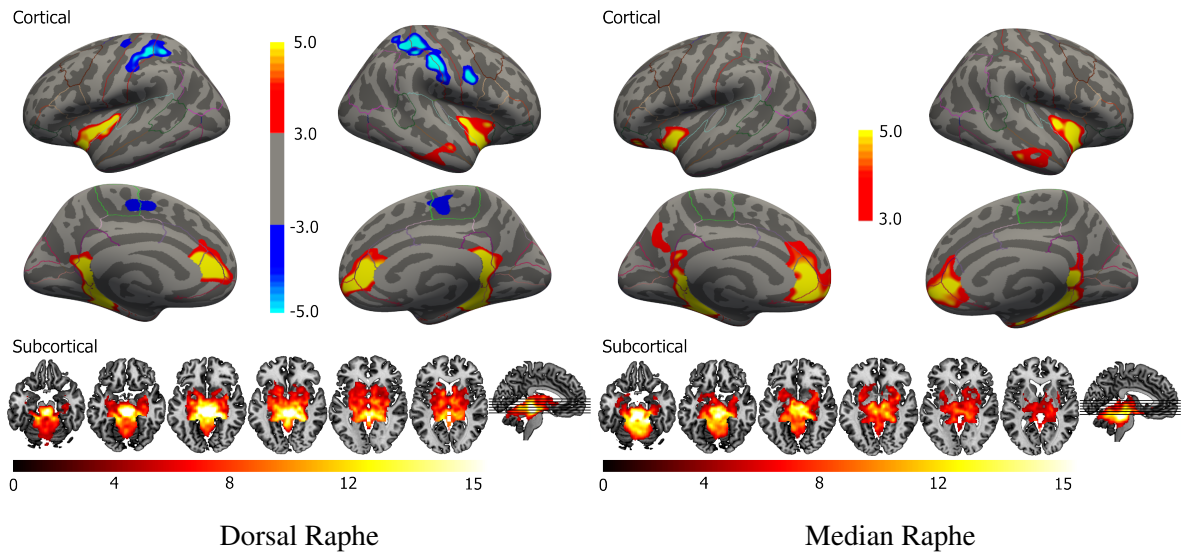

Figure 7: P-value maps $(-\log_{10}(p))$ of brain regions significantly associated with the DR and MR, after correction for multiple comparison.

Region	Cluster p-value	Size (mm^2)	MNI		
			X	Y	Z
Positive FC					
Left cortical hemisphere					
Parahippocampal gyrus	0.0001	1581	−18	−39	−6
Insula	0.0001	1040	−34	−16	−6
Rostral anterior cingulate gyrus	0.0001	805	−6	37	8
Right cortical hemisphere					
Parahippocampal gyrus	0.0001	1737	19	−35	−9
Medial orbitofrontal gyrus	0.0001	1073	14	43	−3
Insula	0.0001	1043	38	−4	−12
Superior temporal gyrus	0.0003	486	48	−12	−18
Negative FC					
Left cortical hemisphere					
Postcentral gyrus	0.0001	1337	−39	−33	47
Precentral gyrus	0.0112	295	−34	−22	58
Superior frontal gyrus	0.0121	291	−7	−7	51
Right cortical hemisphere					
Superior parietal gyrus	0.0001	2181	32	−44	48
Precentral gyrus	0.0037	359	57	7	29
Paracentral gyrus	0.0122	289	12	−19	47
Region	Cluster p-value	Size (mm^3)	MNI		
			X	Y	Z
Subcortical					
Brainstem	<0.0001	197,264	−29	−11	27

Table 1. Significant clusters functionally connected with the DR at rest.

Region	Cluster p-value	Size	MNI		
		(mm^2)	X	Y	Z
Left cortical hemisphere					
Rostral anterior cingulate gyrus	0.0001	2393	−6	41	−1
Parahippocampal gyrus	0.0001	1811	−28	−36	−16
Insula	0.0001	765	−30	13	−13
Precuneus	0.0042	361	−7	−68	30
Lateral orbitofrontal cortex	0.0140	278	−35	33	−10
Right cortical hemisphere					
Parahippocampal gyrus	0.0001	2585	24	−29	−20
Rostral anterior cingulate gyrus	0.0001	1255	7	39	−1
Insula	0.0001	1104	36	8	−12
Middle temporal gyrus	0.0001	674	62	−23	−18
Region	Cluster p-value	Size	MNI		
		(mm^3)	X	Y	Z
Subcortical					
Brainstem	<0.0001	228,744	−35	−21	29

Table 2. Significant clusters functionally connected with the MR at rest.

Study II

Regional, surface and volume BP$_{ND}$ values were obtained for all subjects. We averaged regional values for each target and investigated the linear association with corresponding autoradiography density measures from the literature. We observed significant associations for all targets. Using the regression slopes from these associations, we transformed the BP$_{ND}$ into density values and created average cortical and subcortical density maps, presented in Figure 8 and Figure 9. These maps display shared spatial patterns, but also exhibit spatial features unique to only some of the targets. We tested for associations between age, gender or their interaction and density, but none was found.
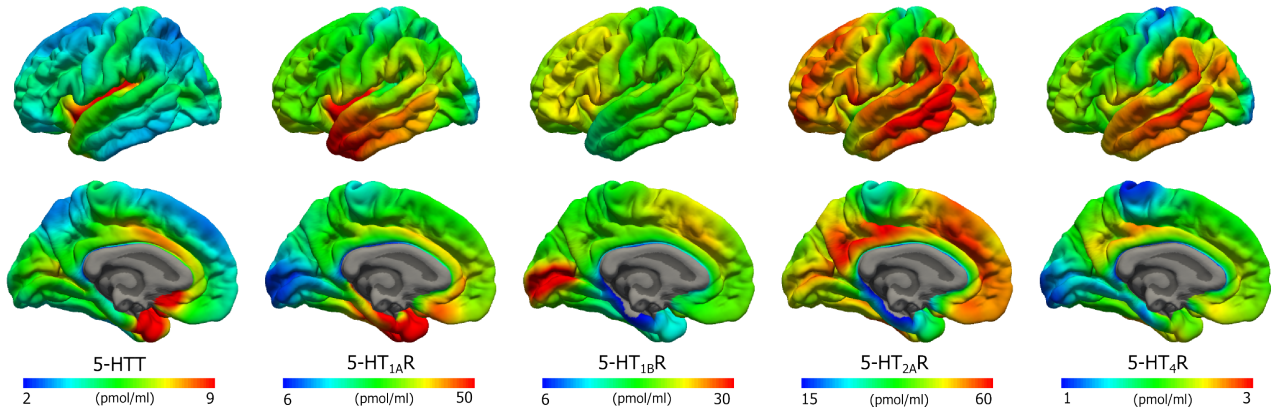
Figure 8: Average cortical density maps for the five 5-HT targets (left hemisphere).
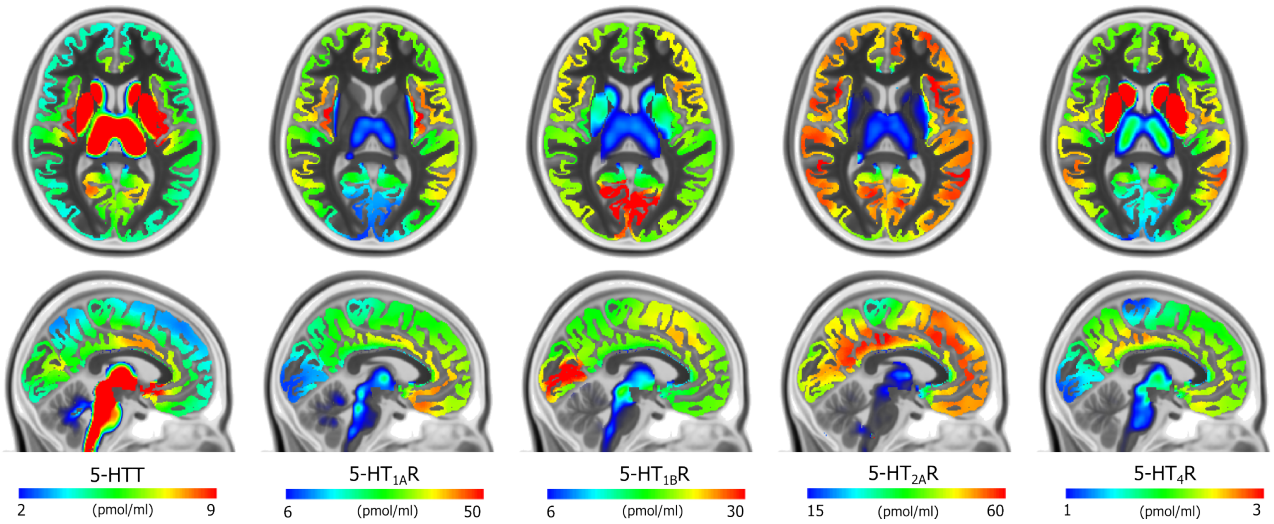

Figure 9: Average subcortical density maps for the five 5-HT targets.

Subsequently, we investigated the association between mRNA levels and density for the five targets; results are presented in Figure 10. For 5-HTT there was no significant association. The 5-HT$_{1A}$R showed a strong and significant association, including both cortical and subcortical regions. We observed a moderate association for the 5-HT$_{1B}$R and 5-HT$_{2A}$R in cortical regions; the subcortical regions deviated from the linear pattern exhibited by the cortical regions. Similarly, we observed a moderate association for the 5-HT$_4$R, but here the subcortical regions followed more closely the linear association observed for the cortical regions.
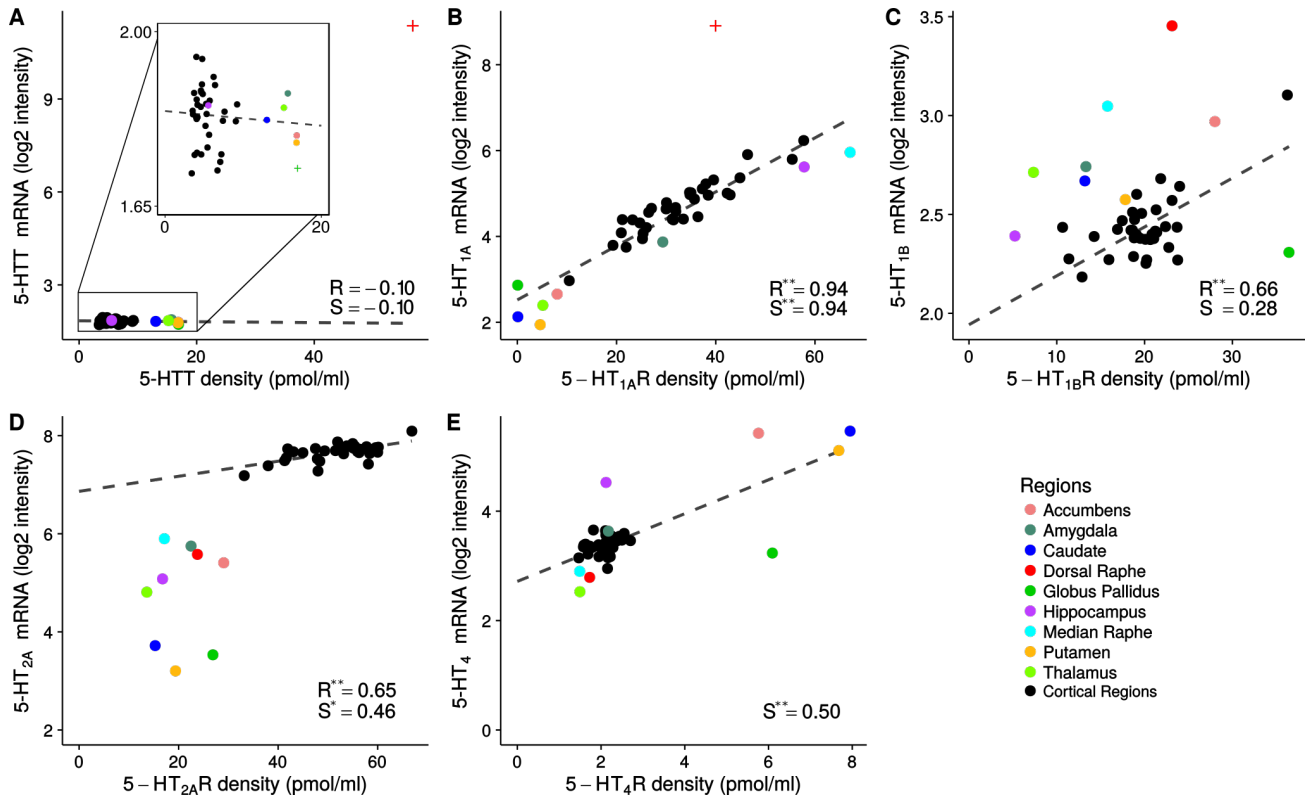
Figure 10: mRNA vs. density for the five 5-HT targets.

Study III

Components resulting from decomposing the simulated data with the Variational Bayes PCA and PARAFAC (VB-PCA and VB-PARAFAC) and their sparse formulation (SP-PCA and SP-PARAFAC), as well as a non probabilistic implementation of PARAFAC, are presented in Figure 11. All models were able to identify the predefined ground truth components used to create the simulated data, but to varying levels of accuracy. Both PCA type algorithms identified additional, unrelated components compared to ground truth. As expected, VB-PCA identified non sparse components while its sparse counterpart was able to prune smaller, non important weights. All PARAFAC models identified the true number of components with the correct ground truth patterns; SP-PARAFAC was however better at pruning unrelated weights.

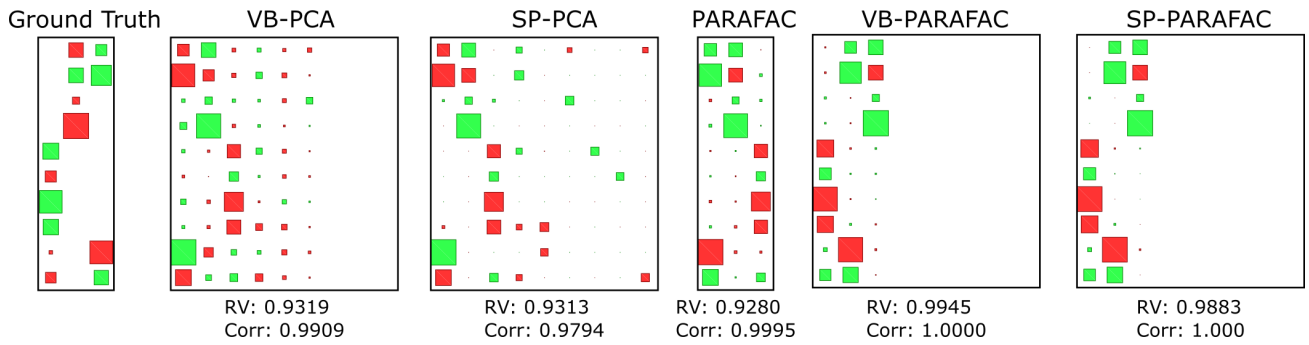| Ground Truth	VB-PCA	SP-PCA	PARAFAC	VB-PARAFAC	SP-PARAFAC
	RV: 0.9319	RV: 0.9313	RV: 0.9280	RV: 0.9945	RV: 0.9883
	Corr: 0.9909	Corr: 0.9794	Corr: 0.9995	Corr: 1.0000	Corr: 1.000

Figure 11: The ground truth components for the simulation and the components identified by the different algorithms when applied to the simulation data.

When applied to the PET data, the two first components identified by all algorithms were similar and the remaining components exhibited spatial patterns which appeared random. Figure 12 shows component 1 and 2 for the VB- and SP-PARAFAC algorithms; the components identified by VB-PCA and PARAFAC were similar to those of VB-PARAFAC and the ones from SP-PCA were similar to those of SP-PARAFAC. Here the sparse algorithms did not isolate a specific brain region, as was hoped, but instead pruned small weights in an apparent random pattern. We compared the fit of the models to PET activity within different brain regions and all algorithms yielded comparable outcomes.
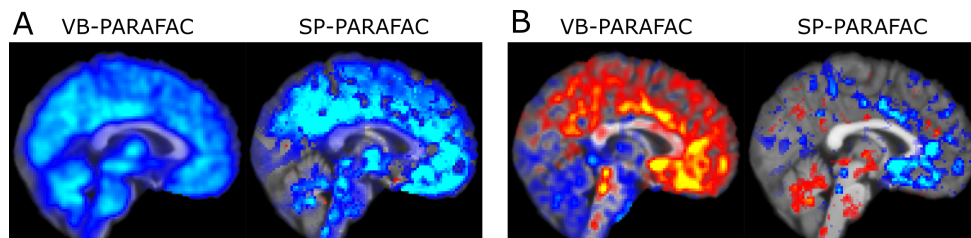

Figure 12: The first (left) and second (right) components identified by the VB-PARAFAC and SP-PARAFAC algorithms.

The fMRI data was processed with all the algorithms and the significance maps for selected components obtained with the different algorithms are presented in Figure 13. The fMRI task performed here is known to produce ipsilateral activation and contralateral deactivation of the motor cortex and activation of the visual cortex, due to the use of visual cues. Here, this pattern was well captured by tensor PICA. Only one relatively noisy component including activation in visual and motor cortex was captured by the non probabilistic PARAFAC model. This pattern was similar for both sparse algorithms, although motor activation appeared more defined in SP-PARAFAC and was mostly absent in SP-PCA. Both VB based algorithms identified components with motor and visual activation, but were

not able to segregate the loading for the corresponding brain regions onto different components, as was done by PICA, nor did they identify contralateral deactivation.
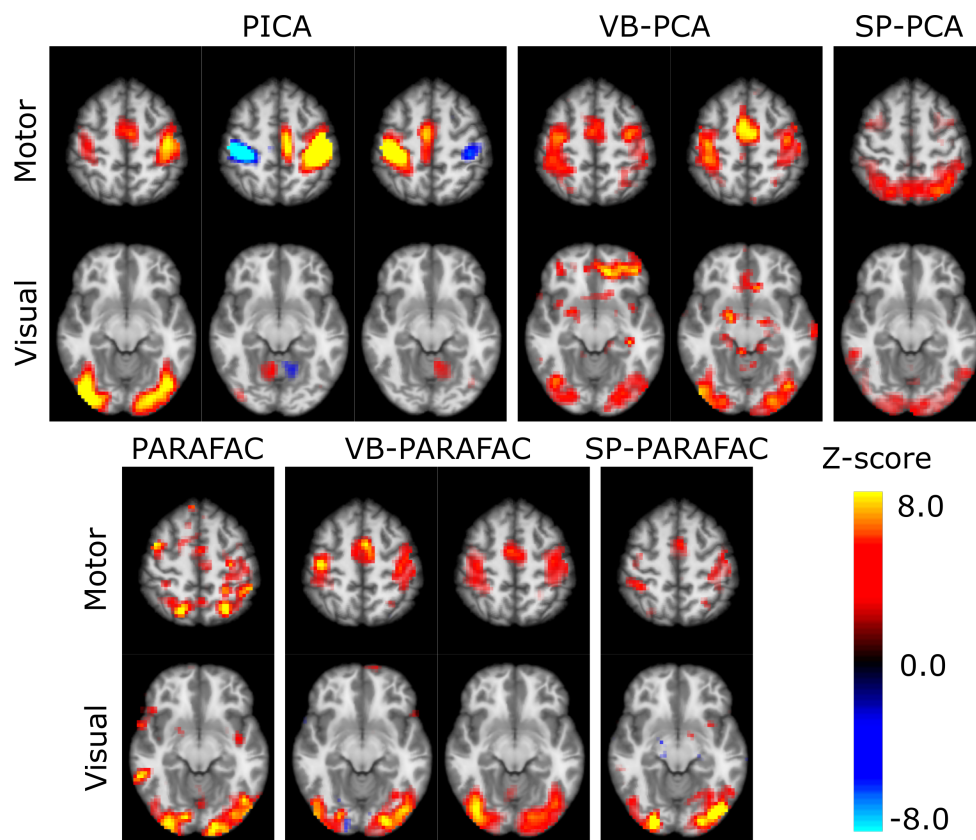

Figure 13: Selected visual and motor components identified by the different algorithms applied on the fMRI dataset.

Discussion

Study I

The clusters observed in Figure 7 represent brain regions functionally connected with our DR and MR seeds. We observed an association between raphe FC and 5-HTT BP_{ND} suggesting that the signal from DR and MR can be partly explained by features of the 5-HT system.

Interestingly, DR and MR are known to project mostly to separate, non overlapping regions of the brain [21, 86]. However, they do share substantial amount of afferent projections [2]. Given the striking similarity of the DR and MR FC maps, this suggests that the FC we have observed is largely modulated by inputs to the raphe nuclei. Regions such as the mPFC have been shown to have direct projections to the DR [87], and dysregulation of the mPFC has been implicated in a number of disorders related to the 5-HT system such as anxiety, stress and depression [88, 89]. Recent findings have also shown that some of the regions functionally connected to DR and MR show an increase in 5-HTT BP_{ND} after the administration of SSRI [90] in depressed patients. Notably, a recent study in the rat which performed direct stimulation of serotonergic neurons via a technique termed chemogenetic fMRI has also detected an increase in cerebral blood volume in most of the brain regions observed in our study [91]. These observations substantiate the idea that the DR and MR FC maps presented here may truly capture functional aspects of the 5-HT system.

However, although all efforts were made to obtain a purely serotonergic seed signal, it is difficult to assess the extent to which this is uniquely captured. Indeed, as previously stated, the raphe nuclei consist of an heterogeneous composition of cells which are largely serotonergic, but also contain other types of neurotransmitters [19]. Furthermore, it is reasonable to assume that the DR signal might be contaminated by signal of proximal regions such as the periaqueductal gray, a region involved in nociception; this may partly explain the negative correlations in somatosensory cortex observed for DR [92].

Study II

The high resolution 5-HT atlas created in this study highlights structural features of the 5-HT system. This atlas complements and extends earlier work on similar data of relatively lower resolution [8]. The strong associations between our *in vivo* BP_{ND} values and the autoradiography measures from the literature, across all targets, support the validity of PET imaging as a informative proxy for the underlying

5-HT receptor densities. By transforming the BP_{ND} values into densities it is hence possible to directly compare the distributions of different receptors. However, it is to be noted that the autoradiography came from relatively older patients and this has to be considered when interpreting the density values reported in this work.

An interesting novel aspect of this study is the evaluation of the spatial correspondence between mRNA levels and the density of the associated 5-HT proteins. Although most of these associations were previously observed, some of the targets were here investigated for the first time in humans. Furthermore, the spatial correspondence of mRNA samples and density values to regions of an atlas in a normalized space offers for the first time a uniform view of the 5-HT targets considered in this study. For 5-HTT, there was no significant association between mRNA and density, consistent with the fact that most of the mRNA for 5-HTT is located within the raphe nuclei [93]. This suggests that neocortical expression of 5-HTT outside of the raphe nuclei is linked to localized mRNA brought by axonal transport, and is independent of the local levels of mRNA. The neocortical expression of 5-HTT may then possibly reflect some localized regulation of a neurological process, such as observed by [94]. The $5-HT_{1A}R$ showed a strong association between mRNA levels and receptor density, supporting the well-known postsynaptic localization of this receptor. The remaining $5-HT_{1B}R$, $5-HT_{2A}R$ and $5-HT_4R$ receptors showed moderate associations. Remarkably, the subcortical regions for $5-HT_{1B}R$ and $5-HT_{2A}R$ did not follow the linear association of the cortical regions, indicating intrinsic differences in the synaptic localization of the receptors between cortical and subcortical regions.

Study III

The goals of this study were to develop probabilistic PARAFAC models to extract features indicative of dynamic properties of the PET data and to evaluate their usefulness for the modeling of fMRI data. The simulation clearly indicated that the algorithms performed as expected. VB-PCA and SP-PCA were able to identify the ground truth components, but were more sensitive to noise compared to their PARAFAC counter parts and identified additional, unrelated components. Conversely, the PARAFAC algorithms were both able to identify the correct number of components, but the SP-PARAFAc was better at pruning remaining unrelated weights compared to VB-PARAFAC. In both cases, the sparse algorithms were better at pruning unrelated weights compared to their VB counter part.

Even though the models performed as expected on simulated data, their application on dynamic PET data did not yield the desired results. In all cases, the algorithms yielded two components which

mapped throughout the brain and additional random components. Although this was an exploratory analysis, we had hoped to extract components which were loaded on specific, sparse brain regions. These results are however consistent with the compartmental approach used in kinetic modeling; here the models identified two basis functions which can be linearly mixed to obtain the temporal PET activity of any brain region. Similarly, the standard kinetic models used for this data uses a two compartment model (e.g. MRTM2), with some of the rate constant usually fixed using a reference and a high binding region [42]. Despite the fact that the models investigated here all achieved a good and comparable fit of the data, a solution rooted in the understanding of the underlying physiology may be preferable. Furthermore, although great efforts are usually made to achieve the same framing for all dynamic PET scans of a given radioligand, small deviations are critical to our PARAFAC model. Unfortunately, when considering the PET data from study II, the PARAFAC model would not be directly applicable due to timing variation between the injection of the radioligand and the start of the scanner acquisition; temporal alignment of the PET frames would hence require substantial interpolation, which is to be critically avoided.

When applied to fMRI data, the models considered here did not perform as well as tensor PICA in term of identifying components where brain regions with different functions are uniquely loaded and in identifying contralateral deactivation. This inadequate performance of the models can be linked to a number of factors such as mismatches between the presentation of the visual cue and the subject's response or changes in the dynamic of the BOLD signal across patients beyond simple scaling. Hence these results indicate that the PCA and PARAFAC models used here are inappropriate for the modeling of fMRI signal across subjects and that more flexible models such as ICA are to be preferred.

Concluding remarks and future perspectives

Study I suggests that raphe FC captures functional features of the 5-HT system related to the 5-HTT density. Hence, raphe FC may represent a useful biomarker for probing the 5-HT system, however further studies investigating its sensitivity to 5-HT related disease states are required. One of the main features of this biomarker would be that it does not require costly PET imaging and could be obtained directly from rs-fMRI. However, a few challenges need to be solved for this to happen. Firstly, a replication of the raphe FC maps is critical to ensure the validity of the method. Furthermore, a method for the delineation of the raphe nuclei independent of PET imaging is crucial for the wide-spread investigation of raphe FC. ICA based methods [95, 96] have shown promising results in that respect, but further validation is warranted. Finally, rs-fMRI acquired at high field strength (e.g. 7T) and at a higher sampling frequency should be considered to prevent partial voluming effects and to allow for a better separation between the signal of interest and physiological artifacts.

The atlas presented in study II shows one of the most complete pictures yet of the structural organization of the 5-HT system. It clearly outlines brain regions with unique characteristics in term of 5-HT receptor density and possibly distinct brain functions. Current structural atlases, such as the Desikan-Killiany atlas, do not define regions of homogeneous 5-HT receptor density. As part of future work, the data used in study II will be leveraged to obtain a parcellation of cortex specific to the 5-HT system where regions of homogeneous density will be better captured. Hence, we hope that this new parcellation will be more sensitive to regional changes affecting the 5-HT system.

In study III we successfully derived and implemented two probabilistic PARAFAC algorithms. When applied to the dynamic PET data, the algorithms yielded two latent vectors which were mapped throughout all of the brain rather than onto discrete brain regions. This indicates that the dynamic information of the PET data does not reveal additional information which can be used for parcellating the brain and that using a summary measures such as binding potential may be sufficient for that purpose. We have also shown that the application of the algorithms to fMRI data does not improve over one of the state-of-the-art technique used for that modality. Nonetheless, these algorithms may still prove to be very useful in other contexts assuming that the underlying model assumptions are respected. Furthermore, the variational Bayes framework is a very powerful framework and the experience gained in this work can potentially be extended to other types of algorithms such as dictionary learning.

In conclusion, we have introduced a novel tool for the study of functional properties of the 5-

HT system, derived a high resolution description of its structure and investigated the application of advanced modeling strategies to generate a parcellation of the brain specific to that system. Hence, the work presented in this thesis furthers our knowledge and understanding of the 5-HT system and opens new avenues of investigation.

References

[1] R. P. Vertes, S. B. Linley, Efferent and afferent connections of the dorsal and median raphe nuclei in the rat, in: Serotonin and sleep: molecular, functional and clinical aspects, Springer, 2008, pp. 69–102.

[2] I. P. Dorocic, D. Fürth, Y. Xuan, Y. Johansson, L. Pozzi, G. Silberberg, M. Carlén, K. Meletis, A whole-brain atlas of inputs to serotonergic neurons of the dorsal and median raphe nuclei, Neuron 83 (3) (2014) 663–678.

[3] R. M. Salomon, R. L. Cowan, B. P. Rogers, M. S. Dietrich, A. L. Bauernfeind, R. M. Kessler, J. C. Gore, Time series fmri measures detect changes in pontine raphe following acute tryptophan depletion, Psychiatry Research: Neuroimaging 191 (2) (2011) 112–121.

[4] R. M. Salomon, R. L. Cowan, Oscillatory serotonin function in depression, Synapse 67 (11) (2013) 801–820.

[5] J. J. Weinstein, B. P. Rogers, W. D. Taylor, B. D. Boyd, R. L. Cowan, K. M. Shelton, R. M. Salomon, Effects of acute tryptophan depletion on raphé functional connectivity in depression, Psychiatry Research: Neuroimaging 234 (2) (2015) 164–171.

[6] P. Bonaventure, H. Hall, W. Gommeren, P. Cras, X. Langlois, M. Jurzak, J. E. Leysen, Mapping of serotonin 5-ht4 receptor mrna and ligand binding sites in the post-mortem human brain, Synapse 36 (1) (2000) 35–46.

[7] K. Varnäs, C. Halldin, H. Hall, Autoradiographic distribution of serotonin transporters and receptor subtypes in human brain, Human brain mapping 22 (3) (2004) 246–260.

[8] M. Savli, A. Bauer, M. Mitterhauser, Y.-S. Ding, A. Hahn, T. Kroll, A. Neumeister, D. Haeusler, J. Ungersboeck, S. Henry, et al., Normative database of the serotonergic system in healthy subjects using multi-tracer pet, Neuroimage 63 (1) (2012) 447–459.

[9] G. M. Knudsen, P. S. Jensen, D. Erritzoe, W. F. Baaré, A. Ettrup, P. M. Fisher, N. Gillings, H. D. Hansen, L. K. Hansen, S. G. Hasselbalch, et al., The center for integrated molecular brain imaging (cimbi) database, Neuroimage 124 (2016) 1213–1219.

[10] K. Brodmann, Vergleichende Lokalisationslehre der Grosshirnrinde in ihren Prinzipien dargestellt auf Grund des Zellenbaues, Barth, 1909.

[11] R. S. Desikan, F. Ségonne, B. Fischl, B. T. Quinn, B. C. Dickerson, D. Blacker, R. L. Buckner, A. M. Dale, R. P. Maguire, B. T. Hyman, et al., An automated labeling system for subdividing the human cerebral cortex on mri scans into gyral based regions of interest, Neuroimage 31 (3) (2006) 968–980.

[12] B. T. Yeo, F. M. Krienen, J. Sepulcre, M. R. Sabuncu, D. Lashkari, M. Hollinshead, J. L. Roffman, J. W. Smoller, L. Zöllei, J. R. Polimeni, et al., The organization of the human cerebral cortex estimated by intrinsic functional connectivity, Journal of neurophysiology 106 (3) (2011) 1125–1165.

[13] M. F. Glasser, T. S. Coalson, E. C. Robinson, C. D. Hacker, J. Harwell, E. Yacoub, K. Ugurbil, J. Andersson, C. F. Beckmann, M. Jenkinson, et al., A multi-modal parcellation of human cerebral cortex, Nature 536 (7615) (2016) 171–178.

[14] J.-P. Hornung, The human raphe nuclei and the serotonergic system, Journal of chemical neuroanatomy 26 (4) (2003) 331–343.

[15] B. L. Jacobs, E. C. Azmitia, Structure and function of the brain serotonin system, Physiological reviews 72 (1) (1992) 165–229.

[16] I. Törk, Anatomy of the serotonergic system, Annals of the New York Academy of Sciences 600 (1) (1990) 9–34.

[17] K. Baker, G. Halliday, J.-P. Hornung, L. Geffen, R. Cotton, et al., Distribution, morphology and number of monoamine-synthesizing and substance p-containing neurons in the human dorsal raphe nucleus, Neuroscience 42 (3) (1991) 757–775.

[18] K. Baker, G. Halliday, P. Halasz, J.-P. Hornung, L. Geffen, R. Cotton, I. Törk, Cytoarchitecture of serotonin-synthesizing neurons in the pontine tegmentum of the human brain, Synapse 7 (4) (1991) 301–320.

[19] K. A. Michelsen, C. Schmitz, H. W. Steinbusch, The dorsal raphe nucleus—from silver stainings to a role in depression, Brain research reviews 55 (2) (2007) 329–342.

[20] R. P. Vertes, W. J. Fortin, A. M. Crane, Projections of the median raphe nucleus in the rat, Journal of Comparative Neurology 407 (4) (1999) 555–582.

[21] R. P. Vertes, S. B. Linley, Comparison of projections of the dorsal and median raphe nuclei, with some functional considerations, in: International Congress Series, Vol. 1304, Elsevier, 2007, pp. 98–120.

[22] A. R. Hariri, A. Holmes, Genetics of emotional regulation: the role of the serotonin transporter in neural function, Trends in cognitive sciences 10 (4) (2006) 182–191.

[23] L. M. Paterson, B. R. Kornum, D. J. Nutt, V. W. Pike, G. M. Knudsen, 5-ht radioligands for human brain imaging with pet and spect, Medicinal research reviews 33 (1) (2013) 54–111.

[24] C. L. Parks, P. S. Robinson, E. Sibille, T. Shenk, M. Toth, Increased anxiety of mice lacking the serotonin1a receptor, Proceedings of the National Academy of Sciences 95 (18) (1998) 10734–10739.

[25] R. J. Carey, G. DePalma, E. Damianopoulos, A. Shanahan, C. P. Müller, J. P. Huston, Evidence that the 5-ht 1a autoreceptor is an important pharmacological target for the modulation of cocaine behavioral stimulant effects, Brain research 1034 (1) (2005) 162–171.

[26] G. Gudelsky, J. Koenig, H. Meltzer, Thermoregulatory responses to serotonin (5-ht) receptor stimulation in the rat: evidence for opposing roles of 5-ht2 and 5-ht1a receptors, Neuropharmacology 25 (12) (1986) 1307–1313.

[27] Y. Ootsuka, W. W. Blessing, Activation of 5-ht1a receptors in rostral medullary raphe inhibits cutaneous vasoconstriction elicited by cold exposure in rabbits, Brain research 1073 (2006) 252–261.

[28] S. da Cunha-Bang, L. V. Hjordt, E. Perfalk, V. Beliveau, C. Bock, S. Lehel, C. Thomsen, D. Sestoft, C. Svarer, G. M. Knudsen, Serotonin 1b receptor binding is associated with trait anger and level of psychopathy in violent offenders, Biological psychiatry 82 (4) (2017) 267–274.

[29] E. Tatarczynska, A. Klodzinska, K. Stachowicz, E. Chojnacka-Wojcik, Effects of a selective 5-ht1b receptor agonist and antagonists in animal models of anxiety and depression, Behavioural pharmacology 15 (8) (2004) 523–534.

[30] R. L. Carhart-Harris, M. Bolstridge, J. Rucker, C. M. Day, D. Erritzoe, M. Kaelen, M. Bloomfield, J. A. Rickard, B. Forbes, A. Feilding, et al., Psilocybin with psychological support for treatment-resistant depression: an open-label feasibility study, The Lancet Psychiatry 3 (7) (2016) 619–627.

[31] D. Popa, C. Léna, V. Fabre, C. Prenat, J. Gingrich, P. Escourrou, M. Hamon, J. Adrien, Contribution of 5-ht2 receptor subtypes to sleep–wakefulness and respiratory control, and functional adaptations in knock-out mice lacking 5-ht2a receptors, Journal of Neuroscience 25 (49) (2005) 11231–11238.

[32] N. K. Popova, T. G. Amstislavskaya, 5-ht2a and 5-ht2c serotonin receptors differentially modulate mouse sexual arousal and the hypothalamo-pituitary-testicular response to the presence of a female, Neuroendocrinology 76 (1) (2002) 28–34.

[33] P. M. Fisher, C. C. Meltzer, J. C. Price, R. L. Coleman, S. K. Ziolko, C. Becker, E. L. Moses-Kolko, S. L. Berga, A. R. Hariri, Medial prefrontal cortex 5-ht2a density is correlated with amygdala reactivity, response habituation, and functional coupling, Cerebral cortex 19 (11) (2009) 2499–2507.

[34] P. M. Fisher, J. C. Price, C. C. Meltzer, E. L. Moses-Kolko, C. Becker, S. L. Berga, A. R. Hariri, Medial prefrontal cortex serotonin 1a and 2a receptor binding interacts to predict threat-related amygdala reactivity, Biology of mood & anxiety disorders 1 (1) (2011) 2.

[35] M. E. Haahr, P. Fisher, C. G. Jensen, V. Frokjaer, B. Mc Mahon, K. Madsen, W. Baaré, S. Lehel, A. Norremolle, E. A. Rabiner, et al., Central 5-ht4 receptor binding as biomarker of serotonergic tonus in humans: a [11c] sb207145 pet study, Molecular psychiatry 19 (4) (2014) 427.

[36] V. Compan, Y. Charnay, N. Dusticier, A. Daszuta, R. Hen, J. Bockaert, Feeding disorders in 5-ht4 receptor knockout mice, Journal de la Societe de biologie 198 (1) (2003) 37–49.

[37] R. S. Duman, A silver bullet for the treatment of depression?, Neuron 55 (5) (2007) 679–681.

[38] C. E. Hagan, R. A. Mcdevitt, Y. Liu, A. R. Furay, J. F. Neumaier, 5-ht1b autoreceptor regulation of serotonin transporter activity in synaptosomes, Synapse 66 (12) (2012) 1024–1034.

[39] M. K. Madsen, B. Mc Mahon, S. B. Andersen, H. R. Siebner, G. M. Knudsen, P. M. Fisher, Threat-related amygdala functional connectivity is associated with 5-httlpr genotype and neuroticism, Social cognitive and affective neuroscience 11 (1) (2015) 140–149.

[40] P. M. Fisher, K. K. Holst, D. Adamsen, A. B. Klein, V. G. Frokjaer, P. S. Jensen, C. Svarer, N. Gillings, W. F. Baare, J. D. Mikkelsen, et al., Bdnf val66met and 5-httlpr polymorphisms predict a human in vivo marker for brain serotonin levels, Human brain mapping 36 (1) (2015) 313–323.

[41] M. Ganz, L. Feng, H. D. Hansen, V. Beliveau, C. Svarer, G. M. Knudsen, D. N. Greve, Cerebellar heterogeneity and its impact on pet data quantification of 5-ht receptor radioligands, Journal of Cerebral Blood Flow & Metabolism (2017) 0271678X16686092.

[42] M. Ichise, J.-S. Liow, J.-Q. Lu, A. Takano, K. Model, H. Toyama, T. Suhara, K. Suzuki, R. B. Innis, R. E. Carson, Linearized reference tissue parametric imaging methods: application to [11c] dasb positron emission tomography studies of the serotonin transporter in human brain, Journal of Cerebral Blood Flow & Metabolism 23 (9) (2003) 1096–1112.

[43] G. L. Shulman, J. A. Fiez, M. Corbetta, R. L. Buckner, F. M. Miezin, M. E. Raichle, S. E. Petersen, Common blood flow changes across visual tasks: Ii. decreases in cerebral cortex, Journal of cognitive neuroscience 9 (5) (1997) 648–663.

[44] M. E. Raichle, A. M. MacLeod, A. Z. Snyder, W. J. Powers, D. A. Gusnard, G. L. Shulman, A default mode of brain function, Proceedings of the National Academy of Sciences 98 (2) (2001) 676–682.

[45] D. A. Gusnard, M. E. Raichle, Searching for a baseline: functional imaging and the resting human brain, Nature reviews. Neuroscience 2 (10) (2001) 685.

[46] D. A. Gusnard, E. Akbudak, G. L. Shulman, M. E. Raichle, Medial prefrontal cortex and self-referential mental activity: relation to a default mode of brain function, Proceedings of the National Academy of Sciences 98 (7) (2001) 4259–4264.

[47] M. P. Van Den Heuvel, H. E. H. Pol, Exploring the brain network: a review on resting-state fmri functional connectivity, European neuropsychopharmacology 20 (8) (2010) 519–534.

[48] K. Murphy, R. M. Birn, D. A. Handwerker, T. B. Jones, P. A. Bandettini, The impact of global signal regression on resting state correlations: are anti-correlated networks introduced?, Neuroimage 44 (3) (2009) 893–905.

[49] J. D. Power, K. A. Barnes, A. Z. Snyder, B. L. Schlaggar, S. E. Petersen, Spurious but systematic correlations in functional connectivity mri networks arise from subject motion, Neuroimage 59 (3) (2012) 2142–2154.

[50] G. H. Glover, T.-Q. Li, D. Ress, Image-based method for retrospective correction of physiological motion effects in fmri: Retroicor, Magnetic resonance in medicine 44 (1) (2000) 162–167.

[51] A. Eklund, T. E. Nichols, H. Knutsson, Cluster failure: why fmri inferences for spatial extent have inflated false-positive rates, Proceedings of the National Academy of Sciences (2016) 201602413.

[52] A. M. Dale, B. Fischl, M. I. Sereno, Cortical surface-based analysis: I. segmentation and surface reconstruction, Neuroimage 9 (2) (1999) 179–194.

[53] B. Fischl, M. I. Sereno, A. M. Dale, Cortical surface-based analysis: Ii: inflation, flattening, and a surface-based coordinate system, Neuroimage 9 (2) (1999) 195–207.

[54] B. Fischl, Freesurfer, Neuroimage 62 (2) (2012) 774–781.

[55] D. N. Greve, C. Svarer, P. M. Fisher, L. Feng, A. E. Hansen, W. Baare, B. Rosen, B. Fischl, G. M. Knudsen, Cortical surface-based analysis reduces bias and variance in kinetic modeling of brain pet data, Neuroimage 92 (2014) 225–236.

[56] F. Ségonne, A. M. Dale, E. Busa, M. Glessner, D. Salat, H. K. Hahn, B. Fischl, A hybrid approach to the skull stripping problem in mri, Neuroimage 22 (3) (2004) 1060–1075.

[57] D. N. Greve, B. Fischl, Accurate and robust brain image alignment using boundary-based registration, Neuroimage 48 (1) (2009) 63–72.

[58] B. Fischl, D. H. Salat, E. Busa, M. Albert, M. Dieterich, C. Haselgrove, A. Van Der Kouwe, R. Killiany, D. Kennedy, S. Klaveness, et al., Whole brain segmentation: automated labeling of neuroanatomical structures in the human brain, Neuron 33 (3) (2002) 341–355.

[59] B. Fischl, A. Van Der Kouwe, C. Destrieux, E. Halgren, F. Ségonne, D. H. Salat, E. Busa, L. J. Seidman, J. Goldstein, D. Kennedy, et al., Automatically parcellating the human cerebral cortex, Cerebral cortex 14 (1) (2004) 11–22.

[60] J. E. Iglesias, K. Van Leemput, P. Bhatt, C. Casillas, S. Dutt, N. Schuff, D. Truran-Sacrey, A. Boxer, B. Fischl, A. D. N. Initiative, et al., Bayesian segmentation of brainstem structures in mri, NeuroImage 113 (2015) 184–195.

[61] J. E. Iglesias, J. C. Augustinack, K. Nguyen, C. M. Player, A. Player, M. Wright, N. Roy, M. P. Frosch, A. C. McKee, L. L. Wald, et al., A computational atlas of the hippocampal formation using ex vivo, ultra-high resolution mri: application to adaptive segmentation of in vivo mri, NeuroImage 115 (2015) 117–137.

[62] A. Klein, J. Tourville, 101 labeled brain images and a consistent human cortical labeling protocol, Frontiers in neuroscience 6.

[63] H. Jung, B. C. Yoon, C. E. Holt, Axonal mrna localization and local protein synthesis in nervous system assembly, maintenance and repair, Nature reviews. Neuroscience 13 (5) (2012) 308.

[64] C. Glock, M. Heumüller, E. M. Schuman, mrna transport & local translation in neurons, Current Opinion in Neurobiology 45 (2017) 169–177.

[65] G. Postelnicu, L. Zollei, B. Fischl, Combined volumetric and surface registration, IEEE transactions on medical imaging 28 (4) (2009) 508–522.

[66] O. V. Olesen, M. Sibomana, S. H. Keller, F. Andersen, J. Jensen, S. Holm, C. Svarer, L. Højgaard, Spatial resolution of the hrrt pet scanner using 3d-osem psf reconstruction, in: Nuclear Science Symposium Conference Record (NSS/MIC), 2009 IEEE, IEEE, 2009, pp. 3789–3790.

[67] C. Comtat, F. Sureau, M. Sibomana, I. Hong, N. Sjoholm, R. Trebossen, Image based resolution modeling for the hrrt osem reconstructions software, in: Nuclear Science Symposium Conference Record, 2008. NSS'08. IEEE, IEEE, 2008, pp. 4120–4123.

[68] F. C. Sureau, A. J. Reader, C. Comtat, C. Leroy, M.-J. Ribeiro, I. Buvat, R. Trébossen, Impact of image-space resolution modeling for studies with the high-resolution research tomograph, Journal of Nuclear Medicine 49 (6) (2008) 1000–1008.

[69] S. H. Keller, C. Svarer, M. Sibomana, Attenuation correction for the hrrt pet-scanner using transmission scatter correction and total variation regularization, IEEE transactions on medical imaging 32 (9) (2013) 1611–1621.

[70] R. P. Woods, S. R. Cherry, J. C. Mazziotta, Rapid automated algorithm for aligning and reslicing pet images., Journal of computer assisted tomography 16 (4) (1992) 620–633.

[71] V. G. Frokjaer, A. Pinborg, K. K. Holst, A. Overgaard, S. Henningsson, M. Heede, E. C. Larsen, P. S. Jensen, M. Agn, A. P. Nielsen, et al., Role of serotonin transporter changes in depressive responses to sex-steroid hormone manipulation: a positron emission tomography study, Biological psychiatry 78 (8) (2015) 534–543.

[72] P. Jezzard, R. S. Balaban, Correction for geometric distortion in echo planar images from b0 field variations, Magnetic resonance in medicine 34 (1) (1995) 65–73.

[73] E. B. Beall, Adaptive cyclic physiologic noise modeling and correction in functional mri, Journal of neuroscience methods 187 (2) (2010) 216–228.

[74] G. S. Kranz, A. Hahn, M. Savli, R. Lanzenberger, Challenges in the differentiation of midbrain raphe nuclei in neuroimaging research, Proceedings of the National Academy of Sciences 109 (29) (2012) E2000–E2000.

[75] L. French, T. Paus, A freesurfer view of the cortical transcriptome generated from the allen human brain atlas, Frontiers in neuroscience 9.

[76] M. J. Hawrylycz, S. Lein, A. L. Guillozet-Bongaarts, E. H. Shen, L. Ng, J. A. Miller, L. N. Van De Lagemaat, K. A. Smith, A. Ebbert, Z. L. Riley, et al., An anatomically comprehensive atlas of the adult human brain transcriptome, Nature 489 (7416) (2012) 391.

[77] J. Diedrichsen, A spatially unbiased atlas template of the human cerebellum, Neuroimage 33 (1) (2006) 127–138.

[78] Y. Guan, J. G. Dy, Sparse probabilistic principal component analysis, in: International Conference on Artificial Intelligence and Statistics, 2009, pp. 185–192.

[79] P. Robert, Y. Escoufier, A unifying tool for linear multivariate statistical methods: the rv-coefficient, Applied statistics (1976) 257–265.

[80] J. Munkres, Algorithms for the assignment and transportation problems, Journal of the society for industrial and applied mathematics 5 (1) (1957) 32–38.

[81] C. A. Andersson, R. Bro, The n-way toolbox for matlab, Chemometrics and intelligent laboratory systems 52 (1) (2000) 1–4.

[82] M. Jenkinson, C. F. Beckmann, T. E. Behrens, M. W. Woolrich, S. M. Smith, Fsl, Neuroimage 62 (2) (2012) 782–790.

[83] M. Jenkinson, P. Bannister, M. Brady, S. Smith, Improved optimization for the robust and accurate linear registration and motion correction of brain images, Neuroimage 17 (2) (2002) 825–841.

[84] J. L. Andersson, M. Jenkinson, S. Smith, et al., Non-linear registration, aka spatial normalisation fmrib technical report tr07ja2, FMRIB Analysis Group of the University of Oxford 2.

[85] C. F. Beckmann, S. M. Smith, Tensorial extensions of independent component analysis for multisubject fmri analysis, Neuroimage 25 (1) (2005) 294–311.

[86] K. G. Commons, Two major network domains in the dorsal raphe nucleus, Journal of Comparative Neurology 523 (10) (2015) 1488–1504.

[87] M. R. Warden, A. Selimbeyoglu, J. J. Mirzabekov, M. Lo, K. R. Thompson, S.-Y. Kim, A. Adhikari, K. M. Tye, L. M. Frank, K. Deisseroth, A prefrontal cortex-brainstem neuronal projection that controls response to behavioural challenge, Nature 492 (7429) (2012) 428–432.

[88] A. Chocyk, I. Majcher-Maślanka, D. Dudys, A. Przyborowska, K. Wedzony, Impact of early-life stress on the medial prefrontal cortex functions–a search for the pathomechanisms of anxiety and mood disorders, Pharmacological Reports 65 (6) (2013) 1462–1470.

[89] D. Riga, M. R. Matos, A. Glas, A. B. Smit, S. Spijker, M. C. Van den Oever, Optogenetic dissection of medial prefrontal cortex circuitry, Frontiers in systems neuroscience 8.

[90] G. M. James, P. Baldinger-Melich, C. Philippe, G. S. Kranz, T. Vanicek, A. Hahn, G. Gryglewski, M. Hienert, M. Spies, T. Traub-Weidinger, et al., Effects of selective serotonin reuptake inhibitors on interregional relation of serotonin transporter availability in major depression, Frontiers in human neuroscience 11.

[91] A. Giorgi, S. Migliarini, A. Galbusera, G. Maddaloni, M. Mereu, G. Margiani, M. Gritti, S. Landi, F. Trovato, S. M. Bertozzi, et al., Brain-wide mapping of endogenous serotonergic transmission via chemogenetic fmri, Cell Reports 21 (4) (2017) 910–918.

[92] J. Kong, P.-c. Tu, C. Zyloney, T.-p. Su, Intrinsic functional connectivity of the periaqueductal gray, a resting fmri study, Behavioural brain research 211 (2) (2010) 215–219.

[93] B. J. Hoffman, S. R. Hansson, E. Mezey, M. Palkovits, Localization and dynamic regulation of biogenic amine transporters in the mammalian central nervous system, Frontiers in neuroendocrinology 19 (3) (1998) 187–231.

[94] M. Nørgaard, M. Ganz, C. Svarer, B. Mc Mahon, P. M. Fisher, N. Churchill, V. Beliveau, C. Grady, S. C. Strother, G. M. Knudsen, Brain networks implicated in seasonal affective disorder: A neuroimaging pet study of the serotonin transporter, Frontiers in Neuroscience 11 (2017) 614.

[95] F. Beissner, A. Schumann, F. Brunn, D. Eisenträger, K.-J. Bär, Advances in functional magnetic resonance imaging of the human brainstem, Neuroimage 86 (2014) 91–98.

[96] T. Moher Alsady, E. M. Blessing, F. Beissner, Mica—a toolbox for masked independent component analysis of fmri data, Human brain mapping 37 (10) (2016) 3544–3556.

Appendix

Study I-III

Functional connectivity of the dorsal and median raphe nuclei at rest

Vincent Beliveau[1,2], **Claus Svarer**[1], **Vibe G. Frokjaer**[1], **Gitte M. Knudsen**[1,2], **Douglas N. Greve**[3,4,†], and **Patrick M. Fisher**[1,†,*]

[1]Neurobiology Research Unit and Center for Integrated Molecular Brain Imaging, Rigshospitalet, Copenhagen, Denmark

[2]Faculty of Health and Medical Sciences, University of Copenhagen, Copenhagen, Denmark

[3]Athinoula A. Martinos Center for Biomedical Imaging, Department of Radiology, Massachusetts General Hospital, Boston, MA, USA

[4]Harvard Medical School, Boston, MA, USA

Abstract

Serotonin (5-HT) is a neurotransmitter critically involved in a broad range of brain functions and implicated in the pathophysiology of neuropsychiatric illnesses including major depression, anxiety and sleep disorders. Despite being widely distributed throughout the brain, there is limited knowledge on the contribution of 5-HT to intrinsic brain activity. The dorsal raphe (DR) and median raphe (MR) nuclei are the source of most serotonergic neurons projecting throughout the brain and thus provide a compelling target for a seed-based probe of resting-state activity related to 5-HT. Here we implemented a novel multimodal neuroimaging approach for investigating resting-state functional connectivity (FC) between DR and MR and cortical, subcortical and cerebellar target areas. Using [^{11}C]DASB positron emission tomography (PET) images of the brain serotonin transporter (5-HTT) combined with structural MRI from 49 healthy volunteers, we delineated DR and MR and performed a seed-based resting-state FC analysis. The DR and MR seeds produced largely similar FC maps: significant positive FC with brain regions involved in cognitive and emotion processing including anterior cingulate, amygdala, insula, hippocampus, thalamus, basal ganglia and cerebellum. Significant negative FC was observed within pre- and postcentral gyri for the DR but not for the MR seed. We observed a significant association between DR and MR FC and regional 5-HTT binding. Our results provide evidence for a resting-

Conflict of Interest

state network related to DR and MR and comprising regions receiving serotonergic innervation and centrally involved in 5-HT related behaviors including emotion, cognition and reward processing. These findings provide a novel advance in estimating resting-state FC related to 5-HT signaling, which can benefit our understanding of its role in behavior and neuropsychiatric illnesses.

Keywords

serotonin; resting-state; functional connectivity; dorsal raphe; median raphe

1 Introduction

The serotonin (5-hydroxytryptamine, 5-HT) neurotransmitter system is a critical component in the healthy functioning of the human brain and is involved in many functions such as sleep-wake cycle (Portas et al., 2000), reward (Liu et al., 2014), appetite (Curzon, 1990), emotion (Meneses and Liy-Salmeron, 2012), motor function (Di Matteo et al., 2008) and cognition (Meneses, 1999). Disruptions in the serotonin system have been implicated in a wide spectrum of neuropsychiatric disorders, including major depression disorder (Paul-Savoie et al., 2011), anxiety (Sullivan et al., 2005), bipolar disorder (Mahmood and Silverstone, 2001), chronic stress (Jovanovic et al., 2011), and drug addiction (Müller and Homberg, 2014).

Serotonergic innervation of cerebral cortex, subcortical structures and cerebellum originate for the greater part from the dorsal (DR) and median (MR) raphe nuclei (Dorocic et al., 2014; Hornung, 2003; Jacobs and Azmitia, 1992; Vertes and Linley, 2008). Thus, effects of serotonin signaling on brain function and behavior critically depend on appropriate communication with these nuclei. Despite substantial focus and clear relevance to delineating neurobiological mechanisms associated with various neuropsychiatric illnesses, the effects of serotonin signaling on brain function are not fully understood. Recent studies have reported that serotonin signaling modulates resting-state networks (RSNs) including the commonly studied default mode network (DMN) (Hahn et al., 2012; McCabe and Mishor, 2011). However, these studies have focused on networks modulated by serotonergic input rather than more directly modeling serotonin-related connectivity based on raphe nuclei intrinsic connectivity. The evaluation of the functional connectivity (FC) with DR or MR at rest would provide yet unreported novel insight into how serotonin signaling shapes intrinsic brain connectivity.

The purpose of this study was to elucidate FC of the DR and MR in the healthy human brain at rest. We used high resolution imaging of the serotonin transporter (5-HTT) with [^{11}C]DASB positron emission tomography (PET), an effective probe of 5-HTT binding in receptor-rich regions (Frankle and Slifstein, 2006), combined with anatomical landmarks from structural magnetic resonance imaging (MRI) to determine subject-specific DR and MR regions of interests (ROIs). These ROIs were then transferred to functional MRI (fMRI) space where we performed seed-based FC to identify areas showing significant resting-state FC with DR and MR. Finally we correlated regional DR and MR FC with regional 5-HTT binding to assess the association between the identified FC maps and serotonin signaling.

2 Methods

2.1 Participants

Data from 63 healthy women were collected at baseline as part of a broader randomized, placebo-controlled and double-blind intervention study. Subjects were scanned before (baseline) and after an intervention. In the current study, the baseline data was used for the main analysis and the placebo intervention data was included only for the test-retest evaluation. The placebo intervention consisted of a single subcutaneous injection of saline into the abdomen approximately 4 weeks prior to rescan. Additional details regarding the overall study design can be found elsewhere (Frokjaer et al., under review). Importantly, all fMRI and PET data were acquired at a fixed time relative to their menstrual cycle phase (follicular), as determined by ovarian ultrasound. The study was registered and approved by the local ethics committee under the protocol number H-2-2010-108. After complete description of the study, written informed consent was obtained from all participants.

Of the 63 participants, 14 were excluded due to excessive motion (detailed below in 2.5 fMRI analysis) during the rs-fMRI scans at baseline. Thus rs-fMRI data from 49 participants (age 24.2 ± 4.7) was available for our analyses. To evaluate the reproducibility of the FC results, we repeated the FC analysis on data from the 20 participants that received placebo (age 25.6 ± 6.2) but were without excessive motion at baseline and rescan, using the seeds defined on the baseline PET images. DR and MR delineation was also performed on baseline and rescan PET images for these 20 participants and the overlap was evaluated.

2.2 Data acquisition

2.2.1 Magnetic resonance imaging (MRI)—Participants completed a 10-minute rs-fMRI scan (280 volumes) acquired on a Siemens (Erlangen, Germany) 3T Verio MR scanner. During rs-fMRI scans, participants were instructed to close their eyes, but not to fall asleep. The participants were asked after the scan whether they fell asleep during the scan; all participants reported not falling asleep. Scans were acquired using a T2*-weighted gradient echo-planar imaging (EPI) sequence sensitive to blood-oxygen level dependent (BOLD) signal (TR=2.15 s, TE=26 ms, flip-angle=78°, in-plane matrix 64x64, number of slices=42, voxel size=3x3x3 mm, GRAPPA acceleration factor 2, no gap, interleaved slice order). Pulse and respiratory data were sampled at 50 Hz using the Siemens' Physiological Monitoring Unit.

A high-resolution 3D T1-weighted structural image was acquired using a sagittal, magnetization prepared rapid gradient echo (MP-RAGE) sequence (TE/TR/TI=2.32/1900/900 ms, flip angle=9°, in-plane matrix 256x256, number of slices=224, voxel size=0.9x0.9x0.9 mm, GRAPPA acceleration factor 2, no gap, acquisition time = 8 min 30 sec). A high-resolution 3D T2-weighted image was acquired using a sagittal, Turbo Spin Echo (TSE) scan of the whole head (TE/TR= 409/3200 ms, flip angle=120º, in-plane matrix 256x256, number of slices=176, voxel size=1x1x1 mm, GRAPPA acceleration factor 2, acquisition time = 4 min 43 sec).

2.2.2 [^{11}C] DASB positron emission tomography (PET) imaging—[^{11}C]DASB
PET list-mode data were acquired with a Siemens ECAT HRRT scanner operating in 3D-acquisition mode, with an approximate in-plane resolution of 2 mm. Scan duration was 90 minutes and started immediately after bolus injection of 585 ± 34 MBq [^{11}C]DASB. Thirty-six dynamic PET frames (6x10 sec, 3x20 sec, 6x30 sec, 5x60 sec, 5x120 sec, 8x300 sec, 3x600 sec) were reconstructed using a 3D-OSEM-PSF algorithm (Comtat et al., 2008; Hong et al., 2007; Sureau et al., 2008). Realignment of PET frames was performed using AIR 5.2.5 (Woods et al., 1992) to account for within-scan motion.

5-HTT binding was quantified as [^{11}C]DASB nondisplaceable binding potential (BP$_{ND}$) values determined with the Multilinear Reference Tissue Model 2 (Ichise et al., 2003) as previously described (Frokjaer et al., 2014). The kinetic modeling was performed using Freesurfer (Greve et al., 2013) with cerebellum gray matter segmentation as reference region and a combined thalamus, caudate, putamen and pallidum region as the high binding region for determining k2'. Surface and volume [^{11}C]DASB BP$_{ND}$ maps were smoothed by 10 and 6 mm full width half maximum (FWHM) Gaussian 2D and 3D filters, respectively.

2.3 Anatomical MRI Analysis

Structural images was analyzed in FreeSurfer (FS, surfer.nmr.mgh.harvard.edu, version 5.3) (Dale et al., 1999; Fischl and Dale, 2000; Fischl et al., 1999a, 1999b; Greve and Fischl, 2009; Ségonne et al., 2007, 2004). The T2-weighted structural images were used to refine the delineation of the pial surfaces. This process creates mesh models of the cortical surfaces and labels cortical and subcortical ROIs customized to each subject. Some of these ROIs were used to help create search spaces for the DR and MR. The cortical surfaces were aligned with a cortical surface atlas using nonlinear surface-based registration (Fischl et al., 1999a). This atlas is the surface-based equivalent to Talairach or MNI space and serves as a space in which voxel-wise group analysis can be performed on the surface. The anatomical volume was also registered to the MNI305 atlas which serves as the group analysis space for volume-based analysis of subcortical structures.

2.4 Delineation of DR and MR

Histological studies performed by Baker and colleagues (1991a, 1991b, 1990) have provided in-depth knowledge of the morphology and location of the DR and the MR in the *ex vivo* human brain. However, to perform seed-based FC, accurate *in vivo* segmentation of DR and MR are needed (Kalbitzer and Svarer, 2009). This presents a challenge (Kranz and Hahn, 2012), as the raphe nuclei are composed of sparse neurons surrounded by white matter and they have no well-defined boundaries visible in MRI (Baker et al., 1996, 1991a, 1990).

We have adopted a method similar to (Schain et al., 2013) in which liberal search volumes were defined on the structural MRI and then refined using the PET image. The DR lies on the midline of the brainstem and extends from the oculomotor nucleus to the middle of the pons (Baker et al., 1990). It can be subdivided at the level of the isthmus into two groups, a midbrain (B7) group and a pontine (B6) group (Dahlström and Fuxe, 1964) which meet near the inferior opening of the cerebral aqueduct (CA). The B7 group is adjacent to the CA. The B6 group is only about 0.5 mm in radius, well below current scanner resolution for fMRI.

For this reason, we focused on the B7 group as the seed region for our analysis. The search volume for the DR was defined from the inferior to the superior limit of the CA and from the anterior boundary of the CA to approximately 6mm (5 voxels) anterior to that boundary. Lateral boundaries definitions were not needed for the refinement procedure.

The MR also lies on the midline of the brainstem and extends from the caudal pole of the DR to, approximately, the decussation of the superior cerebellar peduncle (Baker et al., 1991a). Based on this description, the search volume for the MR was defined from the inferior boundary of the CA down, and from the anterior limit of the 4th ventricle to (6 mm) 5 voxels anterior to that limit. Neither inferior nor lateral limits were needed for the refinement procedure.

The DR and MR search spaces were refined using a mean [^{11}C]DASB image created by integrating the number of counts over time of the PET frames. The mean PET image was smoothed using a 3-voxel median filter to reduce spatial noise while preserving border (edge) integrity (Chin and Yeh, 1983) between the raphe and ventricular space. For delineation of the DR and MR, we used the mean uptake instead of the BP_{ND} because the kinetic modeling is noisy and requires spatial smoothing, which could introduce spatial uncertainty due to the proximity of low count regions such as the CA and 4th ventricle. The mean uptake image of a subject was registered to the gradient distortion (GD) corrected structural MRI using boundary-based registration (BBR) which has been shown to be a highly robust and accurate cross-modal registration technique (Greve and Fischl, 2009). GD correction was performed as described in Jovicich et al. (2006). This allowed for anatomical landmarks be transferred onto the PET image and to subsequently transfer back the seed region onto the structural MRI.

The refinement procedure was iterative. The first voxel of the ROI was defined by the highest PET value within the search volume. Subsequent voxels were added iteratively by selecting the voxel with the highest value within the neighborhood of the already-defined ROI until a target total volume was reached. The total volume of serotonergic neurons in the DR has been estimated to be 71.3±4.5 mm^3 (Baker et al., 1990). However, Schain et al. (2013) suggested to use a volume estimate of 150 mm^3, as the DR is composed of both grey and white matter. Based on the fact that the DR, excluding the caudal subnucleus, is about 57 mm^3, we used a target volume of 115 mm^3. The target volume used for the MR was 64 mm^3, as suggested by Kranz & Hahn (2012). This procedure was applied to enforce local convergence; more lenient clustering methods, such as taking the maximum voxels within the search volume, led to structurally inhomogeneous ROIs, inconsistent with the morphology of the DR and MR. Once the iterative process completed, the seed was transferred onto the GD corrected structural MRI and an inverse gradient unwarping (i.e., reintroduction of gradient non-linearities) was applied to the ROIs to match gradient non-linearities present in the BOLD fMRI images.

2.5 fMRI analysis

The resting-state fMRI volumes were motion corrected using AFNI's *3dVolReg* (Cox and Hyde, 1997; Cox, 1996). Physiological noise was removed in a two-step procedure. First the raw time series was corrected for physiological noise using *PESTICA v2* (Beall and Lowe,

2007; Beall, 2010) in conjunction with the respective cardiac and respiratory recordings. The second step, described more below, involved including nuisance regressors in the time series analysis. Spatial distortion caused by inhomogeneity of the B_0 magnetic field was removed (Jezzard and Balaban, 1995). The DR, MR and aCompCor time series were then extracted from these data, prior to further processing (e.g. spatial filtering). Extracting the time series prior to spatial smoothing assures that signal outside of the target region does not corrupt the waveform.

The fMRI analysis was performed in the FreeSurfer Functional Analysis Stream (FSFAST, surfer.nmr.mgh.harvard.edu/fswiki/FsFast). The fMRI was registered to the structural MRI using BBR. In FSFAST, the time series analysis is separated into cortical and subcortical streams. In the cortical stream, the fMRI time series was sampled onto the left and right cortical surfaces and smoothed (Hagler Jr. et al., 2006) with a 10mm FWHM Gaussian filter. Smoothing on the surface reduces the blurring of white matter, cerebrospinal fluid, and subcortical gray matter with cortical gray matter as well as blurring across adjacent gyri. The surface time series data were then sampled into the group space of surface atlas. The subcortical structures were sampled into MNI305 space and volume smoothed with a 6mm FWHM Gaussian filter.

A general linear model (GLM) used to fit the time series data consisted of the DR or MR time series as well as several nuisance regressors. A high-pass filter (cutoff 0.01 Hz) was implemented by including polynomial regressors up to order 17. Noise of non-neuronal origin was estimated using aCompCor (Behzadi et al., 2007). As suggested by Chai et al. (2012), a mask was constructed combining white matter and ventricular and sulcal cerebrospinal fluid as defined for each subject from the FreeSurfer anatomical analysis; the mask was eroded by 1 anatomical voxel. The first 5 principal components of the BOLD time series from this mask were used as nuisance regressors. The six motion estimates were also used as nuisance regressors. The Euclidean norm of the first difference of the motion estimates, $\|d\|_2$, was computed (Jo et al., 2013). Frames containing excessive motion, based on the criterion $\|d\|_2 > 0.2$, were censored. A given frame at time t was censored by adding to the GLM a regressor where all values were 0 except at time t where the value was 1. For a given censored frame at time t, additional censoring regressors were also created for the previous frame (t-1) and the two subsequent frames (t+1) and (t+2). A subject's data was excluded if more than 10% (28 frames) of the resting-state data were censored. The DR and MR were analyzed using different GLMs.

Group analysis was performed using a voxel-wise two-tailed t-test to determine the areas where the group means of the DR or MR regression coefficient was significantly different than zero. Correction for multiple comparisons was performed using a cluster-wise correction (Friston et al., 1994; Hagler Jr. et al., 2006). Clusters were defined using a voxel-wise threshold of $p < 0.001$. Clusters with cluster-wise $p < 0.05$ were deemed significant.

2.6 Association between FC and 5-HTT binding

The association between FC and 5-HTT binding was evaluated using a linear regression analysis. For every subject, we computed the mean [11C]DASB BP$_{ND}$ and mean FC for the 42 cortical and subcortical brain regions defined by FreeSurfer as containing gray matter

(left and right hemispheres were averaged together) and we computed the within-subject slope for $[^{11}C]$DASB BP_{ND} against FC. We then performed a two-tailed t-test to determine whether the distribution of slopes across subjects was different than 0.

3 Results

3.1 DR and MR seeds

An example of DR and MR segmentation is shown in Figure 1. The average centroid of the DR was (0, −31 −9) in MNI305 space; that of the MR was (0,−35,−21). Although the volume of the seeds defined on the PET images was constant, the reintroduction of GD slightly affected the final volume of the seeds from subject to subject; the volume (mean ± std) was 118±11mm^3 for DR and 65±8mm^3 for MR. For the same reason, the number of functional voxels was 18±3 for DR and 11±2 for MR. The median correlation between the DR and MR raw time-series was 0.26 (range −0.24 − 0.62).

3.2 FC of the DR and MR and its association with 5-HTT binding

The group-level FC maps revealed that the DR seed was functionally connected with multiple cortical and subcortical regions (Figure 2; Table 1). For the cortical surface, we observed significant bilateral positive FC within the parahippocampal gyrus, insula and rostral anterior cingulate (rACC). Clusters showing significant negative FC were observed bilaterally within somatosensory areas including paracentral lobule and the pre- and postcentral gyrus and minor negative clusters were observed in superior parietal lobule and superior frontal gyrus. For subcortical regions, we observed a large cluster centered on the seed in brainstem showing statistically significant positive FC. This cluster extended outside brainstem to include regions of the basal ganglia (putamen, caudate, pallidum, accumbens), limbic structures (hippocampus and amygdala), thalamus, cerebellum and ventral diencephalon.

Group-level FC results for MR were largely similar to DR results (Figure 3; Table 2). On the cortical surface, we observed significant bilateral positive FC within the parahippocampal gyrus, insula and rACC. Subcortically, we observed a cluster centered on the seed and extending outside brainstem and including putamen, caudate, pallidum, hippocampus and amygdala, thalamus, cerebellum, ventral diencephalon and accumbens area.

A prominent difference between the DR and MR FC maps was significant negative FC for the DR but not the MR. FC for both seeds had some overlap but also covered distinct and separate areas (Figure 4). A subject-wise paired t-test between DR and MR FC results showed a significant difference (voxel threshold p=0.001 and cluster threshold p=0.05) only within the postcentral and superior frontal gyri and brainstem; as the seed was located in brainstem the latter difference will not be addressed further.

Since serotonergic neurons (and axons) are abundant in 5-HTT and it has been shown that co-localization between 5-HT and 5-HTT positive fibers is close to 100% (Nielsen et al., 2006) we evaluated if DR or MR FC was correlated with 5-HTT binding at a regional level. For both seeds we observed a significant positive association between $[^{11}C]$DASB BP_{ND} and FC (p <0.0001) (Figure 5).

3.3 Test-retest evaluation of the FC maps and raphe delineation

Test-retest differences were evaluated by comparing baseline and rescan data for 20 participants who received a placebo and whose rs-fMRI data did not contain excessive motion on both baseline and rescan. First, new DR and MR seeds were generated on the baseline structural MRI with the rescan PET images. The median overlap was 31% (range 15%–42%) for DR and 37% (range 24%–53%) for MR and the median volume difference was 13 mm^3 (range 3 – 27 mm^3) for DR and 11 mm^3 (range 1 – 30 mm^3) for MR; see Supplementary Figure 1 for an example of DR and MR delineation at baseline and rescan. Next, new FC maps were generated for both the baseline and rescan fMRI using the baseline seed definitions (Supplementary Figure 2–3). The clusters looked similar but more spatially constrained and with a lower statistical significance due to the reduced sample size (only 20 subjects versus 49). The group-level results of the paired difference between the FC maps at baseline and rescan showed no statistically significant clusters. Finally, new FC maps were generated from the rescan fMRI using the rescan seed definitions (Supplementary Figure 2– 3). Again, the maps looked similar to when the baseline seeds were used and no statistically significant difference was observed between the two maps.

4 Discussion

Here we sought to investigate serotonin-related FC using a multimodal neuroimaging approach for delineation of the DR and MR within a cohort of 49 healthy women. We identified brain regions significantly functionally connected with both nuclei and observed a statistically significant association between raphe FC and 5-HTT binding suggesting a compelling serotonergic component to the intrinsic brain activity related to the raphe nuclei.

We observed significant and distributed FC between both raphe seeds and medial prefrontal cortex (mPFC) and anterior cingulate cortex (ACC). Structural evidence supports the presence of direct reciprocal projections between mPFC and raphe (Behzadi et al., 1990; Peyron et al., 1998; Vertes and Linley, 2008; Vertes, 1991) and direct stimulation of mPFC has been shown to modulate raphe 5-HT neuron activity (Hajós et al., 1998). Electrophysiological evidence from rodents indicates that mPFC-raphe feedback is modulated via serotonin 1A, 2A and 4 receptor signaling (Celada et al., 2001; Lucas et al., 2005; Riad et al., 1999; Sharp et al., 2007) and that stimulation of mPFC axons in the DR induces a rapid antidepressant-like behavioral effect (Warden et al., 2012). Furthermore, two human neuroimaging studies from our lab have also demonstrated an association between mPFC 5-HTT binding and cortisol awakening response, a putative marker of stress responsiveness (Frokjaer et al., 2014, 2013). From a clinical perspective, the prominent raphe-mPFC FC that we observed is also particularly interesting considering converging evidence that mPFC dysfunction is linked to a myriad of neuropsychiatric illnesses including depression and may affect treatment response (Mayberg et al., 2005; Pizzagalli, 2011). Although rs-fMRI does not allow us to disentangle directionality (i.e., raphe to mPFC signaling or vice versa), our findings of significant connectivity between these regions supports this as an informative approach for delineating serotonin-related raphe-mPFC circuit function. Future studies employing this approach would benefit our understanding of its relevance in predicting prefrontal-mediated behaviors or neuropsychiatric illnesses.

A prominent feature of our results is the large overlapping subcortical clusters of positive FC common to both raphe seeds (see Figure 4). The observation of a singular subcortical cluster is somewhat uninformative about region-specific FC. Thus, we evaluated FC maps at more conservative voxel-level thresholds of $p<10^{-3}$, 10^{-5} and 10^{-7}. Even at these thresholds, subclusters did not emerge. We think it is unlikely that this one large cluster is simply an artifact reflecting the combination of 6mm spatial smoothing and the raphe seed correlating with itself. Although the cluster peak is located in the raphe seed, other activated structures are far away. For example, thalamus is approximately 25mm away and basal ganglia and hippocampus are more than 30mm away. These distances are more than 10 standard deviations of the 6mm FWHM kernel away from the raphe seed, so FC is unlikely to be simple spill-over from raphe. Our observation that regional FC and 5-HTT are positively correlated and that many of these subcortical regions have high 5-HTT binding suggests that the presence of a single large subcortical cluster may reflect, in part, serotonergic effects on FC. Further evaluation of raphe connectivity with recently described methods that may limit smoothing effects may prove effective in delineating discrete clusters (Beissner et al., 2014). However, similar subcortical RSNs have previously been identified in a number of studies and have been referred to as a limbic or basal ganglia RSN (Damoiseaux and Beckmann, 2008; Janes et al., 2012; Kim et al., 2013; Martino and Scheres, 2008; Moussa et al., 2012; Robinson et al., 2009, 2008; Schöpf and Kasess, 2010; Smith et al., 2009). However, their functional relevance was in many cases not considered. Our results suggest that this subcortical RSN is related to intrinsic raphe activity and may be associated with the 5-HT system. Although some studies reporting similar FC maps using seed-based analysis (Kong et al., 2010; Martino and Scheres, 2008), most studies used ICA methods, which decompose the rs-fMRI signal into a predefined number of components. However, many independent components are required when using ICA methods to isolate the subcortical RSN (e.g. Janes et al. (2012) used 35 components), which can segregate salient networks such as the DMN into multiple components. Particular care is needed when using ICA to identify subcortical RSNs and in the context of studying serotonergic features, such as a relation with mPFC, a hypothesis-driven approach such as our seed-based method might be advantageous to a purely data-driven method like ICA.

Converging evidence supports an association between structural and functional connectivity at rest within the human brain (Hermundstad et al., 2013; Heuvel and Mandl, 2009). Although efferent and afferent raphe projections have been studied extensively, the bulk of this work was performed in animal models and caution needs to be taken when interpreting human data in light of these studies. Nonetheless, the observed raphe FC maps appears to be generally consistent with the overall known DR and MR projections, although discrepancies can be found (see Vertes and Linley (2008) for an extensive review of the raphe projections). It is interesting to note that although DR and MR have efferent projections to distinct brain areas (Vertes and Linley, 2007; Vertes, 2004), they mostly share afferent projections from common brain areas and there is extensive innervation between the nuclei (Vertes and Linley, 2008). These features could explain the striking similarity between the two FC maps. However, one of the most noticeable differences between the FC maps is the presence of significant negative FC within postcentral and superior frontal gyri for the DR but not for MR. Interestingly, DR has been shown to modulate a nociceptive pathway

including somatosensory cortex (Prieto-Gómez et al., 1989; Reyes-Vazquez et al., 1989; Wang and Nakai, 1994), which may underlie the observed FC with this region. Alternatively, our seed may capture signal from the neighboring periacqueductal gray, a region also involved in nociception (Kong et al., 2010; Linnman et al., 2012). The spatial resolution of our functional images makes it difficult to spatially disentangle these regions. Thus, future higher-resolution studies (e.g., at 7T) would help resolve this overlap. Nonetheless, given the association we have identified between raphe FC and 5-HTT binding and the striking similarity between MR, distinct from periacqueductal gray, and DR FC maps, our method may provide a novel method for probing the association between nociception and the 5-HT system.

5 Limitations and technical concerns

We attempted to effectively account for inherent challenges when estimating raphe FC, however our study is not without limitations. Our target regions and the resulting ROIs are very small, which makes them susceptible to motion and being in brainstem makes them sensitive to physiological noise (Brooks and Faull, 2013). Although these issues are a concern, we have taken steps to minimize these effects including strict exclusion criteria based on motion estimates and implementation of current tools for correction of physiological noise. However, it is plausible that physiological noise not well captured by these methods represents a potential confound. Furthermore, our test-retest evaluation showed no significant group-level differences. Recent work using ICA has shown that it might be possible to identify brainstem nuclei using conventional fMRI, which might provide an alternative method to our approach (Beissner et al., 2014), however the physiological validity of this technique still needs to be proved. A recent study has demonstrated that subjects may drift between wakefulness and sleep during rs-fMRI (Tagliazucchi and Laufs, 2014). As the 5-HT system is linked to wakefulness (Portas et al., 2000; Shima et al., 1986) this is a potentially important source of variation. Although subjects indicated that they did not sleep during the resting-state scan session, robust monitoring of the awake state could be secured in future studies using MRI-compatible EEG. Given that our dataset comprised only women, future studies in males would inform whether our observed FC maps are sex-specific. Finally, although we feel that the nature of the placebo intervention is unlikely to have perturbed serotonin signaling or rs-fMRI connectivity, we cannot rule this out as a potential source of additional variability affecting the test-retest of our data.

DR and MR notably also include non-serotonergic neurons, which may limit the extent to which these maps capture features specific for 5-HT signaling. Approximately half of the neurons within DR and MR are serotonergic (Jacobs and Azmitia, 1992; Steinbusch et al., 1980; Wiklund et al., 1981) and the 5-HT and non-5-HT containing neurons have distinct electrophysiological properties (Beck and Pan, 2004; Hornung, 2003; Kirby et al., 2003; Michelsen et al., 2007), thereby limiting the extent to which these maps may reflect effects of 5-HT, specifically. Future studies directly manipulating 5-HT (e.g., using a pharmacological challenge such as tryptophan depletion or 5-HTT inhibition) could be an effective probe for evaluating aspects of the serotonergic contribution to raphe FC.

6 Conclusion

We have demonstrated a biologically driven method for accurate delineation of the DR and MR ROIs in neuroimaging studies. We then performed a seed-based analysis and identified FC related to these nuclei. The FC map were very similar for both seeds; positive FC was found with cortical regions such as rACC, insula, parahippocampal gyrus and subcortical regions such as basal ganglia, thalamus, hippocampus, amygdala and cerebellum. We found a positive association between raphe FC and 5-HTT binding supporting a serotonergic contribution to the observed resting-state signal. Our results suggest that raphe FC is related to the previously identified subcortical RSN. Further investigation of this network might prove similarly useful for studying 5-HT related brain disorders.

Supplementary Material

Refer to Web version on PubMed Central for supplementary material.

Acknowledgments

References

Baker K, Halliday G, Halasz P. Cytoarchitecture of serotonin- synthesizing neurons in the pontine tegmentum of the human brain. Synapse. 1991a; 7:301–320. [PubMed: 2042112]

Baker K, Halliday G, Hornung J. Distribution, morphology and number of monoamine-synthesizing and substance P-containing neurons in the human dorsal raphe nucleus. Neuroscience. 1991b; 42:757–775. [PubMed: 1720227]

Baker K, Halliday G, Kril J, Harper C. Chronic alcoholism in the absence of Wernicke-Korsakoff syndrome and cirrhosis does not result in the loss of serotonergic neurons from the median raphe nucleus. Metab Brain Dis. 1996; 11:217–227. [PubMed: 8869942]

Baker K, Halliday G, Törk I. Cytoarchitecture of the human dorsal raphe nucleus. J Comp Neurol. 1990; 161:147–161. [PubMed: 2262589]

Beall E. Adaptive cyclic physiologic noise modeling and correction in functional MRI. J Neurosci Methods. 2010; 187:216–228. [PubMed: 20096307]

Beall E, Lowe M. Isolating physiologic noise sources with independently determined spatial measures. Neuroimage. 2007; 37:1286–1300. [PubMed: 17689982]

Beck S, Pan Y. Median and dorsal raphe neurons are not electrophysiologically identical. J Neurophysiol. 2004; 91:994–1005. [PubMed: 14573555]

Behzadi G, Kalén P, Parvopassu F, Wiklund L. Afferents to the median raphe nucleus of the rat: retrograde cholera toxin and wheat germ conjugated horseradish peroxidase tracing, and selective D-[3H]aspartate labelling of possible excitatory amino acid inputs. Neuroscience. 1990; 37:77–100. [PubMed: 2243599]

Behzadi Y, Restom K, Liau J, Liu T. A component based noise correction method (CompCor) for BOLD and perfusion based fMRI. Neuroimage. 2007; 37:90–101. [PubMed: 17560126]

Beissner F, Schumann A, Brunn F, Eisenträger D, Bär KJ. Advances in functional magnetic resonance imaging of the human brainstem. Neuroimage. 2014; 86:91–98. [PubMed: 23933038]

Brooks J, Faull O. Physiological noise in brainstem fMRI. Front Hum Neurosci. 2013:1–13. [PubMed: 23355817]

Celada P, Puig MV, Casanovas JM, Guillazo G, Artigas F. Control of dorsal raphe serotonergic neurons by the medial prefrontal cortex: Involvement of serotonin-1A, GABA(A), and glutamate receptors. J Neurosci. 2001; 21:9917–9929. [PubMed: 11739599]

Chai X, Castañón A, Öngür D, Whitfield-Gabrieli S. Anticorrelations in resting state networks without global signal regression. Neuroimage. 2012; 59:1420–1428. [PubMed: 21889994]

Chin R, Yeh C. Quantitative evaluation of some edge-preserving noise-smoothing techniques. Comput Vision, Graph Image Process. 1983; 23:67–91.

Comtat, C.; Sureau, FC.; Sibomana, M.; Hong, IK.; Sjoholm, N.; Trebossen, R. Image based resolution modeling for the HRRT OSEM reconstructions software. 2008 IEEE Nuclear Science Symposium Conference Record; IEEE; 2008. p. 4120-4123.

Cox RW. AFNI: software for analysis and visualization of functional magnetic resonance neuroimages. Comput Biomed Res. 1996; 29:162–173. [PubMed: 8812068]

Cox RW, Hyde JS. Software tools for analysis and visualization of fMRI data. NMR Biomed. 1997; 10:171–178. [PubMed: 9430344]

Curzon G. Serotonin and appetite. Ann N Y Acad Sci. 1990; 600:521–530. [PubMed: 2252331]

Dahlström A, Fuxe K. Evidence for the existence of monoamine-containing neurons in the central nervous system. I Demonstration of monoamines in the cell bodies of brain stem neurons. Acta Physiol Scand Suppl. 1964; 232:1–55.

Dale A, Fischl B, Sereno M. Cortical surface-based analysis: I. Segmentation and surface reconstruction. Neuroimage. 1999; 194:179–194. [PubMed: 9931268]

Damoiseaux J, Beckmann C. Reduced resting-state brain activity in the —default network in normal aging. Cereb Cortex. 2008; 18:1856–1864. [PubMed: 18063564]

Di Matteo V, Pierucci M, Esposito E, Crescimanno G, Benigno A, Di Giovanni G. Serotonin modulation of the basal ganglia circuitry: therapeutic implication for Parkinson's disease and other motor disorders. Prog Brain Res. 2008; 172:423–463. [PubMed: 18772045]

Dorocic IP, Fürth D, Xuan Y, Johansson Y, Pozzi L, Silberberg G, Carlén M, Meletis K. A Whole-Brain Atlas of Inputs to Serotonergic Neurons of the Dorsal and Median Raphe Nuclei. Neuron. 2014; 83:663–678. [PubMed: 25102561]

Fischl B, Dale AM. Measuring the thickness of the human cerebral cortex from magnetic resonance images. Proc Natl Acad Sci U S A. 2000; 97:11050–11055. [PubMed: 10984517]

Fischl B, Sereno M, Tootell R, Dale A. High-resolution intersubject averaging and a coordinate system for the cortical surface. Hum Brain Mapp. 1999a; 8:272–284. [PubMed: 10619420]

Fischl B, Sereno MI, Dale AM. Cortical surface-based analysis. II: Inflation, flattening, and a surface-based coordinate system. Neuroimage. 1999b; 9:195–207. [PubMed: 9931269]

Frankle W, Slifstein M. Estimation of serotonin transporter parameters with 11C-DASB in healthy humans: reproducibility and comparison of methods. J Nucl Med. 2006:815–826. [PubMed: 16644752]

Friston KJ, Worsley KJ, Frackowiak RS, Mazziotta JC, Evans aC. Assessing the significance of focal activations using their spatial extent. Hum Brain Mapp. 1994; 1:210–220. [PubMed: 24578041]

Frokjaer VG, Erritzoe D, Holst KK, Jensen PS, Rasmussen PM, Fisher PM, Baaré W, Madsen KS, Madsen J, Svarer C, Knudsen GM. Prefrontal serotonin transporter availability is positively associated with the cortisol awakening response. Eur Neuropsychopharmacol. 2013; 23:285–294. [PubMed: 22732516]

Frokjaer VG, Erritzoe D, Holst KK, Madsen KS, Fisher PM, Madsen J, Svarer C, Knudsen GM. In abstinent MDMA users the cortisol awakening response is off-set but associated with prefrontal serotonin transporter binding as in non-users. Int J Neuropsychopharmacol. 2014; 17:1119–1128. [PubMed: 24524290]

Frokjaer, VG.; Pinborg, A.; Holst, KK.; Overgaard, A.; Henningsson, S.; Heede, M.; Larsen, EC.; Jensen, PS.; Agn, M.; Nielsen, AP.; Stenbæk, DS.; da Cunha-Bang, S.; Lehel, S.; Siebner, HR.; Mikkelsen, JD.; Svarer, C.; Knudsen, GM. Role of serotonin transporter changes in depressive responses to sex-steroid hormone manipulation: A PET study. Under review

Greve D, Fischl B. Accurate and robust brain image alignment using boundary-based registration. Neuroimage. 2009; 48:63–72. [PubMed: 19573611]

Greve D, Svarer C, Fisher P, Feng L. Cortical surface-based analysis reduces bias and variance in kinetic modeling of brain PET data. Neuroimage. 2013; 92C:225–236. [PubMed: 24361666]

Hagler D Jr, Saygin A, Sereno M. Smoothing and cluster thresholding for cortical surface-based group analysis of fMRI data. Neuroimage. 2006; 33:1093–1103. [PubMed: 17011792]

Hahn A, Wadsak W, Windischberger C, Baldinger P, Hoflich AS, Losak J, Nics L, Philippe C, Kranz GS, Kraus C, Mitterhauser M, Georgios K, Kasper S, Lanzenberger R. Differential modulation of the default mode network via serotonin-1A receptors. Proc Natl Acad Sci. 2012; 109:2619–2624. [PubMed: 22308408]

Hajós M, Richards C, Székely A, Sharp T. An electrophysiological and neuroanatomical study of the medial prefrontal cortical projection to the midbrain raphe nuclei in the rat. Neuroscience. 1998; 87:95–108. [PubMed: 9722144]

Hermundstad AM, Bassett DS, Brown KS, Aminoff EM, Clewett D, Freeman S, Frithsen A, Johnson A, Tipper CM, Miller MB, Grafton ST, Carlson JM. Structural foundations of resting-state and task-based functional connectivity in the human brain. Proc Natl Acad Sci U S A. 2013; 110:6169–6174. [PubMed: 23530246]

van den Heuvel M, Mandl R. Functionally linked resting-state networks reflect the underlying structural connectivity architecture of the human brain. Hum Brain Mapp. 2009; 3141:3127–3141. [PubMed: 19235882]

Hong IK, Chung ST, Kim HK, Kim YB, Son YD, Cho ZH. Ultra Fast Symmetry and SIMD-Based Projection-Backprojection (SSP) Algorithm for 3-D PET Image Reconstruction. IEEE Trans Med Imaging. 2007; 26:789–803. [PubMed: 17679330]

Hornung J. The human raphe nuclei and the serotonergic system. J Chem Neuroanat. 2003; 26:331–343. [PubMed: 14729135]

Ichise M, Liow J, Lu J, Takano A. Reference Tissue Parametric Imaging Methods: Application to [11C] DASB Positron Emission Tomography Studies of the Serotonin Transporter in. J Cereb blood flow Metab. 2003; 23:1096–1112. [PubMed: 12973026]

Jacobs B, Azmitia E. Structure and function of the brain serotonin system. Physiol Rev. 1992; 72:165–229. [PubMed: 1731370]

Janes A, Nickerson L, de Blaise FB, Kaufman M. Prefrontal and limbic resting state brain network functional connectivity differs between nicotine-dependent smokers and non-smoking controls. Drug Alcohol Depend. 2012; 125:252–259. [PubMed: 22459914]

Jezzard P, Balaban R. Correction for geometric distortion in echo planar images from B0 field variations. Magn Reson Med. 1995; 34:65–73. [PubMed: 7674900]

Jo H, Gotts S, Reynolds R. Effective preprocessing procedures virtually eliminate distance-dependent motion artifacts in resting state FMRI. J Appl Math. 2013; 2013

Jovanovic H, Perski A, Berglund H, Savic I. Chronic stress is linked to 5-HT(1A) receptor changes and functional disintegration of the limbic networks. Neuroimage. 2011; 55:1178–1188. [PubMed: 21211567]

Jovicich J, Czanner S, Greve D, Haley E, van der Kouwe A, Gollub R, Kennedy D, Schmitt F, Brown G, Macfall J, Fischl B, Dale A. Reliability in multi-site structural MRI studies: effects of gradient non-linearity correction on phantom and human data. Neuroimage. 2006; 30:436–443. [PubMed: 16300968]

Kalbitzer J, Svarer C. A probabilistic approach to delineating functional brain regions. J Nucl Med Technol. 2009; 37:91–95. [PubMed: 19447857]

Kim D, Park B, Park H. Functional connectivity-based identification of subdivisions of the basal ganglia and thalamus using multilevel independent component analysis of resting state fMRI. Hum Brain Mapp. 2013; 34:1371–1385. [PubMed: 22331611]

Kirby L, Pernar L, Valentino R, Beck S. Distinguishing characteristics of serotonin and non-serotonin-containing cells in the dorsal raphe nucleus: electrophysiological and immunohistochemical. Neuroscience. 2003; 116:669–683. [PubMed: 12573710]

Kong J, Tu P, Zyloney C, Su T. Intrinsic functional connectivity of the periaqueductal gray, a resting fMRI study. Behav Brain Res. 2010; 211:215–219. [PubMed: 20347878]

Kranz G, Hahn A. Challenges in the differentiation of midbrain raphe nuclei in neuroimaging research. Proc Natl Acad Sci. 2012; 109:E2000. [PubMed: 22711836]

Linnman C, Moulton Ea, Barmettler G, Becerra L, Borsook D. Neuroimaging of the periaqueductal gray: state of the field. Neuroimage. 2012; 60:505–522. [PubMed: 22197740]

Liu Z, Zhou J, Li Y, Hu F, Lu Y, Ma M, Feng Q, Zhang JE, Wang D, Zeng J, Bao J, Kim JY, Chen ZF, El Mestikawy S, Luo M. Dorsal raphe neurons signal reward through 5-HT and glutamate. Neuron. 2014; 81:1360–1374. [PubMed: 24656254]

Lucas G, Compan V, Charnay Y, Neve RL, Nestler EJ, Bockaert J, Barrot M, Debonnel G. Frontocortical 5-HT4 receptors exert positive feedback on serotonergic activity: viral transfections, subacute and chronic treatments with 5-HT4 agonists. Biol Psychiatry. 2005; 57:918–925. [PubMed: 15820713]

Mahmood T, Silverstone T. Serotonin and bipolar disorder. J Affect Disord. 2001

Di Martino A, Scheres A. Functional connectivity of human striatum: a resting state FMRI study. Cereb Cortex. 2008; 18:2735–2747. [PubMed: 18400794]

Mayberg HS, Lozano AM, Voon V, McNeely HE, Seminowicz D, Hamani C, Schwalb JM, Kennedy SH. Deep brain stimulation for treatment-resistant depression. Neuron. 2005; 45:651–660. [PubMed: 15748841]

McCabe C, Mishor Z. Antidepressant medications reduce subcortical–cortical resting-state functional connectivity in healthy volunteers. Neuroimage. 2011; 57:1317–1323. [PubMed: 21640839]

Meneses A. 5-HT system and cognition. Neurosci Biobehav Rev. 1999; 23:1111–1125. [PubMed: 10643820]

Meneses A, Liy-Salmeron G. Serotonin and emotion, learning and memory. Rev Neurosci. 2012; 23:543–553. [PubMed: 23104855]

Michelsen K, Schmitz C, Steinbusch H. The dorsal raphe nucleus—from silver stainings to a role in depression. Brain Res Rev. 2007; 55:329–342. [PubMed: 17316819]

Moussa M, Steen M, Laurienti P, Hayasaka S. Consistency of network modules in resting-state FMRI connectome data. PLoS One. 2012; 7:e44428. [PubMed: 22952978]

Müller CP, Homberg JR. The role of serotonin in drug use and addiction. Behav Brain Res. 2014:1–47.

Nielsen K, Brask D, Knudsen GM, Aznar S. Immunodetection of the serotonin transporter protein is a more valid marker for serotonergic fibers than serotonin. Synapse. 2006; 59:270–6. [PubMed: 16408260]

Paul-Savoie E, Potvin S, Daigle K, Normand E, Corbin JF, Gagnon R, Marchand S. A deficit in peripheral serotonin levels in major depressive disorder but not in chronic widespread pain. Clin J Pain. 2011; 27:529–534. [PubMed: 21415718]

Peyron C, Petit JM, Rampon C, Jouvet M, Luppi PH. Forebrain afferents to the rat dorsal raphe nucleus demonstrated by retrograde and anterograde tracing methods. Neuroscience. 1998; 82:443–468. [PubMed: 9466453]

Pizzagalli, Da. Frontocingulate dysfunction in depression: toward biomarkers of treatment response. Neuropsychopharmacology. 2011; 36:183–206. [PubMed: 20861828]

Portas CM, Bjorvatn B, Ursin R. Serotonin and the sleep/wake cycle : special emphasis on microdialysis studies. Prog Neurobiol. 2000; 60:12–35.

Prieto-Gómez B, Dafny N, Reyes-Vázquez C. Dorsal raphe stimulation, 5-HT and morphine microiontophoresis effects on noxious and nonnoxious identified neurons in the medial thalamus of the rat. Brain Res Bull. 1989; 22:937–943. [PubMed: 2790499]

Reyes-Vazquez C, Qiao JT, Dafny N. Nociceptive responses in nucleus parafascicularis thalami are modulated by dorsal raphe stimulation and microiontophoretic application of morphine and serotonin. Brain Res Bull. 1989; 23:405–411. [PubMed: 2611684]

Riad M, Wu C, Cornea-he V, Singh SK, Descarries L. Cellular and Subcellular Distribution of the Serotonin 5-HT2A Receptor in the Central Nervous System of Adult Rat. J Comp Neurol. 1999; 409:187–209. [PubMed: 10379914]

Robinson S, Basso G, Soldati N. A resting state network in the motor control circuit of the basal ganglia. BMC Neurosci. 2009; 10:1–14. [PubMed: 19126204]

Robinson, S.; Soldati, N.; Basso, G. A resting state network in the basal ganglia. Proc. Int. Soc. Magn. Reseonance Med; Toronto. 2008. p. 746

Schain M, Tóth M, Cselényi Z. Improved mapping and quantification of serotonin transporter availability in the human brainstem with the HRRT. Eur J Med Mol Imaging. 2013; 40:228–237.

Schöpf V, Kasess C. Fully exploratory network ICA (FENICA) on resting-state fMRI data. J Neurosci Methods. 2010; 192:207–213. [PubMed: 20688104]

Ségonne F, Dale AM, Busa E, Glessner M, Salat D, Hahn HK, Fischl B. A hybrid approach to the skull stripping problem in MRI. Neuroimage. 2004; 22:1060–1075. [PubMed: 15219578]

Ségonne F, Pacheco J, Fischl B. Geometrically accurate topology-correction of cortical surfaces using nonseparating loops. IEEE Trans Med Imaging. 2007; 26:518–529. [PubMed: 17427739]

Sharp T, Boothman L, Raley J, Quérée P. Important messages in the —post : recent discoveries in 5-HT neurone feedback control. Trends Pharmacol Sci. 2007; 28:629–636. [PubMed: 17996955]

Shima K, Nakahama H, Yamamoto M. Firing Properties of Two Types of Nucleus Raphe Dorsalis Neurons during the Sleep-Waking Cycle and Their Responses to Sensory Stimuli Recording procedures Fourteen adult cats were anesthetized with Nem- Data analysis was done for 3 behavioral states. 1986; 399:317–326.

Smith SM, Fox PT, Miller KL, Glahn DC, Fox PM, Mackay CE, Filippini N, Watkins KE, Toro R, Laird AR, Beckmann CF. Correspondence of the brain's functional architecture during activation and rest. Proc Natl Acad Sci U S A. 2009; 106:13040–13045. [PubMed: 19620724]

Steinbusch HWM, Van der Kooy D, Verhofstad AAJ, Pellegrino A. Serotonergic and non-serotonergic projections from the nucleus raphe dorsalis to the caudate-putamen complex in the rat, studied by a combined immunofluorescence and fluorescent retrograde axonal labeling technique. Neurosci Lett. 1980; 19:137–142. [PubMed: 6302595]

Sullivan GM, Oquendo Ma, Simpson N, Van Heertum RL, Mann JJ, Parsey RV. Brain serotonin1A receptor binding in major depression is related to psychic and somatic anxiety. Biol Psychiatry. 2005; 58:947–954. [PubMed: 16039621]

Sureau FC, Reader AJ, Comtat C, Leroy C, Ribeiro MJ, Buvat I, Trébossen R. Impact of image-space resolution modeling for studies with the high-resolution research tomograph. J Nucl Med. 2008; 49:1000–1008. [PubMed: 18511844]

Tagliazucchi E, Laufs H. Decoding wakefulness levels from typical fMRI resting-state data reveals reliable drifts between wakefulness and sleep. Neuron. 2014; 82:695–708. [PubMed: 24811386]

Vertes R, Linley S. Comparison of projections of the dorsal and median raphe nuclei, with some functional considerations. Int Congr Ser. 2007; 1304:98–120.

Vertes, R.; Linley, S. Efferent and afferent connections of the dorsal and median raphe nuclei in the rat. In: Monti, JM.; Pandi-Perumal, SR.; Jacobs, BL.; Nutt, DJ., editors. Serotonin and Sleep: Molecular, Functional and Clinical Aspects. Birkhäuser; Verlag/Switzerland: 2008. p. 69-102.

Vertes RP. A PHA-L analysis of ascending projections of the dorsal raphe nucleus in the rat. J Comp Neurol. 1991; 313:643–668. [PubMed: 1783685]

Vertes RP. Differential projections of the infralimbic and prelimbic cortex in the rat. Synapse. 2004; 51:32–58. [PubMed: 14579424]

Wang QP, Nakai Y. The dorsal raphe: an important nucleus in pain modulation. Brain Res Bull. 1994; 34:575–585. [PubMed: 7922601]

Warden MR, Selimbeyoglu A, Mirzabekov JJ, Lo M, Thompson KR, Kim SY, Adhikari A, Tye KM, Frank LM, Deisseroth K. A prefrontal cortex-brainstem neuronal projection that controls response to behavioural challenge. Nature. 2012; 492:428–32. [PubMed: 23160494]

Wiklund L, Léager L, Persson M. Monoamine cell distribution in the cat brain stem. A fluorescence histochemical study with quantification of indolaminergic and locus coeruleus cell groups. J Comp Neurol. 1981; 203:613–647. [PubMed: 7328202]

Woods RP, Cherry SR, Mazziotta JC. Rapid automated algorithm for aligning and reslicing PET images. J Comput Assist Tomogr. 1992; 16:620–633. [PubMed: 1629424]

Highlights

- We investigated serotonin-related resting-state functional connectivity (FC).

- We present a novel multi-modal method for delineating the dorsal and median raphe.

- Functional connectivity of these nuclei at rest was evaluated.

- Brain regions functionally connected to the raphe nuclei were identified.

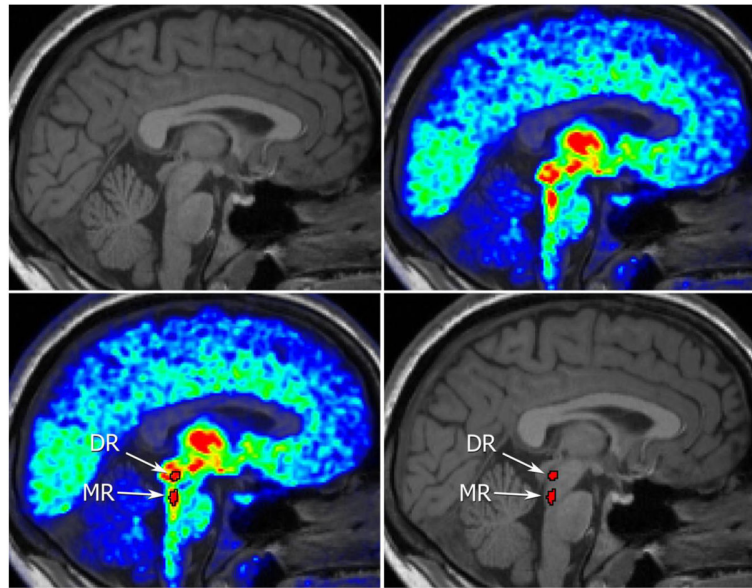- Raphe FC was positively associated with serotonin transporter binding.

Figure 1.
(A) Structural MRI image. The raphe nuclei are not identifiable. (B) [^{11}C]DASB PET image superimposed on the corresponding structural image, highlighting the 5-HTT system. The raphe nuclei are visible within brainstem as regions of higher binding. (C)Delineation of the DR and MR nuclei based on [^{11}C]DASB PET. (D) DR and MR identified from the [^{11}C]DASB PET image transferred as seeds onto the structural image.
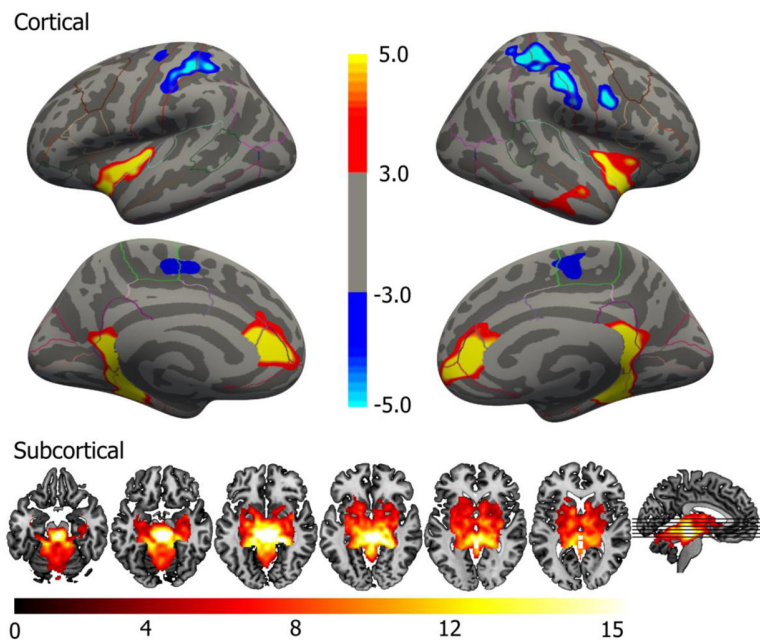
Figure 2.
Group-level FC map for the DR seed, inflated cortical surface and in volume. The map displays clusters of statistically significant FC, corrected for multiple comparisons. Color scales reflect -log$_{10}$(p) values. Negative p-values (blue) are used to denote regions exhibiting negative FC. The six axial slices correspond to Z = −20, −15, −10, −5, 0 and 5 (left to right). Right is right in axial images.
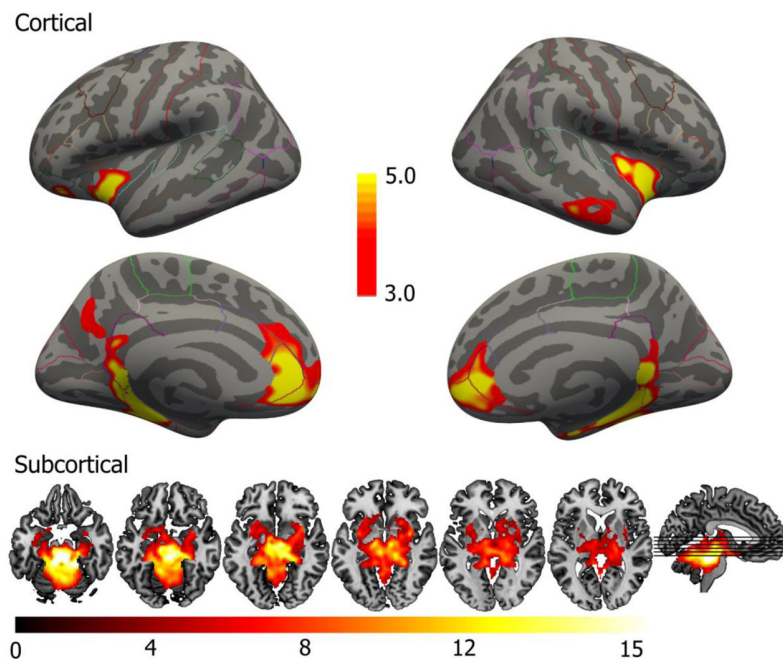
Figure 3.
Group-level FC map for the MR seed, inflated cortical surface and in volume. The map displays clusters of statistically significant FC, corrected for multiple comparisons. Color scales reflect $-\log_{10}(p)$ values. No statistically significant negative FC was observed. The six axial slices correspond to Z = −20, −15, −10, −5, 0 and 5 (left to right). Right is right in axial images.
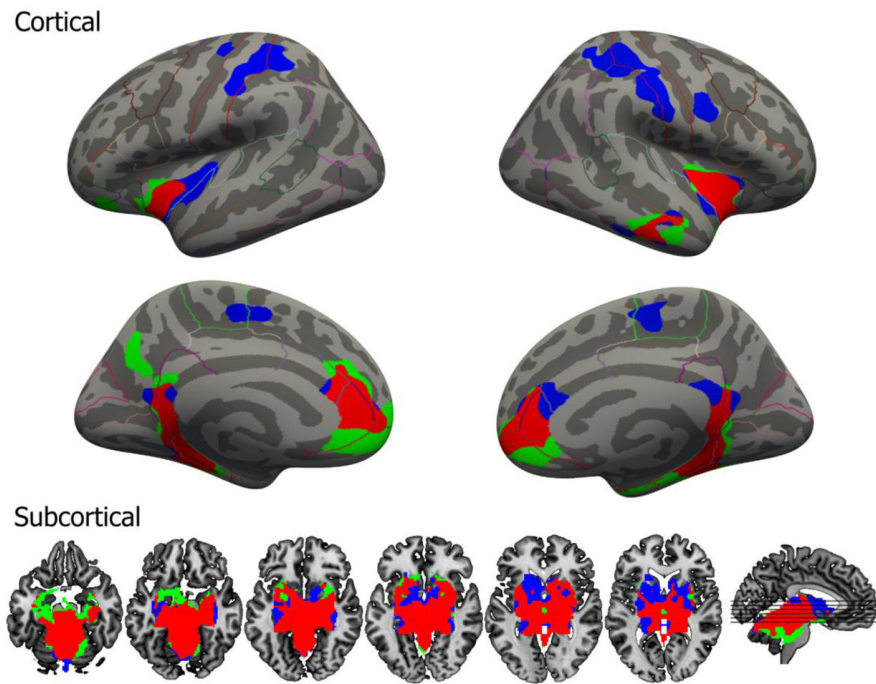
Figure 4.
Overlap of significant negative or positive FC of DR and MR. Blue corresponds to DR only, green MR only and red is the overlap between DR and MR. Most clusters overlap to some extent, except for the pre- and postcentral gyrus for DR. The six axial slices correspond to Z = −20, −15, −10, −5, 0 and 5 (left to right), right is right in axial images.
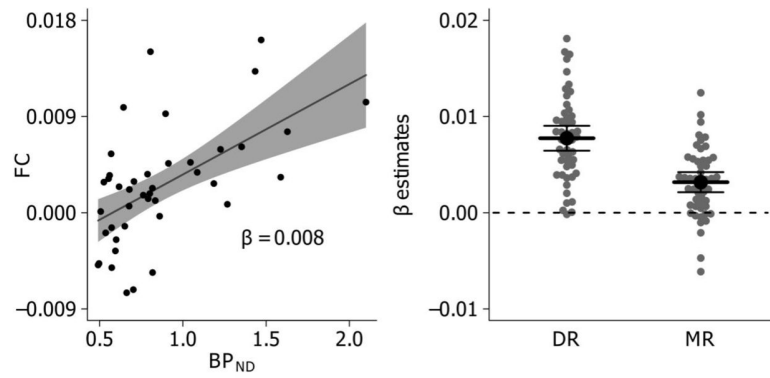
Figure 5.
(A) Example of single-subject association between [^{11}C]DASB BP$_{ND}$ vs. FC with DR across 42 brain regions (see section 2.6 for details). β represents the slope estimate and shading along line represents 95% confidence interval (CI) on slope estimate. (B) Gray points reflect single subject slope estimates for each respective seed and black dots and lines reflects mean and 95% CI across subjects. The DR and MR slope estimates are mostly positive, indicating a positive association between 5-HTT binding and raphe FC in the vast majority of individuals.

Significant clusters functionally connected with the DR at rest.

Region	Cluster p-value	Size (mm²)	MNI		
			X	Y	Z
Positive FC					
Left Cortical Hemisphere					
Parahippocampal gyrus	0.0001	1581	−18	−39	−6
Insula	0.0001	1040	−34	−16	−6
Rostral anterior cingulate gyrus	0.0001	805	−6	37	8
Right Cortical Hemisphere					
Parahippocampal gyrus	0.0001	1737	19	−35	−9
Medial orbitofrontal gyrus	0.0001	1073	14	43	−3
Insula	0.0001	1043	38	−4	−12
Superior temporal gyrus	0.0003	486	48	−12	−18
Negative FC					
Left Cortical Hemisphere					
Postcentral gyrus	0.0001	1337	−39	−33	47
Precentral gyrus	0.0112	295	−34	−22	58
Superior frontal gyrus	0.0121	291	−7	−7	51
Right Cortical Hemisphere					
Superior parietal gyrus	0.0001	2181	32	−44	48
Precentral gyrus	0.0037	359	57	7	29
Paracentral gyrus	0.0122	289	12	−19	47

Region	Cluster p-value	Size v	MNI		
			X	Y	Z
Subcortical					
Brainstem J Jan	<0.0001	197264	−29	−11	27

Table 2

Significant clusters functionally connected with the MR at rest.

Region	Cluster p-value	Size (mm²)	MNI		
			X	Y	Z
Left Cortical Hemisphere					
Rostral anterior cingulate gyrus	0.0001	2393	−6	41	−1
Parahippocampal gyrus	0.0001	1811	−28	−36	−16
Insula	0.0001	765	−30	13	−13
Precuneus	0.0042	361	−7	−68	30
Lateral orbitofrontal cortex	0.0140	278	−35	33	−10
Right Cortical Hemisphere					
Parahippocampal gyrus	0.0001	2585	24	−29	−20
Rostral anterior cingulate gyrus	0.0001	1255	7	39	−1
Insula	0.0001	1104	36	8	−12
Middle temporal gyrus	0.0001	674	62	−23	−18

Region	Cluster p-value	Size (mm³)	MNI		
			X	Y	Z
Subcortical					
Brainstem	<0.0001	228744	−35	−21	29

Systems/Circuits

A High-Resolution *In Vivo* Atlas of the Human Brain's Serotonin System

Vincent Beliveau,[1,2] Melanie Ganz,[1] Ling Feng,[1] Brice Ozenne,[1,3] Liselotte Højgaard,[2,4] Patrick M. Fisher,[1] Claus Svarer,[1] Douglas N. Greve,[5,6] and Gitte M. Knudsen[1,2]

[1]Neurobiology Research Unit and Center for Integrated Molecular Brain Imaging, Rigshospitalet, [2]Faculty of Health and Medical Sciences, [3]Department of Public Health, Section of Biostatistics, and [4]PET and Cyclotron Unit, Copenhagen University Hospital, Rigshospitalet, DK-2100 Copenhagen, Denmark, [5]Athinoula A. Martinos Center for Biomedical Imaging, Department of Radiology, Massachusetts General Hospital, Boston, Massachusetts 02129, and [6]Harvard Medical School, Boston, Massachusetts 02115

The serotonin (5-hydroxytryptamine, 5-HT) system modulates many important brain functions and is critically involved in many neuropsychiatric disorders. Here, we present a high-resolution, multidimensional, *in vivo* atlas of four of the human brain's 5-HT receptors ($5\text{-}HT_{1A}$, $5\text{-}HT_{1B}$, $5\text{-}HT_{2A}$, and $5\text{-}HT_4$) and the 5-HT transporter (5-HTT). The atlas is created from molecular and structural high-resolution neuroimaging data consisting of positron emission tomography (PET) and magnetic resonance imaging (MRI) scans acquired in a total of 210 healthy individuals. Comparison of the regional PET binding measures with postmortem human brain autoradiography outcomes showed a high correlation for the five 5-HT targets and this enabled us to transform the atlas to represent protein densities (in picomoles per milliliter). We also assessed the regional association between protein concentration and mRNA expression in the human brain by comparing the 5-HT density across the atlas with data from the Allen Human Brain atlas and identified receptor- and transporter-specific associations that show the regional relation between the two measures. Together, these data provide unparalleled insight into the serotonin system of the human brain.

Key words: 5-HT; atlas; autoradiography; MRI; mRNA; PET

Significance Statement

We present a high-resolution positron emission tomography (PET)- and magnetic resonance imaging-based human brain atlas of important serotonin receptors and the transporter. The regional PET-derived binding measures correlate strongly with the corresponding autoradiography protein levels. The strong correlation enables the transformation of the PET-derived human brain atlas into a protein density map of the serotonin (5-hydroxytryptamine, 5-HT) system. Next, we compared the regional receptor/transporter protein densities with mRNA levels and uncovered unique associations between protein expression and density at high detail. This new *in vivo* neuroimaging atlas of the 5-HT system not only provides insight in the human brain's regional protein synthesis, transport, and density, but also represents a valuable source of information for the neuroscience community as a comparative instrument to assess brain disorders.

Introduction

Serotonin (5-hydroxytryptamine, 5-HT) is a highly evolutionary conserved monoamine neurotransmitter that, across species, modulates multiple psychophysiological functions. In the human brain, 5-HT is synthesized within the brainstem's raphe nuclei, which have distributed efferent and afferent projections through-

Table 1. Demographics of healthy subjects

Receptor/transporter	5-HTT	5-HT$_{1A}$R	5-HT$_{1B}$R	5-HT$_{2A}$R	5-HT$_4$R
Radioligand	[^{11}C]DASB	[^{11}C]CUMI-101	[^{11}C]AZ10419369	[^{11}C]Cimbi-36	[^{11}C]SB207145
N	100	8	36	29	59
Gender (M/F)	29/71	3/5	24/12	15/14	41/18
Age (mean ± SD)	25.1 ± 5.8	28.4 ± 8.8	27.8 ± 6.9	22.6 ± 2.7	25.9 ± 5.3
BMI (kg/m^2, mean ± SD)	23.2 ± 2.9	22.7 ± 2.6	24.9 ± 4.3	23.4 ± 2.4	23.5 ± 3.3
Injected dose (MBq, mean ± SD)	586.0 ± 32.2	510.5 ± 149.1	585.4 ± 37.4	510.4 ± 109.7	577.1 ± 70.9
Injected mass (μg, mean ± SD)	1.9 ± 2.2	2.0 ± 1.5	1.2 ± 1.0	0.8 ± 0.5	1.1 ± 0.7

out the brain (Dorocic et al., 2014). The 5-HT system is highly diverse (Hannon and Hoyer, 2008). Based on structural, transductional, and operational features, its receptors have been grouped into seven families of receptors (5-HT$_1$ to 5-HT$_7$), including 14 known subtypes, and a transporter (5-HTT). Of the 14 receptors, there are 13 distinct G-protein-coupled receptors and one ligand-gated ion channel receptor, 5-HT$_3$. 5-HT is involved in myriad physiological functions such as cognition (Meneses, 1999), mood and social interaction (Young and Leyton, 2002), sexual behavior (Waldinger, 2015), feeding behavior (Magalhães et al., 2010), the sleep–wake cycle (Portas et al., 2000), and thermoregulation (Cryan et al., 2000). Disturbances in the 5-HT system are also linked to many debilitating brain disorders such as major depression, anxiety, and schizophrenia, as well as migraine and neurodegenerative disorders (Muller and Jacobs, 2009). The role of the individual receptors in the different functions and disorders is, however, only partially known. A prominent example is that, even though the 5-HTT inhibitors (selective serotonin reuptake inhibitors) are the most frequently prescribed antidepressant drug class, the exact involvement of individual 5-HT receptors in mediating their clinical effects is still unclear. To study the role of the individual receptors in healthy individuals, in patients with brain disorders, and in response to physiological or drug interventions, *in vivo* molecular brain imaging with positron emission tomography (PET) in conjunction with an appropriate radiotracer represents the state-of-the-art approach for quantifying the density and spatial distribution of brain receptors and transporters.

Brain atlases play a key role in neuroimaging research. Stereotactic atlases of magnetic resonance imaging (MRI) brain morphology such as the Talairach (Talairach and Tournoux, 1988) and the Montreal Neurological Institute (MNI) atlas (Evans et al., 1992) have become fundamental pillars for performing group analysis and anatomical segmentations such as the Automated Anatomical Labeling atlas (Tzourio-Mazoyer et al., 2002) are commonly used to report results of regional outcomes of brain imaging data. A high-resolution human brain atlas of 5-HT receptors will represent a valuable tool for neuroimaging studies investigating the 5-HT system and disorders related to its dysfunction.

The distribution of 5-HT receptors in the human postmortem brain has in the past been described extensively by autoradiography. However, autoradiography measurements, although quantitative, provide far less spatial information than a whole-brain atlas. With the development of well validated radioligands for imaging the 5-HT system *in vivo*, it is now possible to image specific 5-HT receptor subtypes and the 5-HTT. Up to now, specific and validated PET radioligands for use in humans have been developed for the receptors 5-HT$_{1A}$R, 5-HT$_{1B}$R, 5-HT$_{2A}$R, and 5-HT$_4$R and for 5-HTT (Paterson and Kornum, 2013). A radioligand for the 5-HT$_6$ receptor has been validated in humans (Parker et al., 2012), but was not included here because it also has high affinity to the 5-HT$_{2A}$ receptor (Parker et al., 2015).

We here present an MRI- and PET-based high-resolution atlas of the human brain 5-HT receptors 5-HT$_{1A}$R, 5-HT$_{1B}$R, 5-HT$_{2A}$R, and 5-HT$_4$R and the 5-HTT, represented both in volume and on the cortical surface. The atlas was generated using a subset of the Center for Integrated Molecular and Brain Imaging's (Cimbi's) extensive database (Knudsen et al., 2015), including 210 healthy volunteers aged between 18 and 45 years. Regional PET binding values were compared with corresponding postmortem autoradiography data (Bonaventure et al., 2000; Varnäs et al., 2004), allowing us to validate our results and convert binding values into densities (Bmax). Furthermore, regional densities were compared with mRNA levels from the Allen Human Brain Atlas (Hawrylycz et al., 2012; French and Paus, 2015) to confirm previous findings and to gain novel insights into the localization of the receptor/transporter protein versus its expression.

Materials and Methods

Participants. All participants included in this study were healthy male and female controls from the Cimbi database (Knudsen et al., 2015); all data from this database are freely accessible. The data analysis was restricted to include individuals aged between 18 and 45 years. Participants were recruited by advertisement for different research protocols approved by the Ethics Committee of Copenhagen and Frederiksberg, Denmark. A total of 232 PET scans and corresponding structural MRI scans were acquired for 210 individual participants; 189 subjects had only one scan, 20 subjects had two scans, and a single had three scans. Demographics details are presented in Table 1.

PET and structural MRI. PET data were acquired in list mode on a Siemens HRRT scanner operating in 3D acquisition mode with an approximate in-plane resolution of 2 mm (1.4 mm in the center of the field of view and 2.4 mm in cortex; Olesen et al., 2009). PET frames were reconstructed using a 3D–OSEM–PSF algorithm (Comtat et al., 2008; Sureau et al., 2008). Scan time and frame length were designed according to the radiotracer characteristics. Dynamic PET frames were realigned using AIR 5.2.5 (Woods et al., 1992; see Table 2 for details on framing and realignment). T1- and T2-weighted structural MRI were acquired on four different Siemens scanners with standard parameters. All structural MRIs (T1 and T2) were unwarped offline using FreeSurfer's gradient_nonlin_unwarp version 0.8 or online on the scanner (Jovicich et al., 2006). For further details on structural MRI acquisition parameters, see Knudsen et al. (2015).

Further processing was performed with FreeSurfer 5.3 (Fischl, 2012; http://surfer.nmr.mgh.harvard.edu) using a surface and a volume stream. The individual cortical surfaces were reconstructed using the structural MRI corrected for gradient nonlinearities. The pial surfaces were further refined using T2-weighted structural images and corrected manually where necessary. PET–MR coregistration was estimated using boundary-based registration (Greve and Fischl, 2009) between the time-weighted sum of the PET time–activity curves (TACs) and the structural MRI. Additionally, the transformation from individual MR space to normal MNI152 space was estimated with combined volume–surface (CVS) registration (Postelnicu et al., 2009).

Regional TACs for the cortical regions were extracted by resampling the TACs to the cortical surface (Greve and Fischl, 2009) and taking the average within each of the 34 regions defined by the Desikan–Killiany

Table 2. PET scanning and realignment parameters

Radioligand	[^{11}C]DASB	[^{11}C]CUMI-101	[^{11}C]AZ10419369	[^{11}C]Cimbi-36	[^{11}C]SB207145
Scan time (min)	90	120	90	120	120
Frame lengths (number × sec)	6 × 10, 3 × 20, 6 × 30, 5 × 60, 5 × 120, 8 × 300, 3 × 600	6 × 5, 10 × 15, 4 × 30, 5 × 120, 5 × 300, 8 × 600	6 × 10, 6 × 20, 6 × 60, 8 × 120, 19 × 300	6 × 10, 6 × 20, 6 × 60, 8 × 120, 19 × 300	6 × 5, 10 × 15, 4 × 30, 5 × 120, 5 × 300, 8 × 600
Realigned frames (first:last)	10:36	10:38	13:45	13:45	10:38
Reference frame	26	26	27	27	26

cortical atlas (Desikan et al., 2006) automatically labeled by FreeSurfer. Similarly, regional TACs for seven subcortical regions were obtained by resampling the TACs to an MR-based refined version of the automatic volume segmentation derived by FreeSurfer for each subjects as described in Greve et al. (2016). In addition, a segmentation of cerebellum including different lobules (e.g., vermis) were created using SUIT 2.7 (Diedrichsen, 2006) and SPM12 (http://www.fil.ion.ucl.ac.uk/spm). Gray matter cerebellar segmentations used as reference region were created by limiting the FS segmentation to the intersection with the cerebellum labeled by SUIT, excluding vermis; this has the effect of removing peripheral overlabeling sometimes present in the cerebellar segmentations.

Due to the high binding of [^{11}C]DASB and [^{11}C]CUMI-101 within dorsal and median raphe, these ROIs can be delineated directly on PET images. Raphe TACs were obtained by delineating the ROIs on the time-weighted summed TACs using anatomical landmarks from structural MRI according to the method described in Beliveau et al. (2015) and extracting the average TACs within these regions. For the other tracers, raphe TACs were obtained by taking the average within normalized dorsal and median raphe templates. These templates were created by transferring the raphe ROIs previously derived to common space (MNI152) using CVS and taking the voxels with the highest overlap with a target volume of 150 mm^3 and 100 mm^3 for dorsal and median raphe, respectively. The delineations and templates were transferred back to PET space using CVS.

Subcortical voxelwise TACs in common volume space (MNI152) were obtained using CVS. Cortical vertexwise TACs in common surface space (fsaverage) were obtained using the cortical surface alignment estimated by FreeSurfer (Fischl et al., 1999). Finally, cortical and subcortical TACs were surface smoothed by 10 mm and volume smoothed by 5 mm full-width at half-maximum, respectively.

Kinetic modeling. For all radioligands, modeling of the parametric and regional nondisplaceable binding potential (BP$_{ND}$) was performed using the FS PET pipeline (Greve et al., 2013) with a Multilinear Reference Tissue Model 2 (MRTM2) (Ichise et al., 2003) using cerebellar gray matter, excluding vermis, as a reference region. The reference region washout rate (k$_2$′) was computed using MRTM (Ichise et al., 1996); the high-binding TAC was obtained from a surface-weighted average of neocortical regions for [^{11}C]CUMI-101, [^{11}C]AZ10419369, and [^{11}C]Cimbi-36 and from a volume-weighted average of caudate and putamen for [^{11}C]SB207145 and of caudate, putamen, and thalamus for [^{11}C]DASB. Parametric and regional BP$_{ND}$ were thresholded between 0 and 10 (outliers were set to the corresponding threshold value) and average maps were created. For 5-HTT, the TAC of the median raphe was found to be irreversible within the scan time, so the BP$_{ND}$ for this region is not reported and it was disregarded from further analysis.

In vivo binding and autoradiography. To compare our results with those of Varnäs et al. (2004) and Bonaventure et al. (2000), regional values were adapted. First, the autoradiography data from Varnäs et al. (2004) was averaged across layers for individual cortical regions and divisions of subcortical structures were averaged to generate larger identifiable structures. Then, each region of the Desikan–Killiany cortical atlas (both left and right independently) and each subcortical region were grouped according to a set of regions common to the autoradiography data. Regional BP$_{ND}$ values were then averaged within group using a volume/surface weighting. Regions where no reasonable pairing could be made were disregarded. The association between BP$_{ND}$ and autoradiography was estimated using a linear regression without intercept because a null density is expected to yield null binding and the estimated slopes

were used to transform BP$_{ND}$ into density values. Pearson's and Spearman's correlation coefficients were also computed for all associations. The Shapiro–Wilks test was used to assess the normality of the residuals and the null hypothesis of normality was rejected for $p < 0.1$; whenever the residuals did not pass the test, only the Spearman's correlation coefficient is reported. Densities in units of picomoles per gram of tissue were converted to picomoles per milliliter using an approximate gray matter density of 1.045 g/ml (DiResta et al., 1991).

A linear mixed-effect model was used to investigate the global effect of age and gender on the regional density for the five 5-HT targets. The model included age, gender, and the interaction between age and gender as a fixed effect. Region-specific random effects were used to model regional-specific densities and subject-specific random effects to account for the correlation between the regional measurements of a given individual. To handle different variability in 5-HT density between regions, a separate variance parameter was estimated for each region. To investigate a possible regional-specific effect of age or gender, a separate linear regression was fitted to each region, including age, gender, and a possible interaction between age and gender as covariates. In the global models, the p-values were adjusted for multiple comparison over tracers ($n = 5$) controlling the false discovery at 5% (Benjamini and Hochberg, 1995). Similarly, regional models were corrected for multiple comparisons over regions ($n = 42$). For the entire analysis, the significance threshold was fixed at $p < 0.05$. Regional densities were averaged for left and right hemispheres.

The BP$_{ND}$ of small volume of interest surrounded by low binding tissue can be drastically underestimated due to partial volume effects. As described previously (Savli et al., 2012), this is particularly pronounced in the raphe nuclei for the 5-HTT and 5-HT$_{1A}$R because there is high binding for the corresponding radioligand in this region, but much lower levels in to neighboring white matter tissue of the brainstem. Accordingly, the raphe nuclei density values reported here should be interpreted with caution and, although they are depicted in Figures 1 and 5, this region was excluded from any quantitative analysis for the 5-HTT and the 5-HT$_{1A}$R. Similarly, the 5-HTT BP$_{ND}$ distribution within the globus pallidus was found to be highly heterogeneous due to partial volume effect from the caudate, so this region was also excluded from quantitative analysis for the 5-HTT.

In vivo binding and mRNA levels. Regional binding values were compared with 5-HT receptors and transporter mRNA normalized expression values from the Allen Human Brain Atlas (Hawrylycz et al., 2012). The atlas contains probe information from six human brains. Each probe is associated with mRNA levels (log2 intensity) for all genes sequenced, an anatomical label, and coordinates in the MNI152 space, as well as many other parameters. For more details on the materials and methods for the Allen Human Brain Atlas, see the Microarray Survey Technical White papers available at http://help.brain-map.org/display/human-brain/Documentation. mRNA expression values for regions of the Desikan–Killiany cortical atlas were obtained from the work of French and Paus (2015). Each probe of the Allen Human Brain Atlas was paired to a cortical region using its coordinates in the MNI152 space and regional expression values were obtained by averaging expression values across probes, finding the median per region, and finally finding the median across subjects. We used the same approach to obtain subcortical expression values, but probes were paired to subcortical regions directly by their anatomical label rather than using their coordinates to identify corresponding regions. Both binding values and mRNA values were averaged between left and right hemispheres. As above, the association between binding and mRNA was estimated using a linear regression and
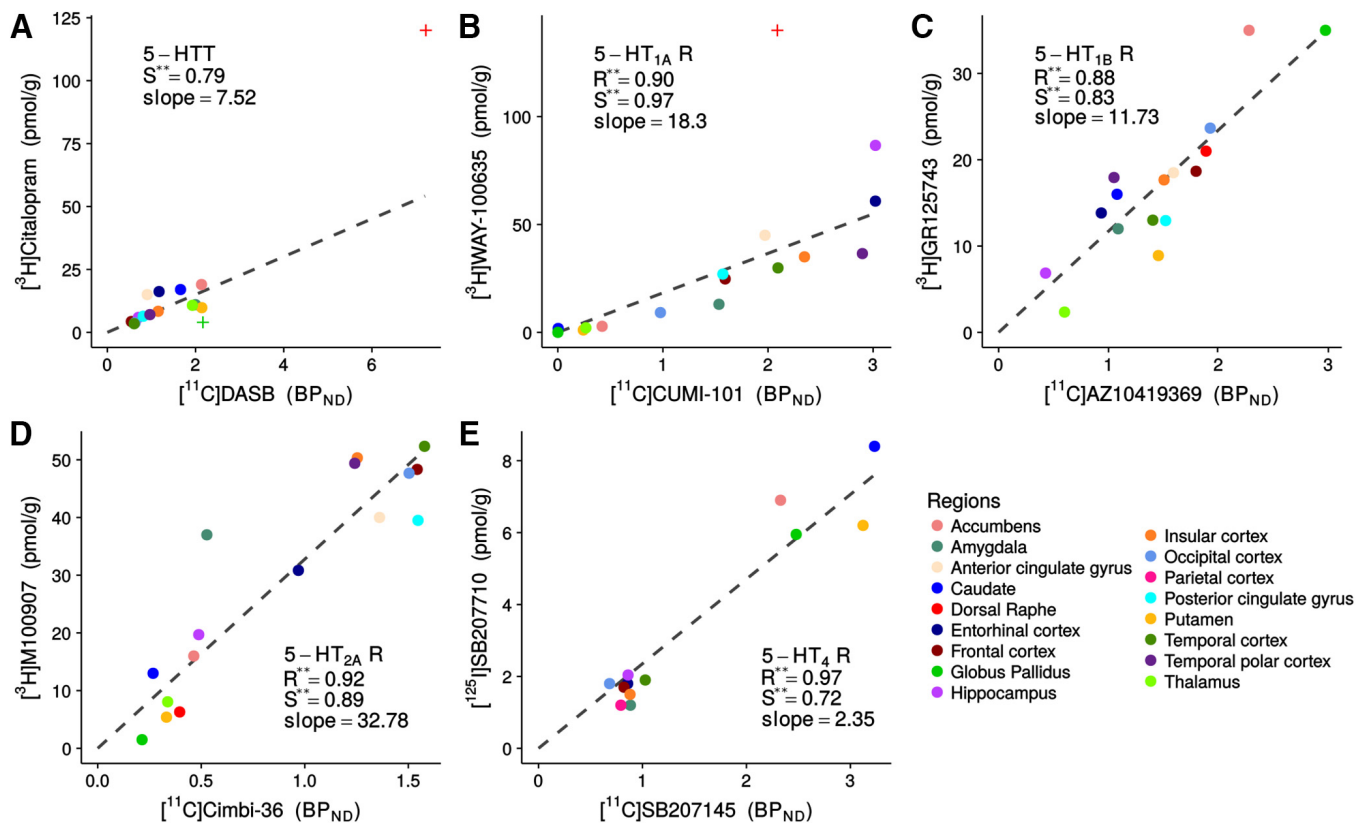
Figure 1. Regional BP_{ND} and B_{max} values for the five 5-HT targets: 5-HTT, 5-HT$_{1A}$R, 5-HT$_{1B}$R, 5-HT$_{2A}$R, and 5-HT$_4$R (*A–E*). The regions in the PET image space were combined to match the regions used by Varnäs et al. (2004) and Bonaventure et al. (2000) in their autoradiography measurement. The regressions (fixed through 0.0) are shown as black, dashed lines and the Pearson's (R) and Spearman's (S) correlation coefficients are reported. **p < 0.001. Dorsal raphe, median raphe, and globus pallidus for 5-HTT and dorsal raphe for 5-HT$_{1A}$R were excluded from the regressions and marked with + on the figure (see Materials and Methods).

Pearson's and Spearman's correlation coefficients were also computed for all association. Dorsal raphe was excluded from the regression for 5-HTT and 5-HT$_{1A}$R and the regression was performed for cortical regions only for the 5-HT$_{2A}$R. For 5-HT$_{1B}$R and 5-HT$_{2A}$R, subcortical regions exhibited patterns distinct from the cortical regions, so the analysis was stratified between cortical and subcortical regions for these two targets.

Results

In vivo molecular imaging and autoradiography

Brain regional BP_{ND} values were compared with the corresponding receptor density measurements from postmortem autoradiography data from Varnäs et al. (2004) and Bonaventure et al. (2000) (for 5-HT$_4$R). Figure 1, *A–E*, shows the relation between autoradiography receptor/transporter B_{max} (density) from the two studies and PET measures of BP_{ND} from the Cimbi database. For all five targets, we found good to excellent associations between BP_{ND} and B_{max}, with Pearson's correlation coefficients ranging from 0.88 to 0.97 and Spearman's correlation coefficients ranging from 0.72 to 0.97. For 5-HTT, the residuals for 5-HTT did not pass the Shapiro–Wilks test for normality, so the Pearson's correlation is not reported for that association. The slope estimates of the regression were used to transform the BP_{ND} atlases into B_{max} atlases (Figs. 2,), allowing for a direct comparison across targets. The regional densities are presented in Figure 4. No global or regional significant effect of age, gender, or their interaction was found.

Receptor density and mRNA

The associations between *in vivo* receptor density, obtained by converting BP_{ND} into densities, and mRNA levels are shown in

Figure 5. For the 5-HT$_{1A}$R, we found excellent correlation between the protein densities and mRNA levels, with Pearson's and Spearman's correlation coefficients of 0.94 and of 0.94, respectively. For 5-HT$_4$, the residuals did not pass the Shapiro–Wilks test for normality, but we found a moderate Spearman's correlation coefficient of 0.50. The 5-HT$_{1B}$R and 5-HT$_{2A}$R showed a distinctly different pattern compared with other targets, with good Pearson's correlation coefficients (0.66 and 0.60, respectively) and weak to moderate Spearman's correlation coefficients (0.28 and 0.46) in cortical regions, but there was no statistically significant correlation in subcortical regions.

Discussion

Here, we present the first high-resolution PET- and MRI-based *in vivo* human brain atlas of four 5-HT receptors and the transporter. The atlas highlights key features of the 5-HT targets, their spatial distribution, and abundance relative to each other. Because we identified high correlations with postmortem autoradiography receptor measurements, the atlas could be calibrated to represent absolute receptor or transporter densities, thus making it independent of the PET methodology in terms of choice of radiotracer and modeling approach. Access to such a high-resolution atlas of the 5-HT system enables scientists not only to evaluate the absolute densities of the individual targets, but also the relative abundance of protein and in any brain region of interest. However, a few caveats with this approach deserve to be mentioned here. Whereas autoradiography provides a measurement of the target density, PET returns an outcome measure that is proportional to the density of the target available for radioligand binding and the measure most notably depends on the *in*
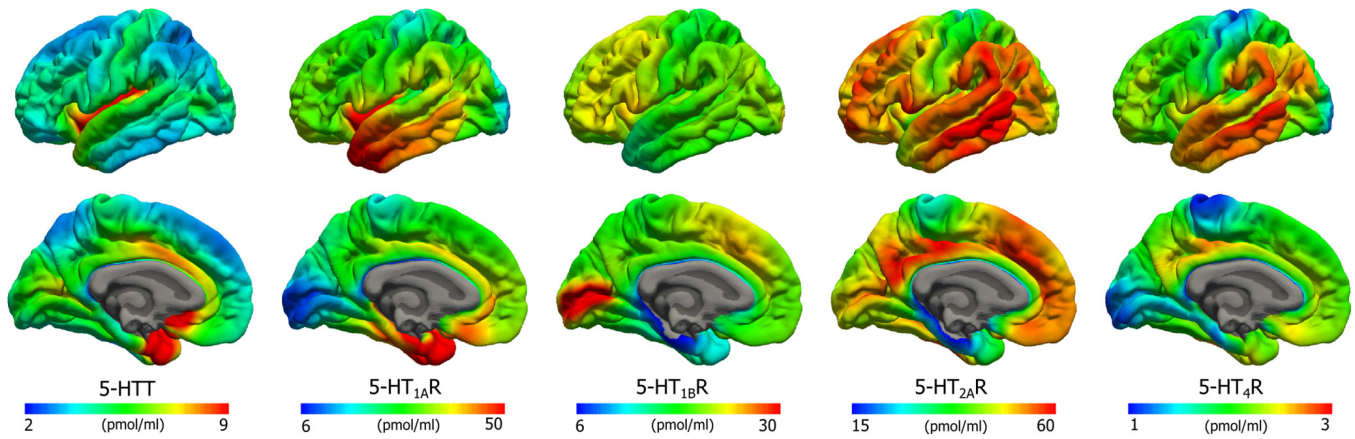
Figure 2. Average density (B_{max}) maps for five 5-HT targets on the common FreeSurfer surface (left hemisphere; lateral view, upper and medial view, lower). Color scaling was individually adjusted to highlight features of the distributions.
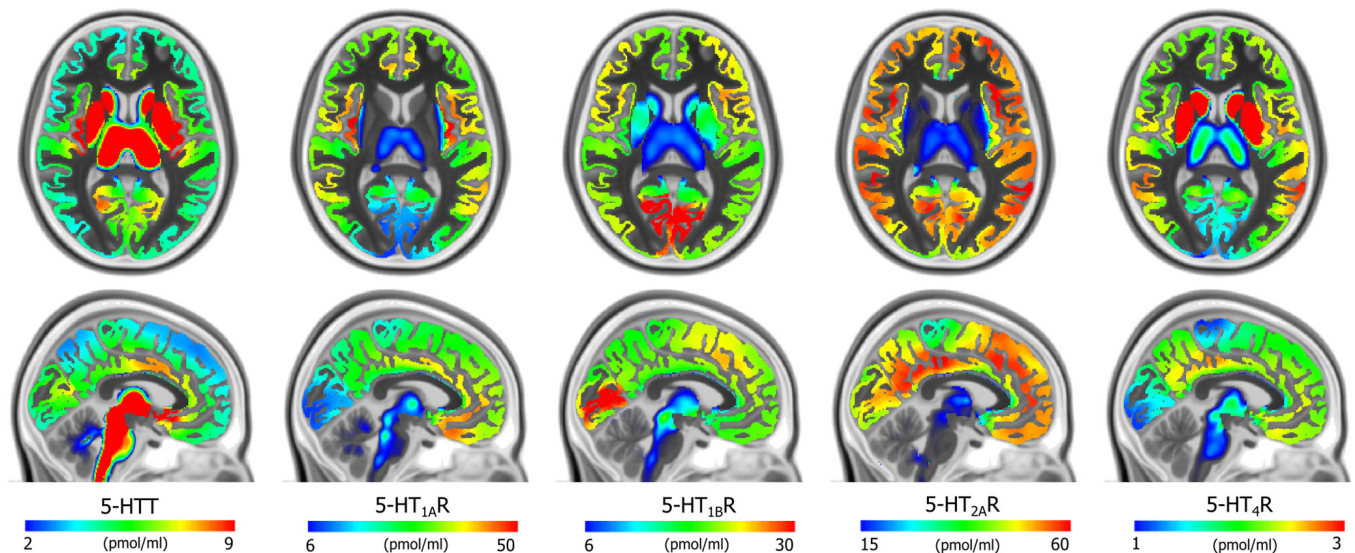

Figure 3. Average density (B_{max}) maps for the five 5-HT targets in the common MNI152 space (coronal, upper, $z = 8$ mm and sagittal, lower, $x = -3$ mm). Color scaling was individually adjusted to highlight features of the distributions.

vivo radioligand affinity to the target. However, because the occupancy of endogenous 5-HT is low for most targets (Paterson et al., 2010), it is unlikely that individual differences in endogenous 5-HT (and thereby *in vivo* affinity) would incur any bias.

Although PET imaging offers unique sensitivity and specificity, the intrinsic image resolution of PET is lower than for MRI. A prior brain 5-HT atlas has been reported based on PET scanners with a resolution of 4.4 mm and was generated independently of anatomical MRI (Savli et al., 2012). Leveraging high-resolution structural MRI ($\sim$1 mm resolution) in combination with molecular images acquired with a high-resolution PET scanner with a resolution of 2 mm allows for precise segmentation of brain regions and accurate intersubject normalization. The surface-based approach used in this work has also been shown to lead to a reduction in bias and variance of PET-derived measurements (Greve et al., 2013). A main advantage of the surface-based method is to diminish partial volume effects introduced by smoothing in the volume; smoothing on the surface drastically reduces the blurring of neighboring tissues with cortical gray matter and blurring across adjacent gyri (Hagler et al., 2006). Nevertheless, we still see subtle signs suggestive of partial volume effects; for example, bands of lower binding along the medial wall

(Figure 6). Although a partial-volume-corrected atlas could be generated, we chose not to do so because methods for partial volume corrections come with their own set of limitations (Harri et al., 2007) and can lead to different results depending on the algorithm used (Greve et al., 2016).

Although [^{11}C]Cimbi-36 has been shown to have some affinity for 5-HT$_{2C}$, these receptors are mostly limited to the choroid plexus and the hippocampus. Furthermore, binding measures for [^{11}C]Cimbi-36 have been shown to be very strongly correlated to those of the 5-HT$_{2A}$ antagonist radiotracer [^{18}F]Altanserin (Ettrup et al., 2016). Therefore, any bias caused by the contribution of 5-HT$_{2C}$ receptors is expected to have minimal impact on the results presented here.

We compared our *in vivo* imaging atlases with meticulous autoradiography studies of the relevant 5-HT targets in postmortem human brain slices (Bonaventure et al., 2000; Varnäs et al., 2004). The postmortem brains in Varnäs et al. (2004) and Bonaventure et al. (2000) were retrieved from individuals older than those included in our study, with a respective mean age of 58 and 55 versus 26 years in our cohort. Therefore, the atlas densities represent those that can be observed in individuals matching the mean age of the population in the autoradiography studies.
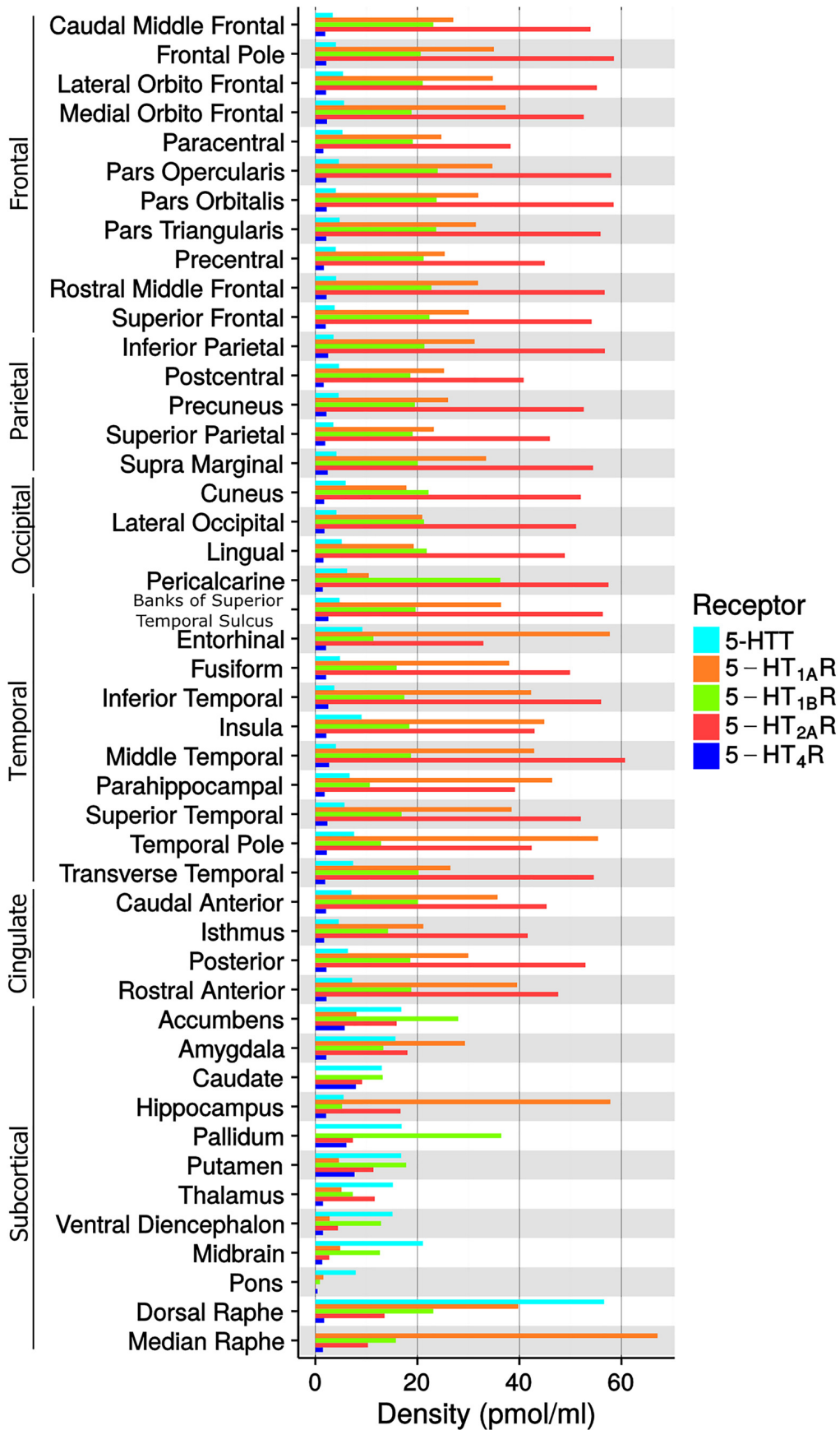
Figure 4. Density values (B_{max}) of the five 5-HT targets in FreeSurfer defined brain regions. Median raphe is not reported for 5-HTT due the irreversible kinetic of the TACs (see Material and Methods).
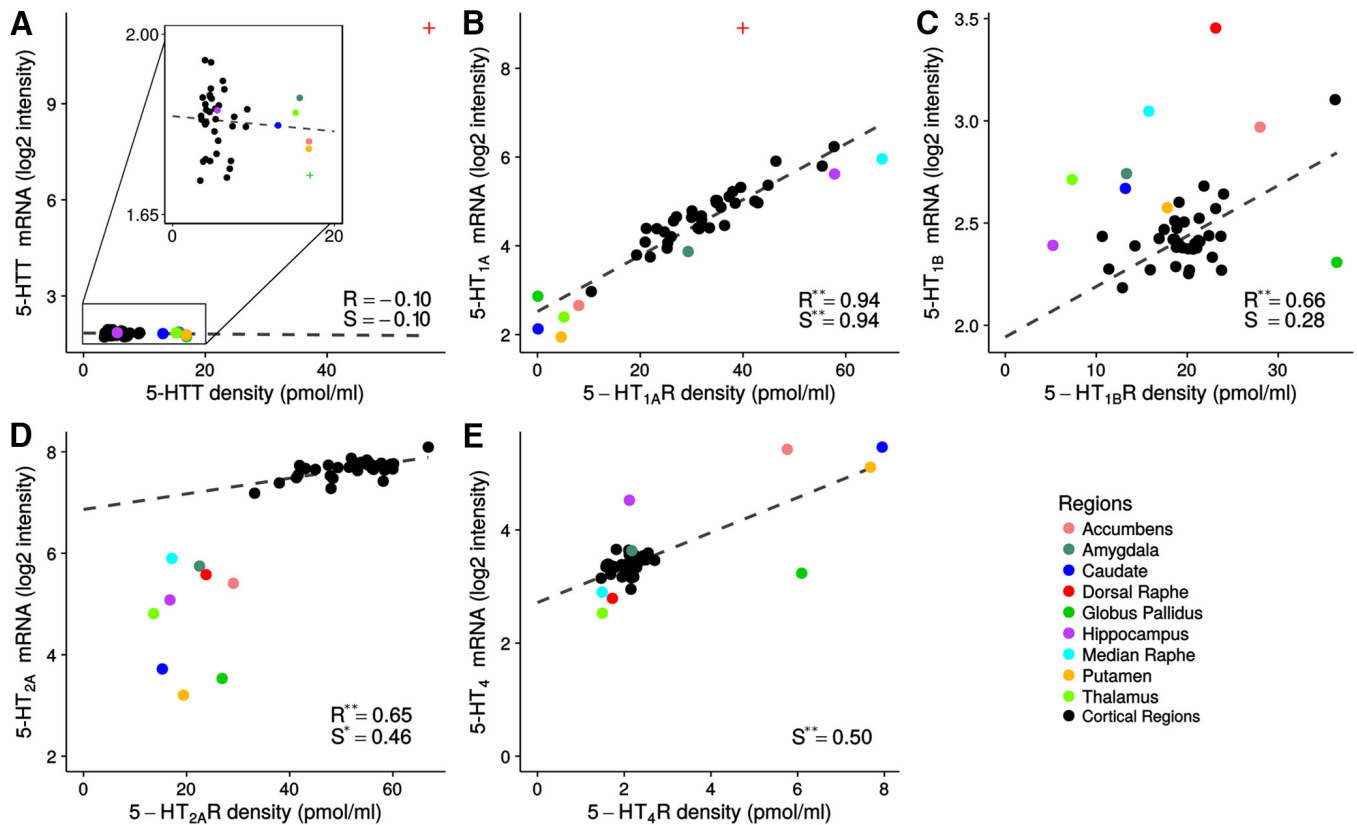
Figure 5. Regional density values (B_{max}) and mRNA levels for the five 5-HT targets: 5-HTT, 5-HT$_{1A}$R, 5-HT$_{1B}$R, 5-HT$_{2A}$R, and 5-HT$_4$R (***A–E***). Subcortical data are shown in color and cortical data are shown in black. The regression lines are shown as black dashed lines and the Pearson's (R) and Spearman's (S) correlation coefficients are reported. *$p < 0.01$; ** $p < 0.001$. In ***C*** and ***D***, a line was fitted to cortical regions (black) only. Dorsal raphe, median raphe, and globus pallidus for 5-HTT and dorsal raphe for 5-HT$_{1A}$R were excluded from the regressions and marked with + on the figure (see Material and Methods).
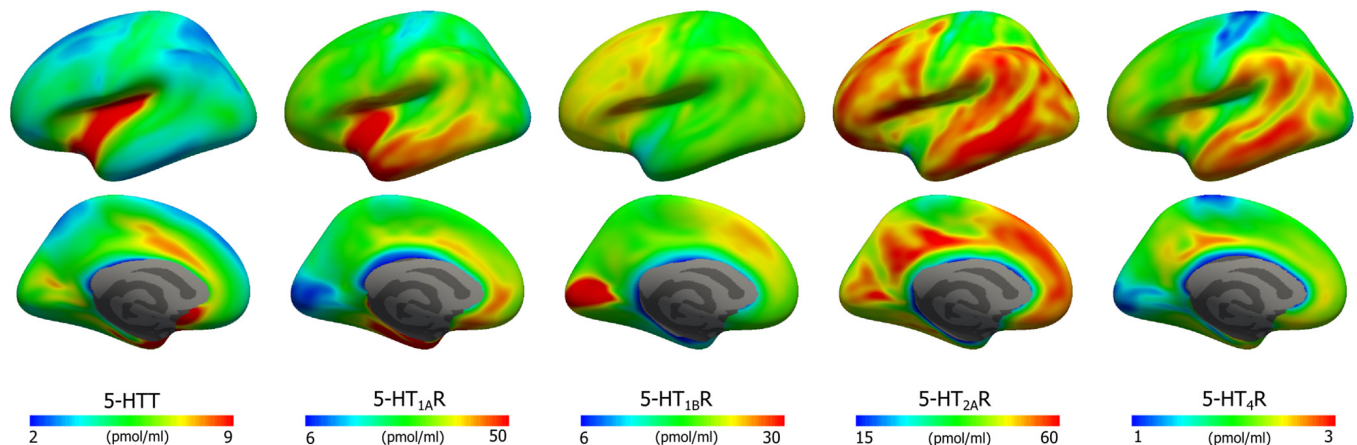

Figure 6. Average density (B_{max}) maps for five 5-HT targets on the inflated common FreeSurfer surface (left hemisphere; lateral view, upper and medial view, lower).

Within the current cohort, we did not observe any significant effect of age or gender within our data, most likely because of the limited age range of the subjects. Whereas some 5-HT targets, such as 5-HT$_{1B}$R and 5-HT$_{2A}$R, are relatively independent of age, others have been shown to have a pronounced age-dependent decline and/or sex differences (Moses-kolko et al., 2011; Nord et al., 2014). Therefore, minor data adjustments may be necessary when relating these atlases to specific research questions.

For all of the serotonergic targets, except for the 5-HT$_{1A}$R (Rizzo et al., 2014), we provide novel information about the relationship between *in vivo* molecular imaging in humans and the associated mRNA levels assessed in postmortem human brain

tissue. The relation between the cerebral 5-HT target densities and their corresponding mRNA levels is of interest as mRNA levels often do not correspond to their protein levels because protein concentrations depend on the relative rates of transcription, mRNA decay, translation, and protein degradation (Vogel et al., 2010). Relating the two measures in brain space generates important information about the gene–protein translation. A high spatial correspondence between the two measures suggests that the protein is located on or at least close to the cell body, where the protein synthesis takes place. We found no significant association between 5-HTT mRNA and 5-HTT density, although, as expected, both were high in the dorsal raphe (Fig. 5*A*).

This is consistent with the exclusively presynaptic localization of 5-HTT and thus primary mRNA localization within raphe nuclei (Hoffman et al., 1998) and 5-HTT protein being located on terminal projections distant from 5-HT neurons (Zhou et al., 1998). The 5-HTT mRNA levels were overall low, both relative to the mRNA of other targets and to the 5-HTT protein density. Consistent with Rizzo et al. (2014), we found a very strong association between 5-HT$_{1A}$R mRNA and 5-HT$_{1A}$R protein density as determined with *in vivo* molecular neuroimaging (Fig. 5B). Rizzo et al. (2014) ascribed the tight correlation to a more general feature of the serotonergic system, but we show here that several other serotonergic targets show profound regional differences. We found a fair association between neocortical 5-HT$_{1B}$R mRNA and 5-HT$_{1B}$R density (Fig. 5C), but the subcortical regions did not conform to this association. As for the latter, our findings are consistent with a previous postmortem human brain study in which proportionally higher levels of 5-HT$_{1B}$R mRNA than protein were found, particularly in the ventral striatum, whereas the pallidum, the brain region with the highest 5-HT$_{1B}$R density, had low mRNA levels (Varnäs et al., 2005). This supports the observation in rodents that 5-HT$_{1B}$Rs in pallidum are localized in nerve terminals from striatal projections (Boschert et al., 1994) that are of GABAergic origin (Ghavami et al., 1999). To the best of our knowledge, existing literature does not provide evidence about the relative densities of 5-HT$_{1B}$R autoreceptors and heteroreceptors in different brain regions, but, due to the specific pattern observed here, we speculate that the 5-HT$_{1B}$R heteroreceptors may be relatively more abundant in subcortical regions. An interesting pattern of 5-HT$_{2A}$R mRNA versus 5-HT$_{2A}$R density emerged: whereas the neocortical brain regions showed a good, linear correlation, there was no association between the two measures in subcortical brain regions (Fig. 5D) and the neocortical and subcortical regions fall in two separate clusters on the graph. This pattern is in agreement with observations in the macaque monkey brain (López-Giménez et al., 2001) and suggests that the regulation and role of the 5-HT$_{2A}$R differ markedly between neocortical and subcortical brain regions, possibly because the 5-HT$_{2A}$R in neocortex are located in the apical part of pyramidal neurons (Jakab and Goldman-Rakic, 2000). In addition, the 5-HT$_{2A}$R mRNA levels are almost twice as high compared with the other investigated targets. We speculate that high mRNA levels enable the system to regulate synaptic 5-HT$_{2A}$R levels quickly, consistent with the ligand-induced endocytosis and recycling of 5-HT$_{2A}$R (Raote et al., 2013). We observed a moderate correlation association between 5-HT$_4$R mRNA and 5-HT$_4$R protein density (Fig. 5E). This finding is consistent with data obtained in humans, where 5-HT$_4$R mRNA levels and densities where high in caudate, putamen, accumbens, and the hippocampus formation and were both relatively lower in other brain regions.

Conclusion

Here, we present a comprehensive PET- and MRI-based high-resolution brain atlas of the serotonin system. By combining the *in vivo* atlases with postmortem autoradiography measurements, we calibrated the individual atlas to represent quantitative protein levels in terms of picomoles per milliliter. Furthermore, we describe the relation between regional serotonergic target densities and their mRNA levels, some for the first time in humans. The approach is generally applicable for any molecular target that can be visualized *in vivo* by PET. Such publicly available *in vivo* human brain atlases will serve as an important resource for neuroscience.

Notes

References

Beliveau V, Svarer C, Frokjaer VG, Knudsen GM, Greve DN, Fisher PM (2015) Functional connectivity of the dorsal and median raphe nuclei at rest. Neuroimage 116:187–195. CrossRef

Benjamini Y, Hochberg Y (1995) Controlling the false discovery rate: a practical and powerful approach to multiple testing. J R Stat Soc Ser B 57:289–300.

Bonaventure P, Hall H, Gommeren W, Cras P, Langlois X, Jurzak M, Leysen JE (2000) Mapping of serotonin 5-HT(4) receptor mRNA and ligand binding sites in the post-mortem human brain. Synapse 36:35–46. CrossRef

Boschert U, Amara DA, Segu L, Hen R (1994) The mouse 5-hydroxytryptamine1B receptor is localized predominantly on axon terminals. Neuroscience 58:167–182. CrossRef

Comtat C, Sureau FC, Sibomana M, Hong IK, Sjoholm N, Trebossen R (2008) Image based resolution modeling for the HRRT OSEM reconstructions software. IEEE Nucl Sci Symp Conf Rec 2008:4120–4123.

Cryan JF, Harkin A, Naughton M, Kelly JP, Leonard BE (2000) Characterization of D-fenfluramine-induced hyperthermia: evidence for multiple sites of action. Eur J Pharmacol 390:275–285. CrossRef

Desikan RS, Ségonne F, Fischl B, Quinn BT, Dickerson BC, Blacker D, Buckner RL, Dale AM, Maguire RP, Hyman BT, Albert MS, Killiany RJ (2006) An automated labeling system for subdividing the human cerebral cortex on MRI scans into gyral based regions of interest. Neuroimage 31:968–980. CrossRef

Diedrichsen JJ (2006) A spatially unbiased atlas template of the human cerebellum. Neuroimage 33:127–138. CrossRef

DiResta GR, Lee J, Arbit E (1991) Measurement of brain tissue specific gravity using pycnometry. J Neurosci Methods 39:245–251. CrossRef

Dorocic IP, Fürth D, Xuan Y, Johansson Y, Pozzi L, Silberberg G, Carlén M, Meletis K (2014) A whole-brain atlas of inputs to serotonergic neurons of the dorsal and median raphe nuclei. Neuron 83:663–678. CrossRef

Ettrup A, Svarer C, McMahon B, da Cunha-Bang S, Lehel S, Møller K, Dyssegaard A, Ganz M, Beliveau V, Jørgensen LM, Gillings N, Knudsen GM (2016) Serotonin 2A receptor agonist binding in the human brain with [(11)C]Cimbi-36: Test-retest reproducibility and head-to-head comparison with the antagonist [(18)F]altanserin. Neuroimage 34:1188–1196.

Evans AC, Collins DL, Milner B (1992) An MRI-based stereotactic atlas from 250 young normal subjects. Soc Neurosci Abstr 18:408.

Fischl B (2012) FreeSurfer. Neuroimage 62:774–781. CrossRef

Fischl B, Sereno MI, Tootell RBH, Dale AM (1999) High-resolution intersubject averaging and a coordinate system for the cortical surface. Hum Brain Mapp 8:272–284. CrossRef

French L, Paus T (2015) A FreeSurfer view of the cortical transcriptome generated from the Allen Human Brain Atlas. Front Neurosci 9:1–5.

Ghavami a, Stark KL, Jareb M, Ramboz S, Ségu L, Hen R (1999) Differential addressing of 5-HT1A and 5-HT1B receptors in epithelial cells and neurons. J Cell Sci 112 Pt 6:967–976.

Greve DN, Fischl B (2009) Accurate and robust brain image alignment using boundary-based registration. Neuroimage 48:63–72. CrossRef

Greve DN, Svarer C, Fisher PM, Feng L, Hansen AE, Baare W, Rosen B, Fischl B, Knudsen GM (2013) Cortical surface-based analysis reduces bias and variance in kinetic modeling of brain PET data. Neuroimage 92C:225–236.

Greve DN, Salat DH, Bowen SL, Izquierdo-Garcia D, Schultz AP, Catana C, Becker JA, Svarer C, Knudsen G, Sperling RA, Johnson KA (2016) Different partial volume correction methods lead to different conclusions: An 18F-FDG PET Study of aging. Neuroimage 132:334–343. CrossRef

Hagler DJ Jr, Saygin A, Sereno M, Hagler D (2006) Smoothing and cluster thresholding for cortical surface-based group analysis of fMRI data. Neuroimage 33:1093–1103. CrossRef

Hannon J, Hoyer D (2008) Molecular biology of 5-HT receptors. Behav Brain Res 195:198–213. CrossRef

Harri M, Mika T, Jussi H, Nevalainen OS, Jarmo H (2007) Evaluation of partial volume effect correction methods for brain positron emission to-

mography: quantification and reproducibility. J Med Phys 32:108–117. CrossRef

Hawrylycz MJ et al. (2012) An anatomically comprehensive atlas of the adult human brain transcriptome. Nature 489:391–399. CrossRef

Hoffman BJ, Hansson SR, Mezey E, Palkovits M (1998) Localization and dynamic regulation of biogenic amine transporters in the mammalian central nervous system. Front Neuroendocrinol 19:187–231. CrossRef

Ichise M, Ballinger J, Golan H (1996) Noninvasive quantification of dopamine D2 receptors with iodine-123-IBF SPECT. J Nucl Med 37:513–520.

Ichise M, Liow JS, Lu JQ, Takano A, Model K, Toyama H, Suhara T, Suzuki K, Innis RB, Carson RE (2003) Reference tissue parametric imaging methods: application to [11C] DASB positron emission tomography studies of the serotonin transporter in human brain. J Cereb Blood Flow Metab 23:1096–1112.

Jakab RL, Goldman-Rakic PS (2000) Segregation of serotonin 5-HT2A and 5-HT3 receptors in inhibitory circuits of the primate cerebral cortex. J Comp Neurol 417:337–348. CrossRef

Jovicich J, Czanner S, Greve D, Haley E, van der Kouwe A, Gollub R, Kennedy D, Schmitt F, Brown G, Macfall J, Fischl B, Dale A (2006) Reliability in multi-site structural MRI studies: effects of gradient non-linearity correction on phantom and human data. Neuroimage 30:436–443. CrossRef

Knudsen GM et al. (2015) The Center for Integrated Molecular Brain Imaging (Cimbi) Database. Neuroimage 124:1213–1219.

López-Giménez J, Vilaro TM, Palacios JM, Mengod G (2001) Mapping of 5-HT2A receptors and their mRNA in monkey brain: [3H]MDL100,907 autoradiography and in situ hybridization studies. J Comp Neurol 429: 571–589. CrossRef

Magalhães CP, de Freitas MFL, Nogueira MI, Campina RCDF, Takase LF, de Souza SL, de Castro RM (2010) Modulatory role of serotonin on feeding behavior. Nutr Neurosci 13:246–255. CrossRef

Meneses A (1999) 5-HT system and cognition. Neurosci Biobehav Rev 23: 1111–1125. CrossRef

Moses-kolko EL, Price JC, Shah N, Berga S, Sereika SM, Fisher PM, Coleman R, Becker C, Mason NS, Loucks T, Meltzer CC (2011) Age, sex, and reproductive hormone effects on brain serotonin-1A and serotonin-2A receptor binding in a healthy population. Neuropsychopharmacology 36: 2729–2740. CrossRef

Muller CP, Jacobs B (2009) Handbook of the Behavioral Neurobiology of Serotonin. Cambridge, MA: Academic Press.

Nord M, Cselenyi Z, Forsberg A, Rosenqvist G, Tiger M, Lundberg J, Varrone A, Farde L (2014) Distinct regional age effects on [11C]AZ10419369 binding to 5-HT1B receptors in the human brain. Neuroimage 103:303–308. CrossRef

Olesen OV, Sibomana M, Keller SH, Andersen F, Jensen J, Holm S, Svarer C, Højgaard L (2009) Spatial resolution of the HRRT PET scanner using 3D-OSEM PSF reconstruction. IEEE Nucl Sci Symp Conf Rec 2009:3789–3790.

Parker C a., Gunn RN, Rabiner E a., Slifstein M, Comley R, Salinas C, Johnson CN, Jakobsen S, Houle S, Laruelle M, Cunningham VJ, Martarello L (2012) Radiosynthesis and characterization of 11C-GSK215083 as a PET radioligand for the 5-HT6 receptor. J Nucl Med 53:295–303. CrossRef

Parker CA, Rabiner EA, Gunn R, Searle G, Martarello L, Comley R, Davy M, Wilson AA, Houle S, Mizrahi R, Laruelle M, Cunningham VJ (2015) Human kinetic modelling of the 5-HT6 PET radioligand, 11C-GSK215083, and its utility for determining occupancy at both 5HT6 and

5HT2A receptors by SB742457 as a potential therapeutic mechanism of action in Alzheimer's disease. J Nucl Med 56:1901–1909. CrossRef

Paterson L, Kornum B (2013) 5-HT radioligands for human brain imaging with PET and SPECT. Med Res Rev 33:54–111. CrossRef

Paterson LM, Tyacke RJ, Nutt DJ, Knudsen GM (2010) Measuring endogenous 5-HT release by emission tomography: promises and pitfalls. J Cereb Blood Flow Metab 30:1682–1706. CrossRef

Portas CM, Bjorvatn B, Ursin R (2000) Serotonin and the sleep/wake cycle: special emphasis on microdialysis studies. Prog Neurobiol 60:12–35.

Postelnicu G, Zollei L, Fischl B (2009) Combined volumetric and surface registration. Med Imaging IEEE Trans 28:508–522. CrossRef

Raote I, Bhattacharyya S, Panicker MM (2013) Functional selectivity in serotonin receptor 2A (5-HT2A) endocytosis, recycling, and phosphorylation. Mol Pharmacol 83:42–50. CrossRef

Rizzo G, Veronese M, Heckemann RA, Selvaraj S, Howes OD, Hammers A, Turkheimer FE, Bertoldo A (2014) The predictive power of brain mRNA mappings for in vivo protein density: a positron emission tomography correlation study. J Cereb Blood Flow Metab 34:827–835. CrossRef

Savli M, Bauer A, Mitterhauser M, Ding Y (2012) Normative database of the serotonergic system in healthy subjects using multi-tracer PET. Neuroimage 63:447–459. CrossRef

Sureau FC, Reader AJ, Comtat C, Leroy C, Ribeiro M-J, Buvat I, Trébossen R (2008) Impact of image-space resolution modeling for studies with the high-resolution research tomograph. J Nucl Med 49:1000–1008. CrossRef

Talairach J, Tournoux P (1988) Co-planar stereotaxic atlas of the human brain: 3-dimensional proportional system: an approach to cerebral imaging. Available online at https://www.researchgate.net/publication/283617540_ Co-Planar_Stereotaxic_Atlas_of_the_Human_Brain3-Dimensional_Pro portional_System_An_Approach_to_Cerebral_Imaging. Accessed November 28, 2016.

Tzourio-Mazoyer N, Landeau B, Papathanassiou D, Crivello F, Etard O, Delcroix N, Mazoyer B, Joliot M (2002) Automated anatomical labeling of activations in SPM using a macroscopic anatomical parcellation of the MNI MRI single-subject brain. Neuroimage 15:273–289. CrossRef

Varnäs K, Halldin C, Hall H (2004) Autoradiographic distribution of serotonin transporters and receptor subtypes in human brain. Hum Brain Mapp 22:246–260. CrossRef

Varnäs K, Hurd YL, Hall H (2005) Regional expression of 5-HT1B receptor mRNA in the human brain. Synapse 56:21–28. CrossRef

Vogel C, Abreu R de S, Ko D, Le S-YY, Shapiro BA, Burns SC, Sandhu D, Boutz DR, Marcotte EM, Penalva LO (2010) Sequence signatures and mRNA concentration can explain two-thirds of protein abundance variation in a human cell line TL-6. Mol Syst Biol 6:400.

Waldinger MD (2015) Psychiatric disorders and sexual dysfunction. Handb Clin Neurol 130:469–489. CrossRef Medline

Woods RP, Cherry SR, Mazziotta JC (1992) Rapid automated algorithm for aligning and reslicing PET images. J Comput Assist Tomogr 16:620–633. CrossRef

Young S, Leyton M (2002) The role of serotonin in human mood and social interaction: insight from altered tryptophan levels. Pharmacol Biochem Behav 71:857–865. CrossRef

Zhou FC, Tao-Cheng JH, Segu L, Patel T, Wang Y (1998) Serotonin transporters are located on the axons beyond the synaptic junctions: anatomical and functional evidence. Brain Res 805:241–254. CrossRef

Sparse Probabilistic Parallel Factor Analysis for the Modeling of PET and Task-fMRI Data

Vincent Beliveau[1,2(✉)], Georgios Papoutsakis[3], Jesper Løve Hinrich[3], and Morten Mørup[3]

[1] Faculty of Health and Medical Sciences, University of Copenhagen, Copenhagen, Denmark
[2] Neurobiology Research Unit, Rigshospitalet, Copenhagen, Denmark
`vincent.beliveau@nru.dk`
[3] DTU Compute, Technical University of Denmark, Copenhagen, Denmark

Abstract. Modern datasets are often multiway in nature and can contain patterns common to a mode of the data (e.g. space, time, and subjects). Multiway decomposition such as parallel factor analysis (PARAFAC) take into account the intrinsic structure of the data, and sparse versions of these methods improve interpretability of the results. Here we propose a variational Bayesian parallel factor analysis (VB-PARAFAC) model and an extension with sparse priors (SP-PARAFAC). Notably, our formulation admits time and subject specific noise modeling as well as subject specific offsets (i.e., mean values). We confirmed the validity of the models through simulation and performed exploratory analysis of positron emission tomography (PET) and functional magnetic resonance imaging (fMRI) data. Although more constrained, the proposed models performed similarly to more flexible models in approximating the PET data, which supports its robustness against noise. For fMRI, both models correctly identified task-related components, but were not able to segregate overlapping activations.

1 Introduction

One of the most widely used tool for dimensionality reduction of large datasets is the Principal Component Analysis (PCA) [1], as well as its probabilistic formulation (PPCA) [2]. PCA finds orthogonal components describing the directions of maximum variance. Selecting the number of components to retain can be problematic and usually requires a post-processing step if the number is not known beforehand. Furthermore, even components explaining a large portion of the variance can include small, non-informative weights making them difficult to interpret. Sparse versions of the PCA algorithms deal with these issues by pruning whole components or individual weights [3].

Neuroscience data are multi-modal in nature and although PCA can be performed on data concatenated along one mode (e.g. time) to identify (e.g. spatial) components common to another mode (e.g. subjects), this approach discards

---

mode-specific information (e.g. subject specific scaling). Instead using a multiway decomposition method, such as Parallel Factor Analysis (PARAFAC) also called Canonical Decomposition or Canonical Polyadic Decomposition (CP) [4–6], maintains the intrinsic structure of the data while having substantially less degrees of freedom and thereby being less sensitive to noise, given model assumptions are met. Furthermore, the PARAFAC model is unique (up to scaling and permutation) under mild conditions [7] providing a more interpretable representation, as components cannot be arbitrarily rotated. Exploiting these properties, the PARAFAC model has successfully been applied to the modeling of neuroimaging data such as EEG and fMRI (for reviews see also [8–10]). Similar to PCA, the amount of small non-informative weights can minimized by inducing sparsity on individual weights. A sparse PARAFAC based on least-squares optimization was discussed in [11].

Sparse multiway models have a high relevance in fields such as neuroscience. The brain has been demonstrated to be organized in networks, and for some specific tasks, e.g. motor tasks, distinct regions of the brain are active, hence a spatially sparse pattern can be expected. When this type of task is performed across multiple subjects it is possible to leverage the intrinsic structure of the data by performing multiway decomposition.

In this paper, we develop a fully bayesian sparse probabilistic PARAFAC (SP-PARAFAC) model with time-dependent and subject specific isotropic noise. We show how a simple change to the sparsity prior allows for easy transition between SP-PARAFAC and probabilistic PARAFAC (VB-PARAFAC). Approximate solution are given based on variational Bayesian inference [12] and we investigate the applicability of the models to PET and task-based fMRI data. While probabilistic PARAFAC has previously been investigated (cf. [13–16]) none impose sparsity on individual elements nor model time-dependent noise.

2 Review of Probabilistic PCA

The initial formulation of probabilistic PCA [2] defines a model relating observations $\boldsymbol{x}$ to latent variables $\boldsymbol{z}$ projected on a K dimensional hyperplane $\boldsymbol{W}$ of origin $\boldsymbol{m}$ with additive Gaussian noise $\boldsymbol{\epsilon}$, such that $\boldsymbol{x} = \boldsymbol{W}\boldsymbol{z} + \boldsymbol{m} + \boldsymbol{\epsilon}$. Here, the latent variable and the noise are assumed to follow an isotropic Gaussian: $\boldsymbol{z} \sim \mathcal{N}(0, \boldsymbol{I})$ and $\boldsymbol{\epsilon} \sim \mathcal{N}(0, \tau^{-1}\boldsymbol{I})$, where τ is the precision of the noise.

In subsequent work [17], the authors formulated a fully Bayesian treatment of PCA solved through variational inference (VB-PCA) and with hierarchical ARD priors $P(\boldsymbol{W}|\boldsymbol{\alpha})$ over the columns of the matrix $\boldsymbol{W}$, allowing for automatic selection of the number of components. Here $P(\boldsymbol{W}|\boldsymbol{\alpha})$ was defined to follow a multivariate Gaussian specific to each column where $\boldsymbol{\alpha}$ is defined as the precision:

$$P(\boldsymbol{W}|\boldsymbol{\alpha}) = \prod_k^K \left(\frac{\alpha_k}{2\pi}\right)^{\frac{T}{2}} \exp\left\{-\frac{1}{2}\alpha_k\|\boldsymbol{w}_k\|^2\right\} \quad (1)$$

$$P(\boldsymbol{\alpha}) = \prod_k^K \Gamma(\alpha_k|a_{\alpha_k}, b_{\alpha_k}) \quad (2)$$

where $\boldsymbol{w}_k$ is the k_{th} column of $\boldsymbol{W}$. To complete the Bayesian specification, the remaining parameters are associated with broad priors: $\boldsymbol{m} \sim \mathcal{N}(0, \beta^{-1}\boldsymbol{I})$ and $\tau \sim \Gamma(a_\tau, b_\tau)$.

The investigation of alternative priors on $\boldsymbol{W}$ by [3] lead to the a fully sparse formulation of PCA (SP-PCA) where a sparsity inducing prior is imposed on elements of $\boldsymbol{W}$ rather than columns. In theory this allows the model to identify both the model order (true K) and disregard noisy or irrelevant voxels (features). Among the different priors studied, Jeffrey's prior was shown to give sparse components with the highest cumulative explained variance. With Jeffrey's prior, the conditional distribution of $P(\boldsymbol{W}|\boldsymbol{\alpha})$ and the prior on $\boldsymbol{\alpha}$ becomes:

$$P(w_{v,k}|\alpha_{v,k}) = \left(\frac{\alpha_{v,k}}{2\pi}\right)^{1/2} \exp\left\{-\frac{1}{2}\alpha_{v,k}w_{v,k}^2\right\} \quad (3)$$

$$Jeffrey's(\alpha_{v,k}) \sim \sqrt{E_{P(w_{v,k}|\alpha_{v,k})}\left(\left(\frac{\partial}{\partial\alpha}\ln P(w_{v,k}|\alpha_{v,k})\right)^2\right)} = \frac{1}{\alpha_{v,k}} \quad (4)$$

3   Probabilistic Parallel Factor Analysis

Multiway data can be viewed as a tensor structure. In this paper we are considering 3-way tensors of dimension $V \times T \times S$, where for ease of correspondence with the PET and fMRI datasets V will be referred to as voxels, T as time and S as subjects. Similar to PCA, the PARAFAC model seeks to identify a matrix $\boldsymbol{W}$ of size $V \times K$, for which the columns are common components across the S subjects. In contrast to PCA the PARAFAC model allows for individual scaling of the components, which can be used to characterize inter-subject variability and it also accounts for subject specific temporal noise. A graphical model of the proposed model is illustrated in Fig. 1. Each timepoint t for each subject s is reconstructed by,

$$\boldsymbol{x}_t^{(s)} = \boldsymbol{W}\,\mathrm{diag}(\boldsymbol{\delta}^{(s)})\boldsymbol{z}_t + \boldsymbol{m}^{(s)} + \boldsymbol{\epsilon}_t^{(s)} \quad (5)$$

where $\boldsymbol{W}$ and $\boldsymbol{z}$ are now common across subjects, but where we model time dependent noise specific to each subject $\boldsymbol{\epsilon}_t^{(s)}$ (with precision $\tau_t^{(s)}$), subject specific mean $\boldsymbol{m}^{(s)}$ and subject specific scaling of the components $\boldsymbol{\delta}^{(s)}$. Note that here $\boldsymbol{\epsilon}$, $\boldsymbol{m}$, $\boldsymbol{\delta}$ and $\boldsymbol{\tau}$ are matrices and $\cdot^{(s)}$ denotes the sth column. The likelihood of a model with a given set of parameters is assess by,

$$P(\boldsymbol{X}\,|\,\boldsymbol{W}, \boldsymbol{Z}, \boldsymbol{m}, \boldsymbol{\tau}, \boldsymbol{\delta}) = \prod_s^S \prod_t^T \mathcal{N}\left(\boldsymbol{x}_t^{(s)}|\boldsymbol{W}\,\mathrm{diag}(\boldsymbol{\delta}^{(s)})\boldsymbol{z}_t + \boldsymbol{m}^{(s)}, \tau_t^{(s)^{-1}}\boldsymbol{I}_V\right) \quad (6)$$
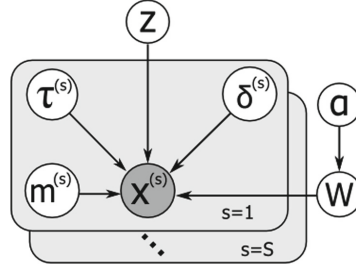
Fig. 1. Graphical model for probabilistic PARAFAC.

To complete the Bayesian framework, prior distributions are defined for the parameters:

$$P(\boldsymbol{\delta}) = \prod_s^S \mathcal{N}\left(\boldsymbol{\delta}^{(s)}|\mathbf{0}, \boldsymbol{I}_K\right) \tag{7}$$

$$P(\boldsymbol{\tau}) = \prod_s^S \prod_t^T \Gamma\left(\tau_t^{(s)}|a_{\tau_t^{(s)}}, b_{\tau_t^{(s)}}\right) \tag{8}$$

$$P(\boldsymbol{m}) = \prod_s^S \mathcal{N}\left(\boldsymbol{m}^{(s)}|\mathbf{0}, \beta^{-1}\boldsymbol{I}_V\right) \tag{9}$$

$$P(\boldsymbol{Z}) = \prod_t^T \mathcal{N}\left(\boldsymbol{z}_t|\mathbf{0}, \boldsymbol{I}_K\right) \tag{10}$$

The choice of priors for $\boldsymbol{W}$ and $\boldsymbol{\alpha}$ determines the pruning and sparsity capability of the model. If the priors are chosen to be Eqs. (1) and (2) then VB-PARAFAC is obtained. Which seeks to identify active and inactive components using ARD. However, if the priors are chosen to be Eqs. (3) and (4) then Sparse Probabilistic (SP-)PARAFAC is obtained. Seeking to identify both dimensionality (model order) and active voxels (features).

The general complexity of the VB- and SP-PCA and the proposed VB- and SP-PARAFAC models differ. Notably, the PCA models with temporally concatenated data have $KT(S-1)$ more degrees of freedom for the latent variable $\boldsymbol{z}$ compared to the PARAFAC models, which for a dataset with large T and K could be a potential source of overfitting, whereas PARAFAC have KS more parameters for $\boldsymbol{\delta}$ and $V(S-1)$ more parameters for $\boldsymbol{m}$.

4   Variational Inference

In order to maximize the likelihood function the marginal distribution $P(\boldsymbol{X}) = \int P(\boldsymbol{X}, \theta)d\theta$ must be estimated. However, the marginalization of this distribution with respect to the prior distributions is most often analytically intractable.

Variational inference solves this problem by approximating the desired distribution with another distribution Q, called the variational distribution. The challenge in a variational approach is to choose a sufficiently simple distribution Q so that the log marginal likelihood can be approximated by a tractable lower bound $\mathcal{L}(Q)$ and at the same time is sufficiently flexible in order to make this bound tight. A common choice for Q is a distribution which factorizes over the model parameters such that $Q = \prod_i Q_i(\theta_i)$. For the VB-PARAFAC model, the distribution $Q_i(\theta_i)$ were defined as follow:

$$Q(\boldsymbol{Z}) = \prod_t^T \mathcal{N}(\boldsymbol{\mu}_{\boldsymbol{z}_t}, \boldsymbol{\Sigma}_{\boldsymbol{z}_t}) \tag{11}$$

$$Q(\boldsymbol{W}) = \prod_v^V \mathcal{N}(\boldsymbol{w}_v | \boldsymbol{\mu}_{\boldsymbol{w}_v}, \boldsymbol{\Sigma}_{\boldsymbol{w}_v}) \tag{12}$$

$$Q(\boldsymbol{\alpha}) = \prod_k^K \Gamma(\alpha_k | \tilde{a}_{\alpha_k}, \tilde{b}_{\alpha_k}) \tag{13}$$

$$Q(\boldsymbol{\delta}) = \prod_s^S \mathcal{N}(\boldsymbol{\delta}^{(s)} | \boldsymbol{\mu}_{\delta^{(s)}}, \boldsymbol{\Sigma}_{\boldsymbol{\delta}^{(s)}}) \tag{14}$$

$$Q(\boldsymbol{m}) = \prod_s^S \mathcal{N}(\boldsymbol{m}^{(s)} | \boldsymbol{\mu}_{\boldsymbol{m}^{(s)}}, \boldsymbol{\Sigma}_{\boldsymbol{m}^{(s)}}) \tag{15}$$

$$Q(\boldsymbol{\tau}) = \prod_s^S \prod_t^T \Gamma(\tau_t^{(s)} | \tilde{a}_{\tau_t^{(s)}}, \tilde{s}_{\tau_t^{(s)}}) \tag{16}$$

It can be shown that the log marginal probability is equivalent to $\ln P(X) = \mathcal{L}(Q) + KL(Q||P)$, where KL is the Kullback-Leibler divergence. By fixing Q_j and maximizing $\mathcal{L}(Q)$ with respect to the remaining $Q_{i \neq j}$ we obtain the general expression $\ln Q_j^* = \mathbb{E}_{i \neq j}[\ln p(\boldsymbol{X}, \boldsymbol{\theta})] + const$ which minimizes the KL divergence. By applying and normalizing this, the update rules for Q can be derived and are shown in Eqs. 17 – 27. Note that $\boldsymbol{w}_v$ denotes a row of $\boldsymbol{W}$, $\langle \cdot \rangle$ denotes the expectation and that the operator $\bullet$ is the Hadamard product.

$$\boldsymbol{\mu}_{\boldsymbol{\delta}^{(s)}} = \boldsymbol{\Sigma}_{\delta^{(s)}} \sum_t^T \left\langle \tau_t^{(s)} \right\rangle \langle \mathrm{diag}(\boldsymbol{z}_t) \rangle \left\langle \boldsymbol{W}^T \right\rangle (\boldsymbol{x}_t^{(s)} - \left\langle \boldsymbol{m}^{(s)} \right\rangle) \tag{17}$$

$$\boldsymbol{\Sigma}_{\boldsymbol{\delta}^{(s)}} = \left(\boldsymbol{I}_K + \sum_t^T \left\langle \tau_t^{(s)} \right\rangle \left\langle \boldsymbol{z}_t \boldsymbol{z}_t^T \right\rangle \bullet \left\langle \boldsymbol{W}^T \boldsymbol{W} \right\rangle \right)^{-1} \tag{18}$$

$$\boldsymbol{\mu}_{\boldsymbol{z}_t} = \boldsymbol{\Sigma}_{\boldsymbol{z}_t} \sum_s^S \left\langle \tau_t^{(s)} \right\rangle \mathrm{diag}\left(\left\langle \boldsymbol{\delta}^{(s)} \right\rangle \right) \left\langle \boldsymbol{W}^T \right\rangle \left(\boldsymbol{x}_t^{(s)} - \left\langle \boldsymbol{m}^{(s)} \right\rangle \right) \tag{19}$$

$$\boldsymbol{\Sigma}_{\boldsymbol{z}_t} = \left(\boldsymbol{I}_K + \sum_s^S \left\langle \tau_t^{(s)} \right\rangle \left\langle \boldsymbol{\delta}^{(s)} \boldsymbol{\delta}^{(s)T} \right\rangle \bullet \left\langle \boldsymbol{W}^T \boldsymbol{W} \right\rangle \right)^{-1} \tag{20}$$

$$\boldsymbol{\mu}_{\boldsymbol{m}^{(s)}} = \boldsymbol{\Sigma}_{\boldsymbol{m}^{(s)}} \sum_t^T \left\langle \tau_t^{(s)} \right\rangle \left(\boldsymbol{x}_t^{(s)} - \langle \boldsymbol{W} \rangle \left\langle diag(\boldsymbol{\delta}^{(s)}) \right\rangle \langle \boldsymbol{z}_t \rangle \right) \tag{21}$$

$$\boldsymbol{\Sigma}_{\boldsymbol{m}^{(s)}} = \left(\beta + \sum_t^T \langle \tau \rangle_t^{(s)} \right)^{-1} \boldsymbol{I}_K \tag{22}$$

$$\boldsymbol{\mu}_{\boldsymbol{w}_v} = \boldsymbol{\Sigma}_{\boldsymbol{w}_v} \sum_s^S \sum_t^T \left\langle diag(\boldsymbol{\delta}^{(s)}) \right\rangle \langle \boldsymbol{z}_t \rangle \left\langle \tau_t^{(s)} \right\rangle \left(\boldsymbol{x}_t^{(s)T} - \left\langle \boldsymbol{m}^{(s)T} \right\rangle \right)_v \tag{23}$$

$$\boldsymbol{\Sigma}_{\boldsymbol{w}_v} = \left(diag(\boldsymbol{\alpha}) + \sum_s^S \sum_t^T \left\langle \tau_t^{(s)} \right\rangle \left\langle \boldsymbol{\delta}^{(s)} \boldsymbol{\delta}^{(s)T} \right\rangle \bullet \left\langle \boldsymbol{z}_t \boldsymbol{z}_t^T \right\rangle \right)^{-1} \tag{24}$$

$$\tilde{a}_\alpha = a_\alpha + \frac{V}{2}, \quad \tilde{b}_{\alpha_k} = b_{\alpha_k} + \frac{\left\langle \boldsymbol{w}_k^T \boldsymbol{w}_k \right\rangle}{2} \tag{25}$$

$$\tilde{a}_{\boldsymbol{\tau}^{(s)}} = a_{\boldsymbol{\tau}^{(s)}} + \frac{V}{2} \tag{26}$$

$$\begin{aligned}
\tilde{b}_{\tau_t^{(s)}} = {} & b_{\tau_t^{(s)}} + \frac{1}{2} \| \boldsymbol{x}_t^{(s)} \|^2 + \frac{1}{2} \left\langle \| \boldsymbol{m}^{(s)} \|^2 \right\rangle - \boldsymbol{x}_t^{(s)T} \left\langle \boldsymbol{m}^{(s)} \right\rangle \\
& - \boldsymbol{x}_t^{(s)T} \langle \boldsymbol{W} \rangle \left\langle diag(\boldsymbol{\delta}^{(s)}) \right\rangle \langle \boldsymbol{z}_t \rangle \\
& + \frac{1}{2} Tr \left(\left\langle \boldsymbol{W}^T \boldsymbol{W} \right\rangle \bullet \left\langle \boldsymbol{\delta}^{(s)} \boldsymbol{\delta}^{(s)T} \right\rangle \left\langle \boldsymbol{z}_t \boldsymbol{z}_t^T \right\rangle \right) \\
& + \left\langle \boldsymbol{m}^{(s)T} \right\rangle \langle \boldsymbol{W} \rangle \left\langle diag(\boldsymbol{\delta}^{(s)}) \right\rangle \langle \boldsymbol{z}_t \rangle
\end{aligned} \tag{27}$$

By changing the prior on $\boldsymbol{W}$ to Jeffrey's prior shown in Eq. 4 we obtain the solution for SP-PARAFAC. The Q_i distributions remain the same except for $Q(\boldsymbol{\alpha})$ which now factorizes over elements, i.e. $Q(\boldsymbol{\alpha}) = \prod_v^V \prod_k^K \Gamma(\alpha_{v,k} | \tilde{a}_{\alpha_{v,k}}, \tilde{b}_{\alpha_{v,k}})$. These changes are reflected in the update rules for $\boldsymbol{W}$ and $\boldsymbol{\alpha}$,

$$\boldsymbol{\Sigma}_{\boldsymbol{w}_v} = \left(\sum_s^S \sum_t^T \left\langle \tau_t^{(s)} \right\rangle \left\langle \boldsymbol{\delta}^{(s)} \boldsymbol{\delta}^{(s)T} \right\rangle \bullet \left\langle \boldsymbol{z}_t \boldsymbol{z}_t^T \right\rangle + diag(\langle \alpha_{v,.} \rangle) \right)^{-1} \tag{28}$$

$$\tilde{a}_{\alpha_{v,k}} = \frac{1}{2}, \quad \tilde{b}_{\alpha_{v,k}} = \frac{\left\langle w_{v,k}^2 \right\rangle}{2} \tag{29}$$

The lower bound $\mathcal{L}(Q)$ can be easily derived to monitor the convergence of the algorithm. Although convergence is guaranteed, the solution will not necessarily arrive at a global maximum. This is typically addressed by running the algorithm multiple times and keeping the solution with the largest lower bound.

5   Results

In this section, we present a validation of our model with simulation and perform the analysis of PET and fMRI data. The parameters β^{-1}, a_α, b_α, a_τ and b_τ were set to 10^{-3} to obtain broad priors. In all cases, $\boldsymbol{W}$ was initialized using PCA, which in practice consistently lead to a higher lower bound compared to random initialization and mitigated the need for multiple restarts in the case of VB- and SP-PCA. For VB- and SP-PARAFAC, PCA was performed on the data from individual subjects, hence the algorithm was restarted for each subject and the solution with the highest lower bound was kept. To assess stability of the solution across model initializations the RV coefficient [18] between the estimated $\boldsymbol{W}$ for two different initializations was calculated. This was done for all unique pairwise combinations, $(\#repeats-1)!$, and the average RV coefficient is reported. The RV coefficient is a multivariate generalization of the Pearson correlation coefficient which measure subspace overlap and is invariant to rotation and translation. The RV coefficient is one if the subspaces overlap completely and zero if they have no overlap. Similarly, we also computed an average correlation: first, for each pair of estimated $\boldsymbol{W}$, components were matched based on correlation and an average correlation computed. Then, the average of all unique pairs was computed.

Results were also compared to solutions obtained with the PARAFAC function from the N-way toolbox 3.21 [19], which evaluates the standard PARAFAC model without modeling of the mean or the noise. As PARAFAC does not model the mean, the data was centered when using this algorithm. Due to memory limitation, the PCA initialization for N-way PARAFAC did not work for large datasets, hence we used the default initialization as it consistently resulted in lower reconstruction error compared to random initialization. Furthermore, the number of components was determined by performing the decomposition for a range of varying number of components and keeping the solution with the most components and a core-consistency of a 100.

5.1   Simulation

This section presents a comparison between VB-PCA [17], SP-PCA [3], PARAFAC [20] and the proposed VB-PARAFAC and SP-PARAFAC through simulation. We created a 3-way dataset using the following procedure. Three sparse vectors of length $V = 10$ were created and concatenated to form matrix $\boldsymbol{W}$; this is shown in Fig. 2 as ground truth. Then random latent variables $\boldsymbol{z}_t$ of length $T = 100$, random mean values $\boldsymbol{m}^{(s)}$ and random scaling factors $\boldsymbol{\delta}^{(s)}$ for $S = 5$ subjects were sampled from the distribution $\mathcal{N}(\boldsymbol{0}, \boldsymbol{I})$ and linearly mixed according to Eq. 5. The additive noise was sampled from $\mathcal{N}(\boldsymbol{0}, \boldsymbol{\tau}_t^{(s)} \boldsymbol{I})$, with the precision $\boldsymbol{\tau}_t^{(s)}$ sampled from $\Gamma(1,1)$. The resulting data was concatenated along the time dimension for the PCA algorithms and as a 3-way tensor for the PARAFAC models.

Figure 2 shows the components identified by the algorithms. All models identified the ground truth components to varying degrees of accuracy and pruned
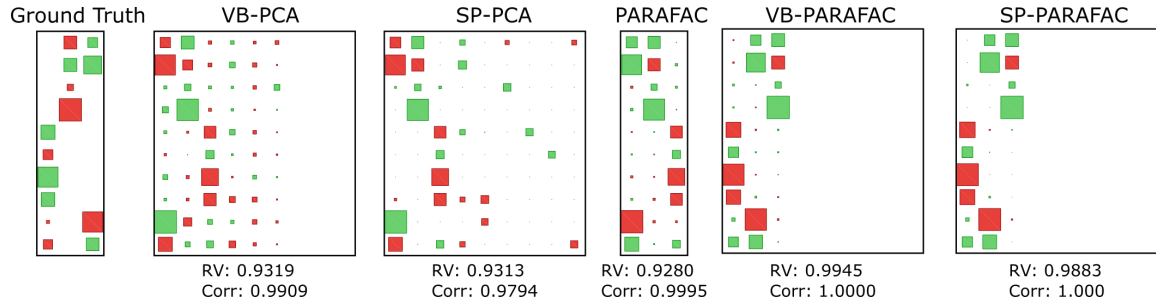
Fig. 2. Hinton diagram of W identified by the algorithms (green is positive and red is negative). Average RV and Pearson's correlation coefficients between the ground truth W and the identified solutions are reported. (Color figure online)

non-informative components. Both PCA models were more confounded by noise and their inability to account for subject specific means compared to their PARAFAC counter parts. Furthermore, SP-PCA and SP-PARAFAC performed better than their VB version at pruning individual non-related weights, although this is not reflected by the RV coefficient. These results indicate that the VB- and SP-PARAFAC models benefit by having PARAFAC structure and by modeling time and subject varying noise as well as subject specific means when these effects are present in the data and that fully sparse priors are more efficient at identifying sparsity structure from the data compared to priors inducing sparsity on whole components.

5.2   Positron Emission Tomography

Here we performed an exploratory data decomposition of PET data. The synchronized nature of PET experiments, the time-depend noise associated with the radioactive isotope decay and subject specific scaling of the time-activity curves (TAC) due to variation in injected dose and body weight make multiway model in theory well suited for the analysis of PET data.

The PET data for the radioligand [11C]CUMI-101 and matching T1-weighted structural magnetic resonance images (MRI) were obtained from the Cimbi database [21] for 4 healthy subjects. Dynamic PET images (34 frames; $2 \times 5\,\mathrm{s}$, $10 \times 15\,\mathrm{s}$, $4 \times 30\,\mathrm{s}$, $5 \times 120\,\mathrm{s}$, $5 \times 300\,\mathrm{s}$, $8 \times 600\,\mathrm{s}$) were acquired on a HRRT scanner with approximate in-plane resolution of $2\,\mathrm{mm}$ and the structural images were acquired on a 3T Siemens Trio scanner at $1\,\mathrm{mm}$ isotropic resolution. The structural images were processed within FreeSurfer [22]. PET images were coregistered to the structural MRI [23], transferred to a common space (MNI152) and smoothed using a $5\,\mathrm{mm}$ FWHM 3d Gaussian kernel. The data was finally concatenated along subjects, forming a 3-way tensor, and processed with VB-PARAFAC and SP-PARAFAC with an initial dimensionality of 30.

VB-PCA, VB-PARAFAC and SP-PARAFAC identified 7, 24 and 19 non-null components, respectively; SP-PCA did not prune any component. Only two components were commonly identified by all five methods. The first one loaded on all brain space (Fig. 3A), whereas the second loaded on regions of high and
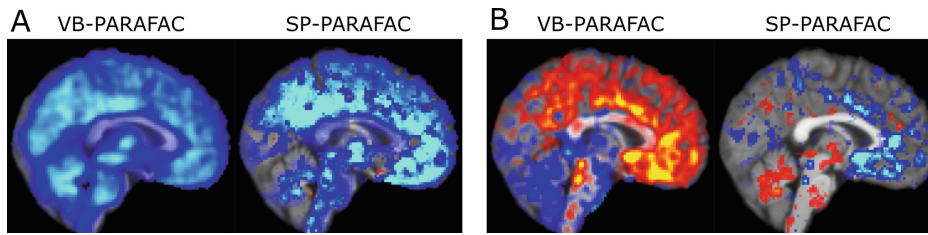
Fig. 3. All algorithms identified at least two similar components, one weighted over the whole brain (A) and one distributed over high and low binding regions (B). Corresponding components for VB-PCA, SP-PCA and PARAFAC are not shown, but exhibited similar patterns. All other components displayed random patterns with no underlying anatomical correspondence. The average RV and Pearson's correlation coefficients for VB- and SP-PARAFAC were (0.5302, 0.5655) and (0.2635, 0.2752).

low binding regions with corresponding weights (Fig. 3B). The others exhibited random patterns across the whole brain and adjusted for small, random variation in the data. There was no component which loaded uniquely on specific brain regions indicating that a set of basis function common to all brain voxel is the more appropriate model. This results is reasonable as the kinetic across all brain voxels is highly similar compared to other modalities, e.g. fMRI. Consequently, although both VB- and SP-PARAFAC algorithms pruned non-informative components, the SP-PARAFAC model introduced seemingly random spatial sparsity which left the components difficult to interpret. Although sparsity is often a desired property, this result indicate that a fully sparse model may not always be appropriate for the identification of global patterns.
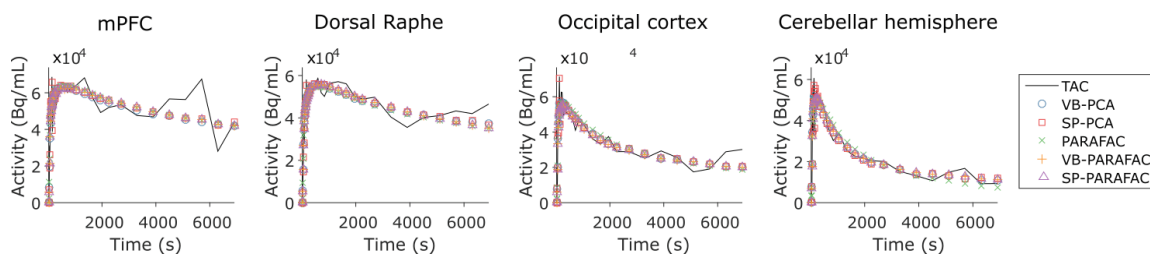

Fig. 4. TACs from individual voxels of selected brain regions and their approximation.

Another interesting application of data decomposition methods applied to PET imaging is the denoising of the data. We compared the approximation performed by the different algorithms and the results were surprisingly similar for all brain regions (see Fig. 4). These results indicate that our constrained PARAFAC models is able to identify noise structure comparable to what a more flexible model like VB and SP-PCA can discover and performed similarly well in approximating the underlying data.

5.3 Functional MRI

The analysis of multiway fMRI data is routinely performed using independent component analysis (ICA) [24]. One of the most common model used to perform ICA decomposition of fMRI data is the probabilistic ICA (PICA) [25] and its tensorial extension for multi-subject analysis. We here aim to demonstrate a side-by-side comparison of the components identified by tensor PICA and the other five methods.

Eight healthy right-handed subjects performed a visually cued reaction fist-closure fMRI task. Subjects performed 10 blocks of a duration of 10 sec, interleaved with 10 sec rest, were they were instructed with a visual cue to open and close their right or left hand at a frequency of approximately $1\,\mathrm{Hz}$; the pattern of left and right blocks was random but fixed across subjects. This task leads to significant activation of the visual, motor and premotor cortex on the contralateral side of the movement, and relatively weaker activation on the ipsilateral side. For each subject, 210 axial echo-planar volumes (TE $= 30$ ms, TR $= 2.25$ s, $64 \times 64 \times 32$ voxels at $3.6 \times 3.6 \times 3.8$ mm) were acquired on a 3-T Siemens Prisma together with a T1-weighted anatomical image at $1\,\mathrm{mm}$ isotropic resolution. The fMRI was motion corrected (MCFLIRT [26]), coregistered to the structural image using (FLIRT [26]), transformed to common MNI152 space (FNIRT [20]) and finally smoothed using a $8\,\mathrm{mm}$ FWHM 3d Gaussian kernel. The fMRI data was finally processed using tensor PICA in Melodic [25] and the five methods. VB-PARAFAC and SP-PARAFAC had an initial dimensionality of 50. Significance maps were estimated as in [25] by creating Z-scores maps by dividing each components by the residual voxel variance and modeling the associated histograms using a Gaussian/Gamma mixture modeling approach in Melodic.

For PICA, the estimated dimensionality was 47. No component was completely pruned by VB-PARAFAC, whereas SP-PARAFAC identified only 4 components. The components identified by all the models corresponding to motor or visual activation are presented in Fig. 5. The different functional aspect of the task are clearly segregated in the components identified by PICA; component 1 is has strong visual activation (but also contains weaker motor activation), where as components 2 and 3 have strong motor activation corresponding to left and right fist-closure, respectively. For the other methods, all relevant components contained both motor and visual activation, however the significance was relatively lower. This is surprising as we would have expected that by enforcing spatial sparsity and modeling time-dependent noise, which is particularly problematic in fMRI (e.g. physiological artifacts, motion), the identifiability of the signal would have improved. As the activation of the visual and motor areas are synchronized in this task, the visual and motor cortex exhibit similar, but non identical, temporal profile which may be difficult to isolate given our model assumptions. Furthermore, this task also illicits both contralateral and (weaker) ipsilateral activation of the motor and premotor cortex, hence left and right hand squeeze will have overlapping activation which may be difficult to segregate in a sparse model. The SP-PCA and the PARAFAC model clearly underperformed in
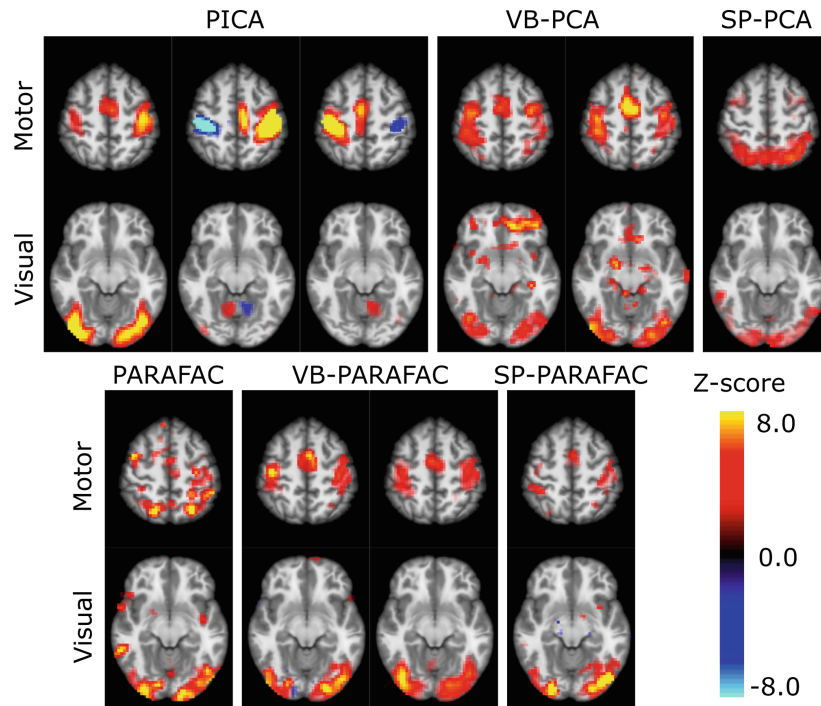
Fig. 5. Motor and visual components (columns) identified by the six methods. The axial slice for the motor and visual views correspond respectively to Z = 55.75 mm and Z = −10.50 mm in MNI152 space. The average RV and Pearson's correlation coefficients for VB- and SP-PARAFAC were (0.9130, 0.6815) and (0.5633, 0.5965).

identifying the motor and visual components. Interestingly, the SP-PARAFAC model was able to prune most of the non task-related components and established a model dimensionality much closer to what is expected from the task compared to the other models.

6   Summary

In this work we presented a VB-PARAFAC model with time-dependent modeling of the noise and a fully sparse extension, the SP-PARAFAC model. We validated these models and compared them to VB-PCA, SP-PCA and PARAFAC through simulation and applied them to PET and task-based fMRI data. For PET, the models identified two common components and performed equally well at approximating the data. The spatial sparsity enforced by SP-PCA and SP-PARAFAC appeared unfortunately random, rendering the components difficult to interpret. We also compared the models to tensor PICA in the identification of task-related fMRI components. Tensor PICA identified functionally segregated motor and visual components where as the other models only identified components with both motor and visual activation and with lower significance. However, the dimensionality of the SP-PARAFAC model was much closer to the what expected given the task, suggesting that this model performs better at pruning non task-related components. Although we solely investigated

neuroimaging modalities in this report, these models have a strong relevance for other types of data for which PARAFAC is commonly used.

References

1. Jolliffe, I.: Principal Component Analysis, vol. 487. Springer, New York (1986)
2. Tipping, M., Bishop, C.: Probabilistic principal component analysis. Royal Stat. Soc. **23**(3), 492–503 (1999)
3. Guan, Y., Dy, J.: Sparse probabilistic principal component analysis. In: International Conference on Artificial Intelligence and Statistics, pp. 185–192 (2009)
4. Harshman, R.: Foundations of the parafac procedure: models and conditions for an "explanatory" multi-modal factor analysis. (1970)
5. Carroll, J., Chang, J.: Analysis of individual differences in multidimensional scaling via an n-way generalization of eckart-young decomposition. Psychometrika **35**(3), 283–319 (1970)
6. Hitchcock, F.: The expression of a tensor or a polyadic as a sum of products. J. Math. Phys. **6**(1), 164–189 (1927)
7. Kruskal, J.: Three-way arrays: rank and uniqueness of trilinear decompositions, with application to arithmetic complexity and statistics. Linear Algebra Appl. **18**(2), 95–138 (1977)
8. Kolda, T., Bader, B.: Tensor decompositions and applications. SIAM Rev. **51**(3), 455–500 (2009)
9. Acar, E., Yener, B.: Unsupervised multiway data analysis: a literature survey. IEEE Trans. Knowl. Data Eng. **21**(1), 6–20 (2009)
10. Mørup, M.: Applications of tensor (multiway array) factorizations and decompositions in data mining. Wiley Interdisc. Rev. Data Mining Knowl. Disc. **1**(1), 24–40 (2011)
11. Rasmussen, M., Bro, R.: A tutorial on the lasso approach to sparse modeling. Chemometr. Intell. Lab. Syst. **119**, 21–31 (2012)
12. Attias, H.: A variational bayesian framework for graphical models. Adv. Neural Inform. Process. Syst. **12**(1–2), 209–215 (2000)
13. Nielsen, F.: Variational approach to factor analysis and related models (2004)
14. Ermis, B., Cemgil, A.: A Bayesian tensor factorization model via variational inference for link prediction **3**, 1–9. arXiv preprint arXiv:1409.8276 (2014)
15. Zhao, Q., Zhang, L., Cichocki, A., Hoff, P.: Bayesian CP factorization of incomplete tensors with automatic rank determination **37**(9), 1–15. arXiv preprint arXiv:1401.6497v2 (2015)
16. Guo, W., Yu, W.: Variational Bayesian PARAFAC decomposition for Multidimensional Harmonic Retrieval. In: Proceedings of 2011 IEEE CIE International Conference on Radar, RADAR 2011, vol. 2, pp. 1864–1867 (2011)
17. Bishop, C.: Variational principal components. In: Ninth International Conference on Artificial Neural Networks, ICANN 1999 (Conf. Publ. No. 470), vol. 1, pp. 509–514. IET (1999)
18. Robert, P., Escoufier, Y.: A unifying tool for linear multivariate statistical methods: the RV-coefficient. Appl. Stat. **25**, 257–265 (1976)
19. Andersson, C.A., Bro, R.: The N-way toolbox for MATLAB. Chemometr. Intell. Lab. Syst. **52**(1), 1–4 (2000)
20. Andersson, J., Jenkinson, M., Smith, S.: Non-linear registration aka Spatial normalisation. FMRIB Technial report TR07JA2, p. 22, June 2007

21. Knudsen, G., Jensen, P., Erritzoe, D., Baaré, W., Ettrup, A., Fisher, P., Gillings, N., Hansen, H., Hansen, L., Hasselbalch, S., Henningsson, S., Herth, M., Holst, K., Iversen, P., Kessing, L., Macoveanu, J., Madsen, K., Mortensen, E., Nielsen, F., Paulson, O., Siebner, H., Stenbæk, D., Svarer, C., Jernigan, T., Strother, S., Frokjaer, V.: The center for integrated molecular brain imaging (Cimbi) database. NeuroImage **124**, 1213–1219 (2015)
22. Fischl, B.: FreeSurfer. Neuroimage **62**(2), 774–781 (2012)
23. Greve, D., Fischl, B.: Accurate and robust brain image alignment using boundary-based registration. Neuroimage **48**(1), 63–72 (2009)
24. Calhoun, V., Liu, J., Adali, T.: A review of group ICA for fMRI data and ICA for joint inference of imaging, genetic, and ERP data. NeuroImage **45**(1 Suppl), S163–S172 (2009)
25. Beckmann, C., Smith, S.: Tensorial extensions of independent component analysis for multisubject FMRI analysis. NeuroImage **25**(1), 294–311 (2005)
26. Jenkinson, M., Bannister, P., Brady, M., Smith, S.: Improved optimization for the robust and accurate linear registration and motion correction of brain images. NeuroImage **17**(2), 825–841 (2002)

DECLARATION OF CO-AUTHORSHIP

Information on PhD student:	
Name of PhD student	Vincent Beliveau
E-mail	vincent.beliveau@nru.dk
Date of birth	15-01-1986
Work place	Neurobiology Research Unit, Rigshospitalet
Principal supervisor	Gitte Moos Knudsen

Title of PhD thesis:

Functional and Molecular Imaging of the Serotonin System in the Human Brain

This declaration concerns the following article:

Functional connectivity of the dorsal and median raphe nuclei at rest

The PhD student's contribution to the article: *(please use the scale (A,B,C) below as benchmark*)*	(A,B,C)
1. Formulation/identification of the scientific problem that from theoretical questions need to be clarified. This includes a condensation of the problem to specific scientific questions that is judged to be answerable by experiments	B
2. Planning of the experiments and methodology design, including selection of methods and method development	C
3. Involvement in the experimental work	C
4. Presentation, interpretation and discussion in a journal article format of obtained data	B

*Benchmark scale of the PhD student's contribution to the article		
A. refers to:	Has contributed to the co-operation	0-33 %
B. refers to:	Has contributed considerably to the co-operation	34-66 %
C. refers to:	Has predominantly executed the work independently	67-100 %

Signature of the co-authors:			
Date:	Name:	Title:	Signature:
23/11-17	Claus Svarer	Sen Rese	
23/11-17	Gitte M. Knudsen	Prof.	
24/11-17	Vibe G. Frokjaer	MD, PhD.	
23/11-17	Douglas N. Greve	Asst Prof	DNGreve

23/11-17	Patrick M. Fisher		Senior Researcher	

Signature of the PhD student and the principal supervisor:

| Date: 24/11-17 | Date: 24-11-17 |
| PhD student: | Principal supervisor: |

DECLARATION OF CO-AUTHORSHIP

Information on PhD student:

Name of PhD student	Vincent Beliveau
E-mail	vincent.beliveau@nru.dk
Date of birth	15-01-1986
Work place	Neurobiology Research Unit, Rigshospitalet
Principal supervisor	Gitte Moos Knudsen

Title of PhD thesis:

Functional and Molecular Imaging of the Serotonin System in the Human Brain

This declaration concerns the following article:

A High-Resolution In Vivo Atlas of the Human Brain's Serotonin System

The PhD student's contribution to the article: *(please use the scale (A,B,C) below as benchmark*)*	(A,B,C)
1. Formulation/identification of the scientific problem that from theoretical questions need to be clarified. This includes a condensation of the problem to specific scientific questions that is judged to be answerable by experiments	B
2. Planning of the experiments and methodology design, including selection of methods and method development	C
3. Involvement in the experimental work	C
4. Presentation, interpretation and discussion in a journal article format of obtained data	B

Benchmark scale of the PhD student's contribution to the article		
A. refers to:	Has contributed to the co-operation	0-33 %
B. refers to:	Has contributed considerably to the co-operation	34-66 %
C. refers to:	Has predominantly executed the work independently	67-100 %

Signature of the co-authors:

Date:	Name:	Title:	Signature:
23-11/17	Melanie Ganz	Asst. Prof.	
23-11/17	Ling Feng	Ph.d.	
23/11/17	Brice Ozenne	Dr.	
26/11-17	Liselotte Højgaard	Prof.	

Signature of the PhD student and the principal supervisor:

Date: 24-11-17	Date: 24-11-17
PhD student:	Principal supervisor:

2

DECLARATION OF CO-AUTHORSHIP

Information on PhD student:	
Name of PhD student	Vincent Beliveau
E-mail	vincent.beliveau@nru.dk
Date of birth	15-01-1986
Work place	Neurobiology Research Unit, Rigshospitalet
Principal supervisor	Gitte Moos Knudsen

Title of PhD thesis:
Functional and Molecular Imaging of the Serotonin System in the Human Brain

This declaration concerns the following article:
Sparse Probabilistic Parallel Factor Analysis for the Modeling of PET and Task-fMRI Data

The PhD student's contribution to the article: *(please use the scale (A,B,C) below as benchmark*)*	(A,B,C)
1. Formulation/identification of the scientific problem that from theoretical questions need to be clarified. This includes a condensation of the problem to specific scientific questions that is judged to be answerable by experiments	B
2. Planning of the experiments and methodology design, including selection of methods and method development	C
3. Involvement in the experimental work	C
4. Presentation, interpretation and discussion in a journal article format of obtained data	B

*Benchmark scale of the PhD student's contribution to the article		
A. refers to:	*Has contributed to the co-operation*	*0-33 %*
B. refers to:	*Has contributed considerably to the co-operation*	*34-66 %*
C. refers to:	*Has predominantly executed the work independently*	*67-100 %*

Signature of the co-authors:			
Date:	Name:	Title:	Signature:
23/11-17	Georgios Papoutsakis	MSc student	*Georgios Papoutsakis*
23/11-17	Jesper Løve Hinrich	PhD student	*Jesper løve Hinrich*
23/11-17	Morten Mørup	Associate Professor	*[signature]*

Signature of the PhD student and the principal supervisor:	
Date: 24-11-17 PhD student:	Date: 24-11-17 Principal supervisor: